

STUDY OF THE DIPOLAR ISING SYSTEM  $\text{LiHo}_x\text{Y}_{1-x}\text{F}_4$  USING  $\mu\text{SR}$

STUDY OF THE DIPOLAR ISING SYSTEM  $\text{LiHo}_x\text{Y}_{1-x}\text{F}_4$  USING  
MUON SPIN RELAXATION/ROTATION

By

JOSE RODRIGUEZ, ENG. & MSc.

A Thesis

Submitted to the School of Graduate Studies

in Partial Fulfilment of the Requirements

for the Degree

Doctor in Philosophy of Science

McMaster University

©Copyright by Jose Rodriguez, August 2009

DOCTOR IN PHILOSOPHY OF SCIENCE (2009)  
(Department of Physics and Astronomy)

McMaster University  
Hamilton, Ontario

TITLE: Study of the dipolar Ising system  $\text{LiHo}_x\text{Y}_{1-x}\text{F}_4$  using muon spin relaxation/rotation

AUTHOR: Jose Rodriguez, Eng. & MSc.

SUPERVISOR: Graeme M. Luke

NUMBER OF PAGES: xiii, 175

# Abstract

$\text{LiHo}_x\text{Y}_{1-x}\text{F}_4$  is an insulating system where the Ho ions are magnetic. The crystal field gives an Ising character to the Ho ions, and the dominant interaction between them is through magnetic dipolar fields. For  $x=1$ , the system is a ferromagnet with a critical temperature of 1.54 K. The critical temperature decreases as  $x$  is decreased until  $x \approx 0.25$ . At that point the long range order is destroyed, giving rise to a state with some characteristics of spin glass behavior.

The study of this system is important because its Ising nature makes it a test ground for theoretical models. Interestingly, not only experiments and theory diverge in many points, but experimental data from different research groups are contradictory. In order to contribute to a clearer experimental picture, we performed  $\mu\text{SR}$  measurements in this system and we present our results in this thesis.

In the ferromagnetic samples ( $x=1$  and 0.45) we found that the internal field distribution at the muon site is quite broad, even in the  $x=1$  system. Then it is possible that the magnetic field distribution at the Ho ions is broad as well. We show qualitatively how this broadening could explain a feature of the field-temperature phase diagram which is still not understood.

For the more diluted samples ( $x=0.25, 0.12, 0.08, 0.045$  and 0.018), we found that they all have the same qualitative behavior as a function of temperature and magnetic field. Our analysis of the data did not show any feature of canonical spin glass behavior. Instead, an analysis using dynamical Kubo-

Toyabe functions show a temperature independent fluctuation rate of the Ho moments below  $\approx 0.5$  K for all these samples. This behavior is characteristic of cooperative paramagnetic systems. We also found that the low temperature fluctuation rate decreases as  $x$  is decreased.

To analyze the data from  $\text{LiHo}_x\text{Y}_{1-x}\text{F}_4$  we developed microscopic models of  $\mu\text{SR}$  signals. These models are presented in this thesis and they correspond to stochastic models of signals using stretched magnetic field distributions; and the modeling of signals from systems with F- $\mu$ -F bond formation where the set of bonds does not have cubic symmetry.

# Acknowledgements

I want to thank my supervisor Dr. Graeme Luke for his guidance and generosity during the last six years. In special, I have greatly appreciated his friendliness, understanding and true commitment to the professional development of all his students. I would like to extend my thanks to Dr. B. Gaulin and Dr. T. Imai for guiding my research, and for kindly helping me when ever I approached them with a question or a problem.

Even though this thesis carries my name as its author, many people have participated on its completion. I want to gratefully acknowledge the contribution of A. Aczel, J. Carlo, Dr. S. Dunsiger, Dr. G. MacDougall, Dr. P. Russo, Dr. A. Savici, Dr. Y. Uemura, Dr. C. Wiebe and T. Williams. They not only helped me collecting the data shown in this document, but they also participated actively in many discussions regarding the work presented in this thesis.

During the research work that led to this thesis I had the opportunity to discuss technical and theoretical aspects of it with several experts in the field. I want to thank Dr. J. Brewer, Dr. M. Gingras, Dr. K. Kallin, Dr. M Schechter and Dr. P. Stamp for kindly addressing my questions and contributing with ideas. I want to further thank Dr. M. Gingras for accepting to be a member of my examining committee, and for providing several comments and corrections for this document. The quality of the thesis certainly improved thanks to him.

The experimental data shown in this work was acquired thanks to the excellent work of the staff of the TRIUMF "Center for Molecular and Materials Science". I would like to thank in special R. Abasalti, D. Arseneau, B. Hitti and S. Kreitzman. These people have always been committed to the success of our measurements... even at 3AM and during a weekend.

The samples used in this study were prepared for measurements thanks to the collaboration of different people in McMaster University. I am indebted to Dr. A. Dabkowski, Dr. H. Dabkowska and Dr. D. Lozano who helped me and taught me how to perform sample preparation: from the synthesis of materials and crystal growth, to alignment and crystal cutting.

My work in McMaster University would not have been possible without the help of the technical staff from the “Brockhouse Institute for Materials Research”, in particular to C. Butcher, A. Duncan and Dr. P. Dube. I would like to extend my thank to the staff of the McMaster Physics department: M. Esposito, C. Johnston, R. McNeice, L. Penney, T. Stewart and D. Kilgour. These people have not participated in my research projects, but they have certainly made my life easier during the last six years, and they always did it with a smile in their face.

I want to take this opportunity to thank my family who has supported and encouraged my studies during my life; and, finally, I want to thank my wife Mariangela for always being a source of support, strength and joy.

# Table of Contents

<b>Abstract</b>	iii
<b>Acknowledgements</b>	v
<b>List of Figures</b>	x
<b>List of Tables</b>	xiv
<b>Chapter 1 Magnetism and Ising models</b>	<b>1</b>
1.1 Ferromagnetic TFIM . . . . .	3
1.2 The ferromagnetic random TFIM . . . . .	7
1.3 The Sherrington-Kirkpatrick model . . . . .	11
<b>Chapter 2 Introduction to <math>\text{LiHo}_x\text{Y}_{1-x}\text{F}_4</math></b>	<b>15</b>
2.1 The Hamiltonian . . . . .	16
2.2 Experimental studies of $\text{LiHo}_x\text{Y}_{1-x}\text{F}_4$ . . . . .	19
2.2.1 The ferromagnetic state . . . . .	19
2.2.2 The spin glass state . . . . .	25
2.2.3 The “antiglass” phase . . . . .	30
2.3 Theoretical studies of $\text{LiHo}_x\text{Y}_{1-x}\text{F}_4$ . . . . .	34
2.3.1 The ferromagnetic state . . . . .	34
2.3.2 The spin glass state . . . . .	42
2.4 Study of $\text{LiHo}_x\text{Y}_{1-x}\text{F}_4$ using $\mu\text{SR}$ . . . . .	45

<b>Chapter 3</b>	<b>Muon spin relaxation/rotation</b>	<b>47</b>
3.1	The basic concept . . . . .	47
3.2	Experimental setups . . . . .	52
3.3	Technical details of the $\mu$ SR experiment . . . . .	53
3.4	Modeling of muon spin relaxation data . . . . .	56
3.4.1	Probabilistic models . . . . .	58
3.4.2	Dynamic probabilistic models . . . . .	61
3.4.3	Stretched probability distributions . . . . .	66
3.4.4	The F- $\mu$ -F bond . . . . .	75
3.4.5	The $\mu$ SR signal from a ferromagnet . . . . .	80
<b>Chapter 4</b>	<b><math>\mu</math>SR studies of the x=1 and 0.45 systems</b>	<b>82</b>
4.1	Sample preparation . . . . .	82
4.2	F- $\mu$ -F in $\text{LiHo}_x\text{Y}_{1-x}\text{F}_4$ . . . . .	85
4.3	$\text{LiHoF}_4$ . . . . .	89
4.4	$\text{LiHo}_{0.45}\text{Y}_{0.55}\text{F}_4$ . . . . .	100
4.5	Comments on the ferromagnetic state . . . . .	106
4.6	Overview . . . . .	110
<b>Chapter 5</b>	<b><math>\mu</math>SR studies of systems with <math>x \leq 0.25</math></b>	<b>112</b>
5.1	$\text{LiHo}_{0.25}\text{Y}_{0.75}\text{F}_4$ . . . . .	115

5.1.1	Phenomenological analysis . . . . .	115
5.1.2	Microscopic analysis . . . . .	121
5.2	$\text{LiHo}_x\text{Y}_{1-x}\text{F}_4$ for $x \leq 0.12$ . . . . .	127
5.2.1	Phenomenological analysis . . . . .	128
5.2.2	Microscopic analysis . . . . .	133
5.3	Overview . . . . .	147
<b>Chapter 6 Discussion</b>		<b>149</b>
6.1	F- $\mu$ -F . . . . .	149
6.2	Ferromagnetism . . . . .	151
6.3	The disordered phase . . . . .	154
6.4	Conclusions . . . . .	157
6.5	Further work . . . . .	159
<b>Appendix A Field width vs. doping</b>		<b>163</b>
<b>Bibliography</b>		<b>166</b>

# List of Figures

1.1	$\langle S^z \rangle$ and $\langle S^x \rangle$ for the mean field ferromagnetic TFIM . . . . .	6
1.2	$H$ -T phase diagram for the TFIM . . . . .	7
1.3	$H$ - $z_0$ phase diagram of the ferromagnetic random TFIM . . . . .	9
1.4	$\langle S_z \rangle$ as a function of temperature for $H=0$ and three random fields	10
1.5	$J_0$ -T phase diagram from the SK model . . . . .	14
2.1	Unit cell for $\text{LiHoF}_4$ . . . . .	16
2.2	T-x phase diagram in $H = 0$ . . . . .	20
2.3	$H$ -T phase diagram for $x=1$ . . . . .	22
2.4	$H$ -T phase diagram for the $x=0.44$ system . . . . .	24
2.5	$H$ -T phase diagram for $x=0.198$ and $0.167$ . . . . .	27
2.6	$\chi_{AC}$ for $x=0.167$ as a function of transverse field . . . . .	28
2.7	$\chi_{AC}$ for $x=0.167$ as a function of frequency . . . . .	29
2.8	Scaled $\chi_{AC}''$ for $x=0.167, 0.045$ . . . . .	31
2.9	Effective transverse field in $\text{LiHo}_x\text{Y}_{1-x}\text{F}_4$ . . . . .	36
2.10	Theoretical T-x phase diagram . . . . .	40
3.1	Muon spin precession . . . . .	49
3.2	Experimental setup for TF . . . . .	53
3.3	Experimental setup for LF . . . . .	54

3.4	Gaussian Kubo-Toyabe in LF . . . . .	60
3.5	Lorentzian Kubo-Toyabe in LF . . . . .	61
3.6	Dynamic Gaussian Kubo-Toyabe in ZF . . . . .	63
3.7	Dynamic Gaussian Kubo-Toyabe in the narrowing limit. . . . .	64
3.8	Dynamic Lorentzian Kubo-Toyabe in ZF . . . . .	67
3.9	$G_z(t)$ from stretched probability distributions in ZF . . . . .	68
3.10	$G_z(t = \infty)$ as a function of $\Delta_x/\Delta_{yz}$ . . . . .	69
3.11	$G_z(t)$ for a one dimensional Lorentzian field distribution in LF . . . . .	70
3.12	$G_z(t)$ for a one dimensional Lorentzian field distribution for different $\nu$ in ZF . . . . .	72
3.13	$G_z(t)$ for a two dimensional Lorentzian field distribution for different $\nu$ in ZF . . . . .	73
3.14	Characteristic signal from an F- $\mu$ -F bond. . . . .	76
3.15	F- $\mu$ -F signal as a function of time and $\theta$ . . . . .	80
4.1	Crystal of $\text{LiHo}_x\text{Y}_{1-x}\text{F}_4$ . . . . .	83
4.2	Laue pattern from $\text{LiHo}_x\text{Y}_{1-x}\text{F}_4$ . . . . .	84
4.3	Experimental setup for $\text{LiHo}_x\text{Y}_{1-x}\text{F}_4$ . . . . .	85
4.4	F- $\mu$ -F signal in $\text{LiHoF}_4$ . . . . .	86
4.5	Relaxation rate of F- $\mu$ -F signal as a function of temperature . . . . .	87

4.6	Characteristic frequency of the F- $\mu$ -F signal as a function of temperature . . . . .	88
4.7	Corrected asymmetries for LiHoF <sub>4</sub> at 2T LF . . . . .	91
4.8	$\mu$ SR signal for LiHoF <sub>4</sub> at 50mK and LF=20G . . . . .	92
4.9	$f_{\text{ferro}}$ as a function of T in ZF for x=1 and x=0.45 . . . . .	93
4.10	$\lambda_1$ as a function of T in ZF for x=1 and x=0.45 . . . . .	95
4.11	$\mu$ SR signal for x=1 as a function of LF at T=50mK . . . . .	96
4.12	$\lambda_{\text{LF}}$ as a function of LF for x=1 and x=0.45 . . . . .	97
4.13	Relaxing asymmetry for x=1 at T=50mK as a function of LF . . . . .	98
4.14	$\mu$ SR signal for LiHo <sub>0.45</sub> Y <sub>0.55</sub> F <sub>4</sub> at 15mK and LF=20G . . . . .	101
4.15	Corrected asymmetry for X=0.45 in a TF of 1T . . . . .	103
4.16	$\lambda$ as a function of TF at 15mK in x=0.45 . . . . .	104
4.17	Frequency shift of the TF fast component for x=0.45 . . . . .	105
4.18	$f_{\text{ferro}}$ Vs. T with the mean field order parameter . . . . .	107
4.19	Mean field order parameter with and with out random fields. . . . .	108
5.1	Raw asymmetry of the x=0.08 sample at 15mK . . . . .	114
5.2	$\mu$ SR signals in ZF at T=0.025K and 3.5K for x=0.25 . . . . .	116
5.3	$\mu$ SR signals at T=0.025K as a function of LF for x=0.25 . . . . .	117
5.4	$\lambda$ as a function of temperature and LF for x=0.25 . . . . .	118
5.5	$\beta$ as a function of temperature and LF for x=0.25 . . . . .	120

5.6	Moment size of a single $\text{Ho}^{3+}$ ion as a function of temperature in ZF123	
5.7	$\nu$ for $T < 1\text{K}$ at different LF for $x=0.25$ . . . . .	125
5.8	$\mu\text{SR}$ relaxation functions of the $x=0.045$ system at 15mK, 1K and 10K in a LF of 20G . . . . .	128
5.9	Relaxation rate as a function of temperature for $x=0.12, 0.08$ and 0.045 in low LF . . . . .	131
5.10	Power of exponential as a function of temperature for $x=0.12, 0.08$ and 0.045 in low LF . . . . .	132
5.11	Corrected asymmetry of $x=0.045$ in a LF of 20G and at 20mK . . . . .	139
5.12	Parameter $a$ from the Kubo-Toyabe theory plotted as a function of $x$ , for $x \leq 0.12$ . . . . .	140
5.13	Fluctuation rate as a function of temperature for $x \leq 0.12$ . . . . .	141
5.14	Fluctuation rate as a function of $x$ at low temperature . . . . .	142
5.15	Corrected asymmetry for a LF scan at 12mK for $x=0.12$ . . . . .	143
5.16	$\nu$ Vs. LF at 12mK for $x=0.12$ . . . . .	144
5.17	Corrected asymmetry for a LF scan at 25mK for $x=0.018$ . . . . .	145
5.18	Corrected asymmetry for $x=0.018$ at 25mK and 2.5K in 10G LF . . . . .	147
6.1	$f_{\text{ferro}}/x$ as a function of $T/x$ in ZF for $x=1$ and $x=0.45$ . . . . .	153
6.2	$x$ - $T$ phase diagram from $\mu\text{SR}$ . . . . .	159

# List of Tables

4.1	Background in ZF or low LF. . . . .	90
4.2	Characteristic field strength for $x=1$ (@50mK) and 0.45 (@15mK)	109
5.1	Relaxation parallel and perpendicular to the Ising axis for $x=0.08$	136
5.2	Reduced $\chi^2$ values for fit of the low LF data for $x \leq 0.12$ . . . . .	139
6.1	$\chi^2$ values for fits of the F- $\mu$ -F signal with the corrected and cubic fitting functions. . . . .	150

# Chapter 1

## Magnetism and Ising models

Understanding the magnetic properties of materials has captured the attention of many researchers for more than 2000 years [1]. However, it was not until the 20th century, when the theoretical framework of quantum mechanics was developed, that this property of matter could be linked to its atomic origin; magnetism is a cooperative quantum mechanical phenomena.

We understand the magnetic properties of a system when we can explain its behavior from basic principles. Ideally, this would imply solving the quantum mechanical many body Hamiltonian for a macroscopic collection of periodically-placed atomic nuclei plus electrons. Finding a general solution for this kind of problem is an impossible job. Also, even if such a task could be performed, it would turn out to be a formidable display of mathematical skills but probably unable to provide us with physical insight about the behavior of a system. With this in mind, scientists have abstracted simpler mathematical models which can reproduce observed physical phenomena. The advantage of the model is not just to simplify the analysis, but also to provide us with a clear picture of the physical processes which are involved.

One of the most common models used to study magnetic phenomena is the Transverse Field Ising Model (TFIM). This model, which will be explained in the following section, is able to reproduce many observed magnetic phenomena (e.g. ferromagnetism and spin glass order), and it is simpler to use than other models (e.g. Heisenberg model\*). Moreover, this model has been extensively used theoretically due to its suitability to study field induced quantum fluctuations [2].

In many cases the TFIM model describes only qualitatively the physical behavior of real magnetic systems, but sometimes systems can be found with physical characteristics which make them suitable for a TFIM description (e.g. the ferromagnets  $\text{FeCl}_2$  [3] and  $\text{CoCl}_2$  [4]). The study of these systems is very important since they are quantitative test grounds for our understanding of the TFIM.  $\text{LiHo}_x\text{Y}_{1-x}\text{F}_4$  is a system with many of the characteristics of a TFIM, but its magnetic behavior has turned out to be richer than expected. Understanding these new features through the TFIM has been an experimental and theoretical challenge. This effort has produced many results, but big questions remain unsolved. This state of affairs make this system a very interesting scientific object and a potential source of new physical phenomena. In this work we compile the experimental research that we have performed in this system during the last four years.

In the remainder of this chapter we will present an introduction to different transverse field Ising models which are relevant to  $\text{LiHo}_x\text{Y}_{1-x}\text{F}_4$ . These text-

---

\* In contraposition to the TFIM, in the Heisenberg model, all the three components of the magnetic moment enter in the magnetic moments interactions.

book examples aim to illustrate qualitatively some of the physical properties of the different phases that  $\text{LiHo}_x\text{Y}_{1-x}\text{F}_4$  is believed to have. After this, Chapter 2, presents an introduction to  $\text{LiHo}_x\text{Y}_{1-x}\text{F}_4$  together with a brief review of experimental and theoretical work. Also in Chapter 2, we point out some of the most intriguing questions about  $\text{LiHo}_x\text{Y}_{1-x}\text{F}_4$  and how our research can address them. Since the experimental tool we used to investigate  $\text{LiHo}_x\text{Y}_{1-x}\text{F}_4$  is the muon Spin Relaxation/Rotation ( $\mu\text{SR}$ ) technique, we present an introduction to it in Chapter 3. In this chapter we also show an overview of standard functions used to analyze  $\mu\text{SR}$  data as well as our own contributions to the topic. In Chapters 4 and 5 we present our  $\mu\text{SR}$  measurements and data analysis for the dense ( $x \geq 0.45$ ) and diluted ( $x \leq 0.25$ ) samples respectively. Finally, in Chapter 6 we present further discussion on our findings, an overview of our main results, and proposes some calculations and measurements to perform.

## 1.1 Ferromagnetic TFIM

The transverse field Ising Hamiltonian for a collection of interacting magnetic moments can be expressed as:

$$H = \sum_i \left[ \sum_{j \neq i} \frac{-J_{i,j}}{2} S_i^z S_j^z - H S_i^x \right] \quad (1.1)$$

Here  $S_i^z$  is the Pauli spin operator along  $z$  for the  $i$  spin,  $J_{i,j}$  is the interaction term between spin  $i$  and  $j$ , and  $H$  is an external magnetic field transverse to the Ising ( $\hat{z}$ ) axis. We will assume that these moments occupy the sites of magnetic ions in a lattice and that, for the moment,  $H = 0$ . Then, if

$J_{i,j} \geq 0$  for every  $(i, j)$  pair, it is expected that the Hamiltonian will have a doubly degenerate ground state where all the spins point either up or down. This is the ferromagnetic ground state, where the macroscopic alignment of magnetic moments produce a macroscopically observable magnetic field. This  $H = 0$  problem is equivalent to its classical analogue (with classical magnetic moments restricted to point up or down) since the eigenvectors of the Hamiltonian are given in the spin up/down basis (*ie.*  $|\pm, \pm, \pm, \dots\rangle$ ). When  $H > 0$ , the second term in Equation 1.1 (which is proportional to  $S_i^x = S_i^+ + S_i^-$ ) can couple the  $|+\rangle$  and  $|-\rangle$  Ising states and induce a quantum superposition of states. In this case the system can no longer be described classically and, furthermore, if  $H$  is increased enough, a quantum phase transition (at  $T=0$ ) from the ferromagnetic state into a paramagnetic state can occur.

To illustrate how ferromagnetism arises we will consider the simplest ferromagnetic interaction:  $J$  is constant between nearest neighbor spins and zero otherwise. The physical behavior of this problem depends on the dimensionality of the lattice. It can be shown that if the array of spins is a one dimensional chain, the critical temperature at which ferromagnetism sets in (called  $T_c$ ) is zero [5]; but in two and three dimensions  $T_c$  is finite. For the rest of this work we will always assume that the lattices are three dimensional since that is the case relevant for  $\text{LiHo}_x\text{Y}_{1-x}\text{F}_4$ . Then, with the previous assumptions we can write the mean field version of the Hamiltonian in Equation 1.1 by substituting  $S_j^z$  by its thermal average  $\langle S^z \rangle$ :

$$H_{MF} = \sum_i [-Jn\langle S^z \rangle S_i^z - H S_i^x] \quad (1.2)$$

where  $n$  is the number of nearest neighbors. This Hamiltonian is easy to diagonalize and we can get the following expressions for the thermal averages of  $S^z$  and  $S^x$  [2]:

$$\langle S^z \rangle = \frac{Jn\langle S^z \rangle}{\sqrt{H^2 + (Jn\langle S^z \rangle)^2}} \tanh \left( \frac{\sqrt{H^2 + (Jn\langle S^z \rangle)^2}}{k_B T} \right) \quad (1.3)$$

$$\langle S^x \rangle = \frac{H}{\sqrt{H^2 + (Jn\langle S^z \rangle)^2}} \tanh \left( \frac{\sqrt{H^2 + (Jn\langle S^z \rangle)^2}}{k_B T} \right) \quad (1.4)$$

The solution for Equations 1.3 and 1.4 is shown in Figure 1.1 for  $H=0$  and  $H/nJ=0.5$ . It can be seen that the order parameter of the problem is  $\langle S^z \rangle$ , which is proportional to the magnetization along the Ising axis. For  $H=0$  the critical temperature ( $T_c$ ) is  $nJ/k_B$ , and  $\langle S^x \rangle$  is zero as expected. Above this critical temperature the magnetic moments are not correlated and fluctuate rapidly (this is the paramagnetic state). Upon the application of a transverse field  $T_c$  is reduced,  $\langle S^x \rangle$  acquires a nonzero value, and the low temperature value of  $\langle S^z \rangle$  is reduced by the fluctuations of the moments.  $H$  can be increased until the transverse field term (Zeeman splitting) wins over the ordering term and ferromagnetism is completely destroyed. At this point  $\langle S^z \rangle$  is zero at every temperature and  $\langle S^x \rangle$  has a value equal to 1 at  $T=0$ . The  $H$ - $T$  phase diagram for this problem is shown in figure 1.2 and, as expected from Equation 1.3, its shape is exactly the same as that of the  $H/nJ=0$  order parameter in Figure 1.1 with  $\langle S^z \rangle$  in the  $y$  axis substituted by  $H/nJ$ .

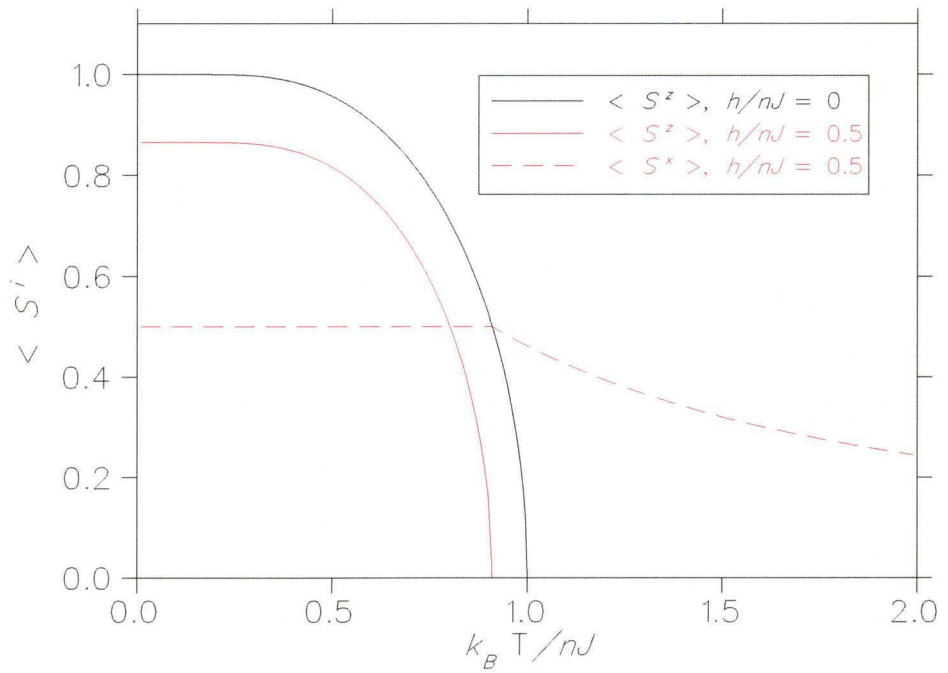
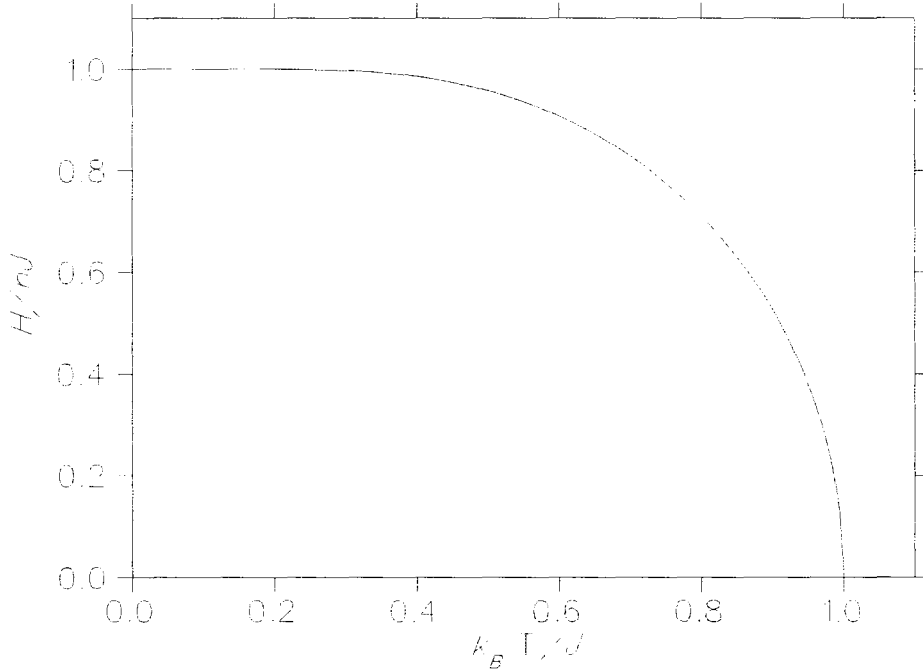


Figure 1.1: Mean field values for  $\langle S^z \rangle$  and  $\langle S^x \rangle$  for the nearest neighbor ferromagnetic TFIM in zero field (black line) and  $H/nJ$  equal to 0.5 .


 Figure 1.2: Mean field  $H$ - $T$  phase diagram for the TFIM.

## 1.2 The ferromagnetic random TFIM

The random TFIM Hamiltonian is given by:

$$H = \sum_i \left[ \sum_{j \neq i} -J_{i,j} S_i^z S_j^z - H S_i^x - z_i S_i^z \right] \quad (1.5)$$

This equation is the same as 1.1 but with the extra term  $z_i S_i^z$ . This term represents a local field of magnitude  $z_i$  along the Ising direction, and which magnitude and direction changes randomly from one site to the next. This random field is quenched (fixed for a given Hamiltonian) and it follows a given probability distribution  $P(z)$ . To exemplify how the random field affects a ferromagnetic system we assume that  $J_{i,j}$  is constant and equal to  $J/N$  ( $N$  being the number of magnetic moments in the lattice). This interaction couples

a given moment with every other, so the interaction is long-ranged. With these assumptions it can be shown that the mean field order parameter of the problem is given by [6]:

$$\langle S^z \rangle = \overline{\frac{2J\langle S^z \rangle + z}{\sqrt{H^2 + (2J\langle S^z \rangle + z)^2}} \tanh \left( \frac{\sqrt{H^2 + (2J\langle S^z \rangle + z)^2}}{k_B T} \right)} \quad (1.6)$$

The bar in this equation, which is very similar to Equation 1.3, represents the configuration average over the probability distribution  $P(z)$ . To make further progress we assume that the local random field has a constant magnitude equal  $z_0$ , but it can point up or down with equal probability. Then, the probability distribution for the random field is given by the following binary distribution:

$$P(z) = \frac{1}{2}\delta(z - z_0) + \frac{1}{2}\delta(z + z_0) \quad (1.7)$$

Using this random field distribution one gets the following expression for the order parameter [6]:

$$\begin{aligned} \langle S^z \rangle &= \frac{1}{2} \frac{\Sigma_+}{\sqrt{H^2 + \Sigma_+^2}} \tanh \left( \frac{\sqrt{H^2 + \Sigma_+^2}}{k_B T} \right) \\ &+ \frac{1}{2} \frac{\Sigma_-}{\sqrt{H^2 + \Sigma_-^2}} \tanh \left( \frac{\sqrt{H^2 + \Sigma_-^2}}{k_B T} \right) \end{aligned} \quad (1.8)$$

$$\Sigma_{\pm} = 2J\langle S_z \rangle \pm z_0 \quad (1.9)$$

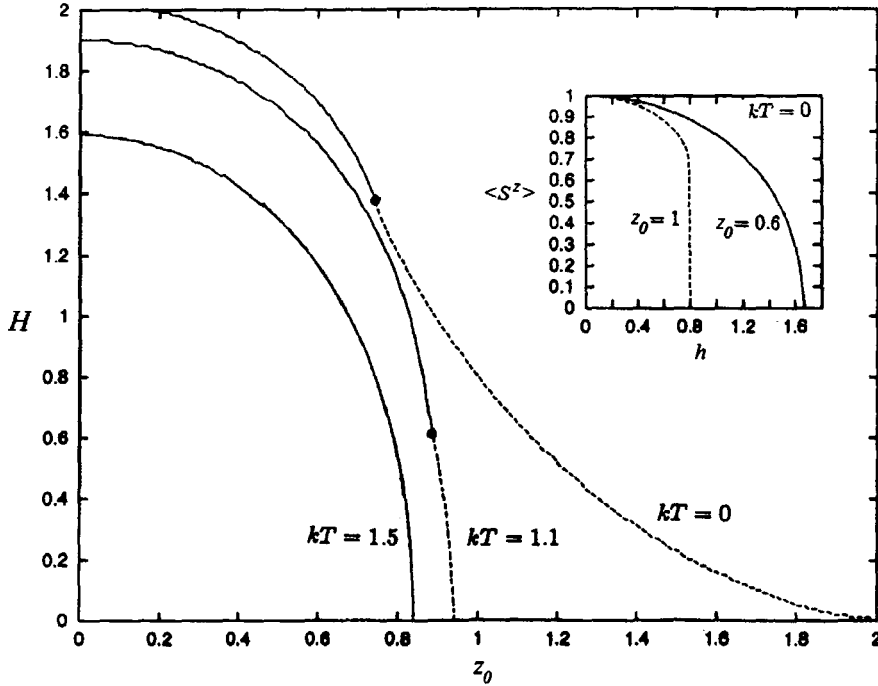


Figure 1.3: Mean field  $H$ - $z_0$  phase diagram for the ferromagnetic random TFIM (the regions below the curves correspond to the ferromagnetic regime). Dotted lines mark first order phase transitions while the continuous mark second order ones. The inset shows the effect of the random field on the order parameter. Taken from A. Dutta *et al.* (1996) [6].

Figure 1.3 shows the  $H$ - $z_0$  phase diagram calculated using Equation 1.8 at different temperatures. This diagram shows that random and transverse fields compete against the ferromagnetic ordering. This competition can also be seen in the inset of Figure 1.3 which shows the  $T=0$  order parameter at two different values of  $z_0$ . One can see that the critical field is reduced by an increment of the strength of the random field. Figure 1.4 shows this same effect but in  $H = 0$ ,  $T_c$  is reduced by an increment in  $z_0$ .

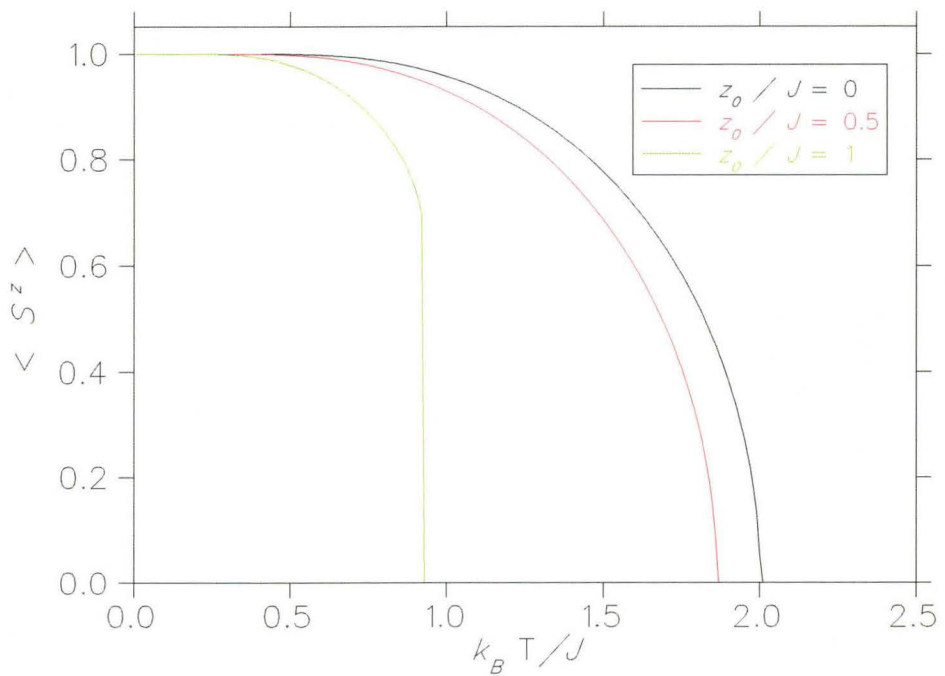


Figure 1.4: Ferromagnetic order parameter as a function of temperature and magnitude of the random field for  $H=0$ . Notice the change from second order phase transition at low values of  $z_0$ , to first order at higher ones.

Figures 1.3 and 1.4 show that the increase of  $z_0$  can change the phase transition from second order to first order. This is an effect from the binary distribution of the random field. If  $P(z)$  would have been chosen to be a smooth Gaussian distribution the ferromagnetic transition would have been continuous regardless of the width of the distribution [6].

### 1.3 The Sherrington-Kirkpatrick model

The Sherrington-Kirkpatrick (SK) Hamiltonian is given again by Equation 1.1, but what characterizes the model are the random interactions which are chosen such that every spin in the lattice interacts with every other one regardless of the distance between them (infinite ranged interactions). Furthermore, the values of  $J_{ij}$  are chosen randomly from the following Gaussian distribution:

$$P(J_{ij}) = \frac{N}{\sqrt{2\pi\Delta^2}} e^{-N(J_{ij}-J_0/N)^2/2\Delta^2} \quad (1.10)$$

where  $J_0$  is a positive parameter which can induce ferromagnetism and which for the moment will be assumed to be equal to zero; and  $N$  is the number of magnetic moments in our system. It is expected that the random couplings in this model generate frustrated interactions<sup>†</sup> which, together with the randomness itself, produce a spin glass ground state [8].

---

<sup>†</sup> One example of a frustrated interaction has two antiferromagnetically coupled spins which are each also antiferromagnetically coupled to a third one. The three bonds cannot be simultaneously satisfied and this makes frustrated systems display non trivial magnetic configurations [7]

In a spin glass the ground state does not have long range order <sup>†</sup> and is thought to be highly degenerate. Each degenerate state corresponds to a random spin configuration which is separated by very large free energy barriers from other configurations. This makes the jumping between free energy minima a rare event (the system is non-ergodic); and it is because of this that spin relaxation processes have very long time scales. It is actually this dynamic behavior that characterizes the spin glass state, and which is reflected in the spin glass order parameter (the Edwards-Anderson order parameter) [8]:

$$q = \lim_{t \rightarrow \infty} \langle \langle S_i(0) \cdot S_i(t) \rangle_T \rangle_C \quad (1.11)$$

where the inner brace represent a thermal average, while the outer one a configurational average over the random bonds. This order parameter acquires a nonzero value below  $T_g$ , the freezing temperature.

The SK model, with its infinite ranged interactions, seems to be unphysical; but its exact solution is believed to produce the right mean field behavior for the Edwards-Anderson model where interactions are short ranged. In the next chapter it will be shown that the long range interaction scenario (though not infinite) is relevant for  $\text{LiHo}_x\text{Y}_{1-x}\text{F}_4$ .

There has been considerable theoretical work in the SK model and most of it is mathematically complex (see [2] [8] and references therein). For the sake of illustrating the effect of the transverse field over the spin glass order

---

<sup>†</sup> By long range order we mean that at the spin glass phase transition the spatial correlation length does not diverge. This is in contrast to ferromagnetic systems for example.

we will just state a mean field like solution of the SK model for the  $H$ - $T$  phase diagram [2]:

$$\frac{H}{\Delta} = \tanh\left(\frac{H}{k_B T}\right) \quad (1.12)$$

This phase boundary, which has been calculated with the replica symmetric assumption<sup>§</sup>, illustrates that a transverse field destroys the spin glass state in a way which evokes that of the ferromagnetic model. More accurate calculations using this model place the zero temperature critical field at around  $1.51\Delta$  instead of  $H_c = \Delta$  which Equation 1.12 predicts [2].

Before we end this chapter, we would like to show what happens when  $J_0 \neq 0$  and  $H = 0$ . Assuming replica symmetry, it can be shown that this case would give rise to the phase diagram shown in Figure 1.5 [8]. This figure shows that for high values of  $J_0$  almost every bond in the system is ferromagnetic and, therefore, ferromagnetism prevails. As  $J_0$  decreases, strong frustrated bonds proliferate until the ground state is that of a spin glass. In the following chapter we will point out similarities between this phase diagram and that of  $\text{LiHo}_x\text{Y}_{1-x}\text{F}_4$ .

---

<sup>§</sup> A mathematical trick to calculate  $q$  in Equation 1.11 consist in introducing many replicas of the system which have the same quenched randomness but can have different initial conditions. Then, one can attempt to solve the problem assuming that the replicas are indistinguishable. This is unphysical, at least at low values of  $H$ , but captures many of the features of the spin glass qualitatively.

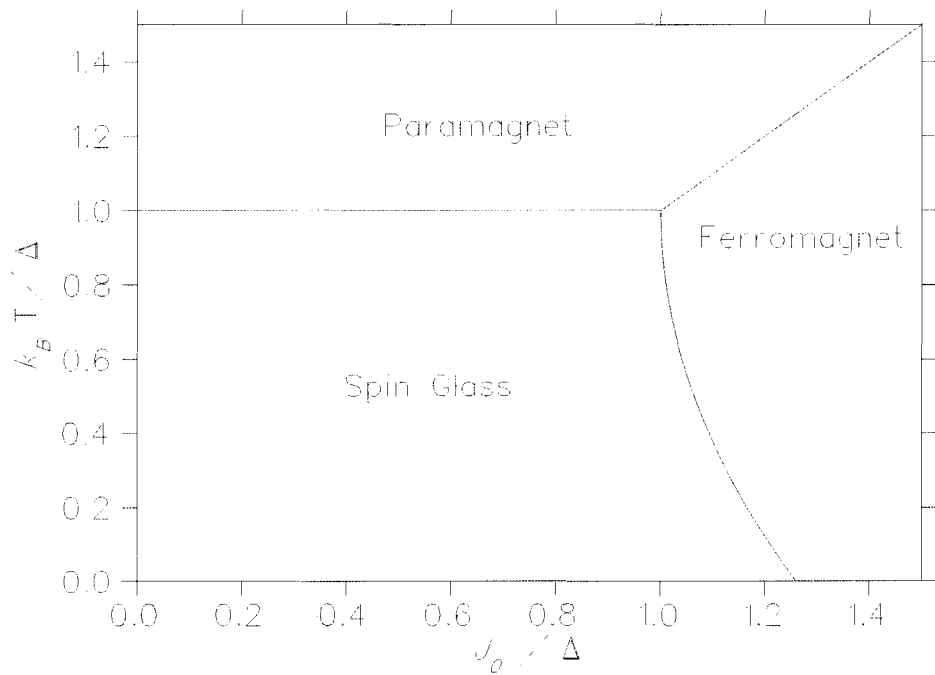


Figure 1.5: Approximate phase diagram for the replica symmetric solution of the SK model at  $H = 0$  [8].

## Chapter 2

### Introduction to $\text{LiHo}_x\text{Y}_{1-x}\text{F}_4$

The optical properties of  $\text{LiHo}_x\text{Y}_{1-x}\text{F}_4$  make it suitable to be used as lasing material [9] [10]. As a matter of fact, most of the early research on this system corresponds to the characterization of its optical properties through absorption, fluorescence and electron-paramagnetic-resonance measurements (see References 8 through 19 in [11]).

The interest in the magnetic properties of  $\text{LiHo}_x\text{Y}_{1-x}\text{F}_4$  began with the discovery of a the ferromagnetic phase transition in  $\text{LiTbF}_4$  which is driven by dipolar interactions [12]. This made the  $\text{LiReF}_4$  ( $\text{Re} = \text{Er}, \text{Dy}, \text{Ho}, \text{Tb}$ ) compounds very attractive to physicists who used them as tests for theoretical models.

We devote this chapter to introduce the reader to the magnetic behavior of  $\text{LiHo}_x\text{Y}_{1-x}\text{F}_4$ . First, we introduce the energy contributions to the Hamiltonian that have been shown to be essential to understand the physical behavior of  $\text{LiHo}_x\text{Y}_{1-x}\text{F}_4$ . After that, we present an overview of the most relevant experimental studies aimed to shine light on the low temperature state of this system. Then, we make a review of the theoretical research performed in this

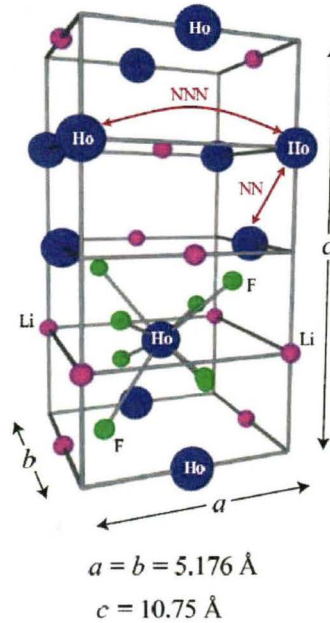


Figure 2.1: Unit cell for  $\text{LiHoF}_4$ . Taken from S. M. A. Tabei *et al.* (2008) [13].

system, and we conclude with a description of how  $\mu\text{SR}$  can contribute to its understanding.

## 2.1 The Hamiltonian

$\text{LiHo}_x\text{Y}_{1-x}\text{F}_4$  is an insulating ionic crystal which has a tetragonal (Scheelite) structure with a  $C_{4h}^6$  ( $I4_1/a$ ) symmetry (see Figure 2.1). The lattice constants are  $a = b = 5.146(1)\text{\AA}$  and  $c = 10.758(1)\text{\AA}$  (see [14] and references there). The  $\text{Ho}^{3+}$  ions are the strongest magnetic entities in the system, with Hund's rules giving  $^5I_8$  as the ground state of the isolated single ion. The Hamiltonian that is believed to describe the magnetic behavior of  $\text{LiHo}_x\text{Y}_{1-x}\text{F}_4$  in a transverse magnetic field (perpendicular to the crystallographic  $\hat{c}$  axis) is [15]:

$$\begin{aligned}
 H = & \sum_i V_{\text{cf}}(\vec{J}_i) - g_L \mu_B H \sum_i J_i^x + A_{\text{hf}} \sum_i \vec{J}_i \cdot \vec{I}_i \\
 & + \frac{1}{2} \frac{\mu_0}{4\pi} (g_L \mu_B)^2 \sum_{i \neq j} D_{ij}^{\nu\gamma} J_i^\nu J_j^\gamma + \frac{1}{2} J_{\text{ex}} \sum_{i,d} \vec{J}_i \cdot \vec{J}_{i+d}
 \end{aligned} \tag{2.1}$$

The first term in this expression corresponds to the effect of the crystal field on the  $\text{Ho}^{3+}$  atomic level structure. The point symmetry of the system is  $S_4$  and the single ion ground state of the  $\text{Ho}^{3+}$  ion in the presence of the crystal field is a  $\Gamma_{3,4}$  doublet [16]. This ground state doublet has  $\langle J^z \rangle \approx \pm 5.8$  and  $\langle J^x \rangle = \langle J^y \rangle = 0$ . This, together with the fact that the first excited crystal field level (a  $\Gamma_2$  singlet with  $\langle J^z \rangle = 0$ ) is  $\approx 11\text{K}$  above the ground state, gives an Ising character to the system for  $T \ll 11\text{K}$  [17].

The second term in the Hamiltonian is the Zeeman energy. Here  $H$  is an external magnetic field which points along  $\hat{x}$  and is therefore transverse to  $\hat{z}$ , the Ising axis. In Section 2.3, it will be shown that this transverse field is renormalized in the effective TFIM description of the system.

The third term corresponds to the nuclear hyperfine interaction. The stable isotope  $^{165}_{87}\text{Ho}$  possesses a nuclear angular momentum of  $7/2$  and the coupling to the electronic moment ( $A_{\text{hf}} \approx 38.6\text{mK}$ ) splits the Ising doublet into 8 doubly degenerate electro-nuclear levels separated by  $\approx 200\text{mK}$  from each other [16].

The first three terms of the Hamiltonian operate on a single Ho ion but it is the following two terms, the interaction terms, which are responsible for the interesting cooperative behavior. The fourth term is the dipolar magnetic interaction between different  $\text{Ho}^{3+}$  ions. Here  $g_L$  is the Landé factor, the value

of which is given by the Wigner-Eckart theorem to be  $5/4$ .  $D_{ij}^{\nu\gamma}$  is the dipolar tensor and is given by:

$$D_{ij}^{\nu\gamma} = \frac{\delta^{\nu\gamma} |\vec{r}_{ij}|^2 - 3(\vec{r}_{ij})^\nu (\vec{r}_{ij})^\gamma}{|\vec{r}_{ij}|^5} \quad (2.2)$$

where  $\vec{r}_{ij}$  is a vector from the  $i^{\text{th}}$  to the  $j^{\text{th}}$  ion.

The fifth and last term in Equation 2.1 is an indirect exchange interaction mediated by the fluorine ions. In this sum  $d$  runs over the nearest neighbor sites of a Ho ion at the  $i^{\text{th}}$  position. This exchange interaction is antiferromagnetic and its value, which has not been measured directly, is still a matter of debate. Reported strengths for this interaction range from -1mK (from fitting the  $H$ - $T$  phase diagram with a mean field model [18]) to -11mK (from fitting of specific heat data [11]). The latest and most reliable calculations, based on quantum Monte Carlo simulations and which use  $J_{\text{ex}}$  as a fit parameter to get the observed  $T_c$  in zero external field, estimate a value of 3.91mK [13] [17].

The second nearest neighbor exchange interaction is believed to be an order of magnitude smaller than the nearest neighbor one [11] and is generally ignored. Furthermore, in some calculations, even the nearest neighbor exchange interaction is neglected and only the dipolar one is considered (the dipolar interaction at the nearest neighbor sites is ferromagnetic and its strength is approximately double the exchange one). The dipolar interaction is dominant in  $\text{LiHo}_x\text{Y}_{1-x}\text{F}_4$  due to its strength and its long range. This has been confirmed experimentally by magnetic susceptibility [19], specific heat [11], neutron scattering [14] [20] and high resolution optical spectroscopy [21].

## 2.2 Experimental studies of $\text{LiHo}_x\text{Y}_{1-x}\text{F}_4$

The temperature-doping phase diagram of  $\text{LiHo}_x\text{Y}_{1-x}\text{F}_4$  is interesting and rich in physics (see Figure 2.2). It is interesting to compare this phase diagram with the  $T$ - $J_0$  one from the Sherrington-Kirkpatrick (SK) model in Figure 1.5. If a rough continuous approximation is done, one would expect that  $J_0$  in the SK model would scale with the typical interaction strength which is proportional to  $x$  in a dipolar system\*. Also, the width of the field distribution in the spin glass part of the phase diagram should scale with  $\sqrt{x}$  (see appendix A). Then, the SK phase diagram in Figure 1.5 could be interpreted as a phase diagram where  $T/\sqrt{x}$  is plotted in the  $y$  axis, while the  $x$  axis shows the value of  $\sqrt{x}$ . If this mapping is done then both phase diagrams show strong similarities. Nevertheless  $\text{LiHo}_x\text{Y}_{1-x}\text{F}_4$  has a richer physical behavior than what the SK model can describe. In this section we review the most relevant experimental results on the system as we move in the phase diagram from  $x=1$  to  $x=0$ .

### 2.2.1 The ferromagnetic state

$\text{LiHoF}_4$  has a ferromagnetic ground state with  $T_c = 1.5384\text{K}$  [23]. This low  $T_c$  is a consequence of the phase transition being driven by weak dipolar interactions [11] [21]. The uniaxial (Ising) nature of this system is observed in

---

\* The average distance between magnetic moments in a diluted system scales with dilution as  $x^{1/3}$ , since the the dipolar interaction between two magnetic moments goes as  $r^{-3}$  ( $r$  is the distance between the moments), then the characteristic dipolar interaction strength scales as  $x$ .

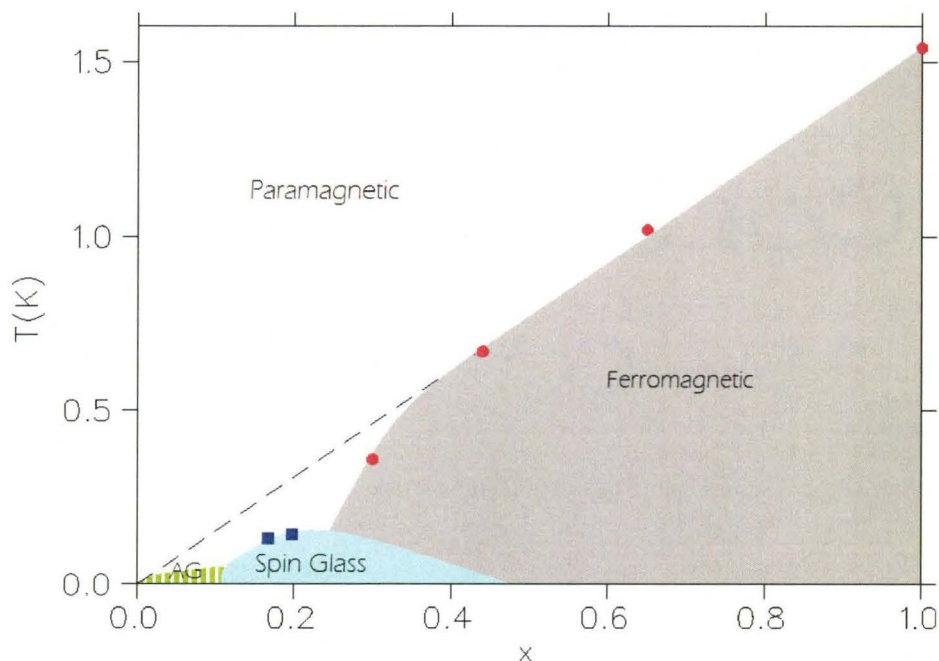


Figure 2.2: Approximate temperature-doping phase diagram of  $\text{LiHo}_x\text{Y}_{1-x}\text{F}_4$  in zero external field. The red circles have been determined by magnetization and neutron scattering measurements [20]. The blue squares have been determined by AC magnetic susceptibility measurements [22]. The green shaded area on the left corresponds to the crossover region to the “Anti-Glass” behavior (observed at  $x=0.045$ ) [20].

the fact that the magnetization along the  $\hat{c}$  direction is much bigger than that perpendicular to it ( $g_{\parallel} \approx 13.7$  and  $g_{\perp} = 0$ ) [19].

If a large enough external magnetic field is applied perpendicular to the Ising axis, the ferromagnetic state can be destroyed by magnetic moment fluctuations (as we saw is the case for the nearest neighbor ferromagnetic Transverse Field Ising Model (TFIM) in Chapter 1). This gives rise to the  $H$ - $T$  phase diagram shown in Figure 2.3. It has been observed that the effect of the external field is to reduce  $T_c$  to zero, making the phase diagram end at a quantum critical point ( $H_c \approx 4.95\text{T}$  [24]). An interesting feature of this phase diagram is the upturn of  $T_c$  below 0.4K (compare Figures 1.1 and 2.3). As will be mentioned in Section 2.3, this upturn is a consequence of the hyperfine electro-nuclear coupling [24]. It has been also demonstrated that the predictions from “Renormalization Group Theory” for a dipolar Ising ferromagnet are followed at the zero field critical point [23].

Another consequence of the hyperfine interaction on the  $H$ - $T$  phase diagram on Figure 2.3, is that it might prevent us from observing quantum criticality in this system. This was noticed from inelastic neutron scattering data as an incomplete mode softening of the lowest excitation energy as the phase transition is crossed at 0.31K [18]. In this study as well, the finite width of the (2,0,0) magnetic Bragg peak at the critical field, suggested that the hyperfine coupling could be limiting the divergence of the coherence length at the phase transition.

If the system is diluted by randomly introducing non-magnetic  $Y^{3+}$  at sites previously occupied by magnetic Ho ions, then the ferromagnetic  $T_c$  is initially

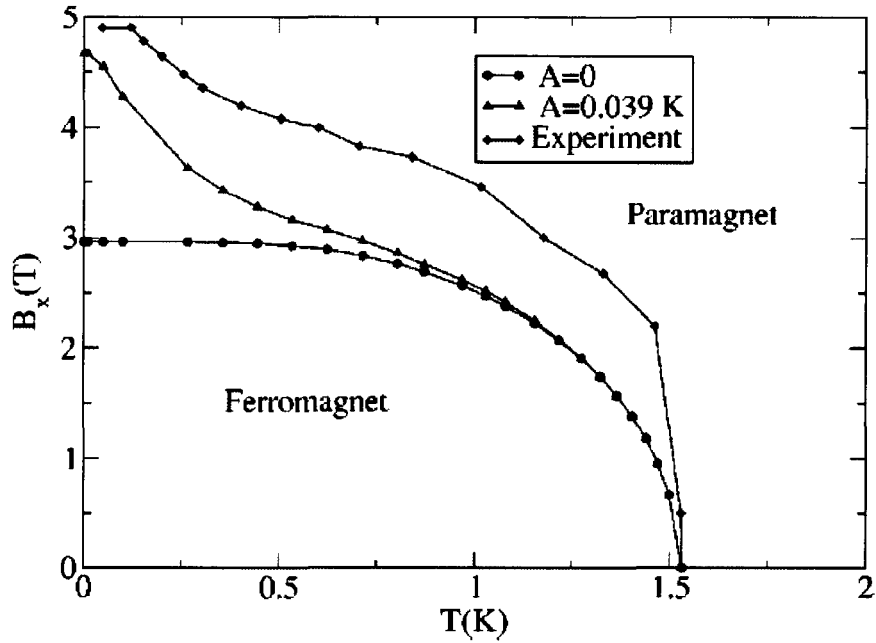


Figure 2.3: Field vs Temperature phase diagram for  $\text{LiHoF}_4$ . The “Experiment” points are  $\chi_{AC}$  data from from Bitko *et al.* (1996) [24] (the shape of this phase diagram has been confirmed by neutron scattering [18]). The “A=0” points were obtained from a quantum Monte Carlo simulation with no hyperfine coupling. The “A=0.039K” points were originated by performing a simulation which included the hyperfine coupling term. Taken from P. B. Chakraborty *et al.* (2004) [15]. Notice that this work uses the symbol  $B_x$  to refer to  $H$ .

decreased in a mean field (linear) way giving rise to an  $x$ - $T$  phase diagram that has a ferromagnetic ground state for  $0.3 \lesssim x \leq 1$ . Most of the work on the diluted ferromagnet has been performed for  $x=0.44$  ( $T_c=0.669\text{K}$  [25] in zero field). In this system,  $\chi_{AC}$  measurements show evidence of quantum tunneling of magnetic domain walls (in opposition to the thermally activated motion of the wall, an effect that is also observed). The energy barrier necessary for quantum tunneling is made available through the pinning of domain walls by magnetic vacancies [26]. In this system an anomalous critical exponent has been observed for the real part of  $\chi_{AC}(T, H)$  (where  $H$  is the externally applied field transverse to the Ising axis). For  $x=1$ ,  $\chi' \propto 1/H^2$  but at  $x=0.44$  it was found  $\chi' \propto 1/H$ . The difference was proposed to be due to the presence of a Griffiths singularity [25] but the exact nature of this effect is still not clear.

The  $x=0.44$  system has shown evidence for having a reentrant transition from the ferromagnetic state into a ferroglass state with decreasing temperature and in a nonzero transverse field [27]. The ferroglass state is characterized by a nonzero magnetization, like the ferromagnetic state, and by a different value of  $\chi_{AC}$  depending if the point in the phase diagram was achieved by a zero field cooled or field cooled protocol [28] (behavior characteristic of a spin glass). Also, this ferroglass state has shown evidence of achieving a state with a faster dynamical response depending if the point in the ferroglass phase is reached by entering the dome from the top (path ABC in Figure 2.4) or from the bottom (path DEC in Figure 2.4) [27]. The state with a faster dynamical response was considered by the authors of Reference [27] to be closer to a global minimum of the free energy and, therefore, closer to a real ground state. Then,

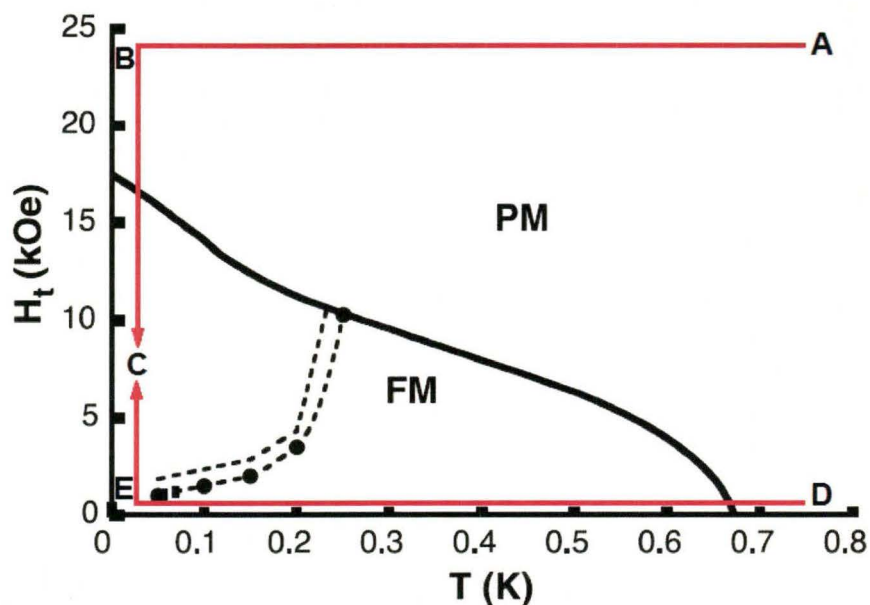


Figure 2.4:  $H$ - $T$  phase diagram for the  $x=0.44$  system. PM stands for paramagnetism, FM for ferromagnetism and FG for ferroglass. The difference in  $\chi_{AC}$  between paths ABC and DEC was interpreted as evidence for quantum annealing. Adapted from J. Brooke *et al.* [27]. Notice that this work uses the symbol  $H_t$  to refer to  $H$ . The physical meaning of the double dashed line is not explained in the reference, but most probable indicates the set of points which delimit the low temperature region where field-cool and zero-field-cool protocols give different values for  $\chi$ .

this measurements were considered as an observation of a quantum annealing process.

Before finishing this section we want to point out that there is not much experimental data available in the diluted ferromagnetic state and that all the measurements performed so far may have been done with the same set of samples since they are reported mostly by the same research group. Also, only  $\chi_{AC}$  is the only technique that has been used to probe the diluted ferromagnetic

part of the phase diagram. The exact nature and existence of the transition to a ferroglass state needs to be further studied by experiments.

### 2.2.2 The spin glass state

A further increase of the magnetic dilution produces a spin glass ground state in  $\text{LiHo}_x\text{Y}_{1-x}\text{F}_4$ . This low temperature state has been inferred from  $\chi_{AC}$  measurements in a sample with  $x=0.167$ . These measurements give a  $T_g \approx 0.133\text{K}$  [29] [30]. It is interesting to note that, even though the low temperature behavior is glassy, neutron scattering studies in this system have observed an onset of ferromagnetic correlations at  $T^* \approx xT_{c,x=1} = 0.257\text{K}$  [20]. This fact suggests the possibility that the ground state of the  $x=0.167$  is not a spin glass but a cluster glass (a glassy array of clusters of spins which have an internal ferromagnetic structure).

If an external magnetic field is applied transverse to the Ising axis of the  $x=0.167$  sample,  $T_g$  is reduced (in analogy to what was found in the SK model, see Equation 1.12). This gives rise to the  $H$ - $T$  phase diagram shown in Figure 2.5. It is interesting to note that in this phase diagram the  $T=0$  critical field is almost an order of magnitude bigger than the zero field  $T_g^\dagger$ . One would expect the  $T=0$  phase transition in an Ising system to occur at a field such that the first term in Equation 1.1 (which promotes order and has magnitude equal to  $k_B T_c$ ) is the same order of magnitude as the second term (which promotes

---

<sup>†</sup> The magnetic field strength can be expressed in degrees Kelvin by calculating the temperature which would produce an equivalent Zeeman splitting, this is,  $\mu_{ho}h = k_B T$  (where  $\mu_{ho}$  is the effective magnetic moment of the Ho ions).

paramagnetism and has an order of magnitude equal to  $\mu_{\text{eff}}H_c$ ). This effect is believed to be caused by the presence of the hyperfine interaction term in the Hamiltonian (see Section 2.3).

There are three interesting features of the  $\chi_{\text{AC}}$  data in a transverse field which should be noted. First, the susceptibility can be expanded in powers of the size of the probing field  $h$  (which is applied along the Ising axis) as:

$$\chi = \chi_1 - 3\chi_3 h^2 - 5\chi_5 h^4 + \dots \quad (2.3)$$

$\chi_3$  in this equation was defined by the authors of reference [30] as the “nonlinear susceptibility”. This quantity is shown as a function of external field ( $H$ , applied transverse to the Ising axis) in the top panel of Figure 2.6, and the position of the maximum in this quantity was used to trace the phase boundary in Figure 2.5. Notice in this figure that  $\chi'_3(H)$  diverges at the phase boundary when the temperature of the system is close to the zero field  $T_g$ . This behavior agrees with what it is expected at a spin glass phase transition [8]. Nevertheless, if the temperature is reduced, the singular behavior is suppressed [30]. This phenomena is believed to be an effect of the presence of field induced random fields in  $\text{LiHo}_{0.167}\text{Y}_{0.833}\text{F}_4$  (see Section 2.3).

The second interesting aspect of the  $\chi_{\text{AC}}$  data of the  $x=0.167$  system is illustrated in the lower panel in Figure 2.6. Here it can be observed that the dissipative component of  $\chi_1$  becomes different from zero at a field  $H_c$  which is a function of the temperature. This onset of dissipation happens at a higher field than  $T_g$  and delimits a “crossover” region in Figure 2.5 from the paramagnetic state into the glassy one.

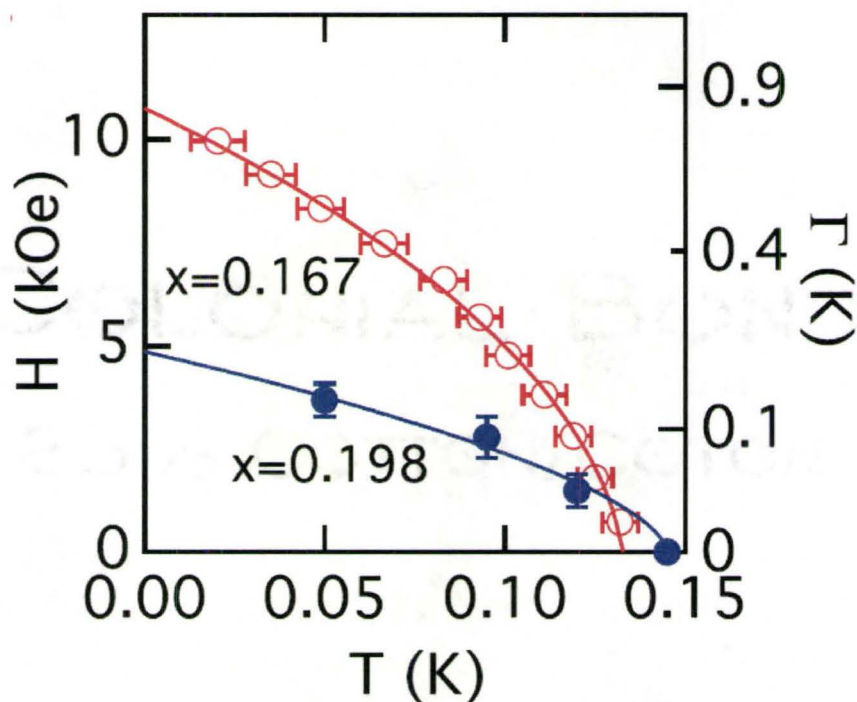


Figure 2.5: Field vs temperature phase diagram as measured by  $\chi_{AC}$  (at 1.5Hz) for the  $x=0.198$  and  $0.167$  system with a spin glass state existing below the dome and paramagnetism outside it. As will be seen in Section 2.3,  $\Gamma \propto H^2$ , where  $H$  is an external field transverse to the Ising axis.  $T_g$  is defined as the point where  $\chi_1''$  gets a flat spectral response (see Figure 2.6). Filled blue circles delimit the phase boundary for  $x=0.198$ , and the red empty ones does it for  $x=0.167$ . Taken from Ancona-Torres *et al.* (2008) [22].

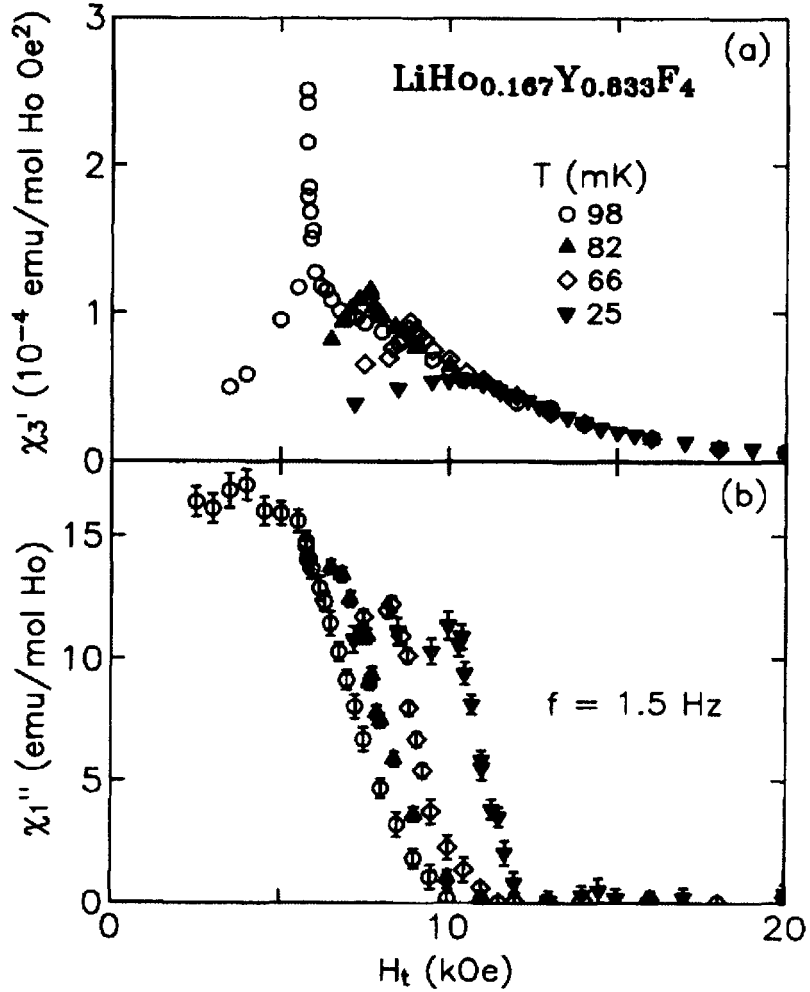


Figure 2.6: Top panel: real component of the nonlinear magnetic susceptibility ( $\chi_3'$ ). Bottom panel: imaginary part of the linear susceptibility ( $\chi_1''$ ). Both panels show data for the  $x=0.167$  system as a function of transverse field, at four temperatures, and at a frequency of 1.5 Hz for the probing field. Taken from Wenhao Wu *et al.* (1993) [30]. Notice that this work uses the symbol  $H_t$  to refer to  $H$ .

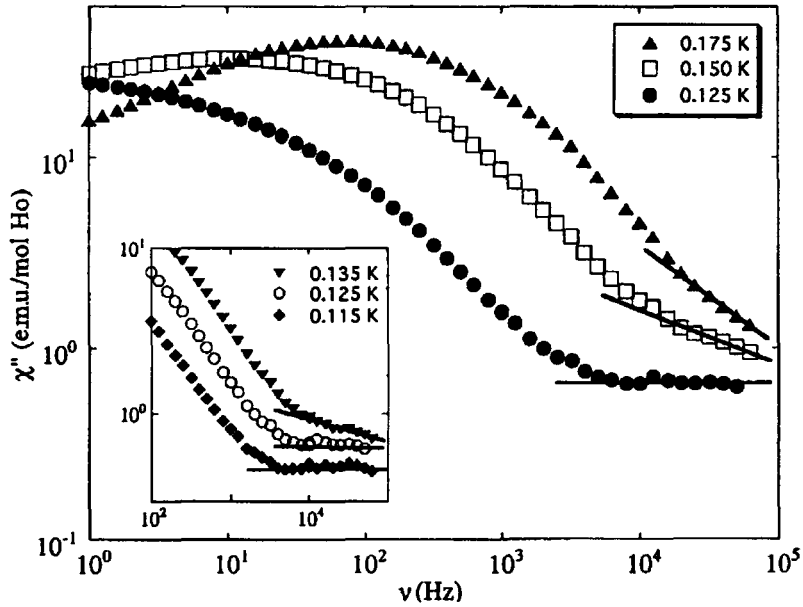


Figure 2.7: Imaginary part of the linear susceptibility as a function of frequency for the  $x=0.167$  ( $T_g = 0.13\text{K}$ ) sample and in zero external field. The inset is a detail plot of the data near  $T_g$ . Taken from D. Bitko *et al.* (1996) [31].

The third interesting feature of the  $\chi_{AC}$  response of the  $x=0.167$  system is that, contrary to what is observed in canonical spin glasses, the high frequency response of  $\chi''_1$  becomes frequency independent and constant below  $T_g$  (see Figure 2.7) [31].

Recent studies which aim at extracting  $T_g$  for  $x=0.167$  from the critical region slightly above the  $\chi''_3$  peak (where the system is in equilibrium), indicate that there is no spin glass transition in  $x=0.167$  [32] [33]. These studies also mention that the collective behavior in this system is somehow quenched by the hyperfine interactions. The existence of a spin glass state in  $\text{LiHo}_{0.167}\text{Y}_{0.833}\text{F}_4$  is an ongoing debate [22] [33].

There are many open experimental questions about the nominally spin glass state of  $\text{LiHo}_x\text{Y}_{1-x}\text{F}_4$ . First, there is no consensus about the nature of the low temperature phase (spin glass, cluster glass or paramagnet). Therefore, also the nature of the “crossover” region is still not well defined. Another point that should be addressed by experiments regards the surprising frequency independent behavior of  $\chi''$  at high frequencies. This response should be independently confirmed with by other techniques, and its behavior should be mapped at higher frequencies.

### 2.2.3 The “antiglass” phase

If the value of  $x$  is further decreased the system is driven into what has been labeled as the “antiglass” state. The peculiar behavior in this part of the phase diagram was brought to the attention by early AC susceptibility measurements of the  $x=0.045$  compound. These measurements showed a qualitatively different behavior from that of the glassy  $x=0.167$  system. The difference can be observed in Figure 2.8. The most important feature in this figure is that for the  $x=0.045$  system, the scaled  $\chi''_{AC}$  narrows upon cooling[20]. This is in contrast to what is expected for a spin glass where the scaled susceptibility broadens as the temperature is lowered (due to the many different relaxation times which characterize the glass state), effect which is observed in the  $x=0.167$  system. This effect was first interpreted as a tendency of the  $x=0.045$  system towards a single relaxation time (or energy barrier) as its temperature is decreased, hence the name “antiglass” [34].

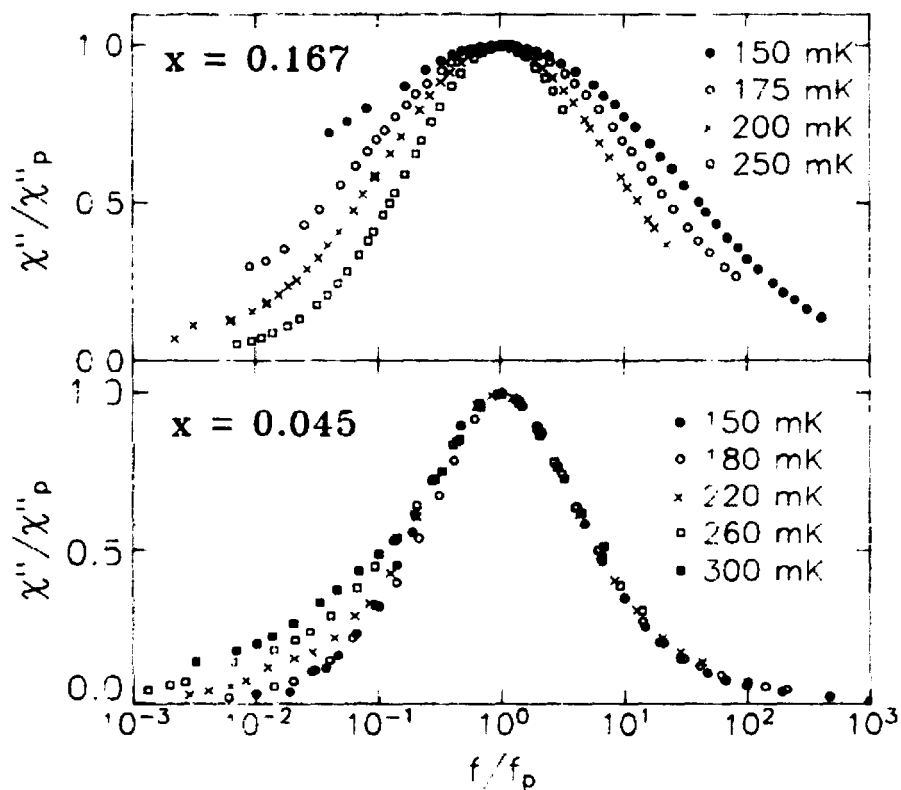


Figure 2.8: Imaginary component of  $\chi_{AC}$  scaled by the position and amplitude of the peak. Notice that the  $x=0.167$  response widens upon cooling against the narrowing observed in the  $x=0.045$  sample. Taken from D. H. Reich *et al.* (1990) [20].

Further measurements of  $\chi''_{AC}$  by the same group in the same  $x=0.045$  system but at lower temperatures, showed a dissipative response which is narrower than what is expected by the Debye form (which assumes a single relaxation time and is given by  $\chi_{AC} = \chi_0/(1 + \omega\tau)$ ). This suggested that the behavior of the system at low temperature is not dictated by a relaxation time but it is more like that of an ensemble of harmonic oscillators [35]. This picture was further supported by the observation of long relaxation times of the magnetization ( $\sim 1$ sec), which kept oscillating after a 0.2G oscillating external field was turned off. This whole phenomenology was explained as coherent oscillations of clusters of spins ( $\sim 100$  spins) with very long correlation times. One of the consequences of this interpretation is that these clusters of spins would have to have  $\langle J_{total} \rangle = 0$  in order to avoid freezing into a glassy state.

Recent AC susceptibility measurements, by a different experimental group, on the  $x=0.045$  system have actually seen a broadening of the scaled  $\chi''$  vs. frequency curve [36] in agreement with a spin glass ground state and in contrast to previous measurements [34]. They also predict a  $T_g$  of 42mK by looking at the temperature evolution of the characteristic timescale of the system. These measurements also see a high frequency tail which does not match the Debye expected behavior. It was pointed out in this study that this might be a signature of a distribution of characteristic time scales dictating the behavior of the system.

Specific heat measurements of  $x=0.018$ , 0.045 and 0.08 have been performed in zero external field, down to  $T \approx 0.07$ K [37]. These measurements showed a broad maximum at  $T \approx 0.12$ K (there seems not to be any dependence

of the maximum with  $x$ ). After integrating  $C/T$ , it was found an increase in residual entropy as Ho concentration is diminished (as a percentage of  $R\ln 2$ : 44% for  $x=0.018$ ; 30% for  $x=0.045$  and 0 for  $x=0.08$ ). This observation is consistent with the lack of a spin glass transition reported in some Monte Carlo studies [38]. It should be mentioned that previous measurements of specific heat in the  $x=0.045$  system by a different group using a different crystal, displayed a very different temperature behavior. These measurements showed two narrower peaks at  $\sim 0.11\text{mK}$  and  $\sim 0.3\text{mK}$  [39].

If  $x$  is further diluted down to 0.002 a “mostly single ion” behavior is attained. This fact makes  $\text{LiHo}_x\text{Y}_{1-x}\text{F}_4$  a very attractive system to study the quantum dynamical behavior of two-level systems coupled to a spin/phonon bath. In this regard, it has been observed that, when a magnetic field is applied along the  $\hat{c}$  direction, enhancement of the magnetic moment relaxation is observed at the single ion “avoided level crossing” positions [16] [40] [41]. Even though, smaller effects of coherent interactions are still apparent at this low value of  $x$ . These coherent processes have been observed as an increase in relaxation of the  $\hat{c}$  axis magnetization due to two-moment flip processes [42] [43].

We have shown that the experimental picture of the “antiglass” region of the phase diagram is incomplete and contradictory. In particular, the interpretation of experimental data in terms of independent spin clusters (like the slowly decaying magnetization explained by coherent oscillations of these clusters) is hard to conceive if one remembers that magnetic moments in this system interact through long range dipolar fields (unless chemical segregation

is present in the system) [44]. More experimental data with different probes and in different samples is necessary to rule out experimental and/or sample biases.

## 2.3 Theoretical studies of $\text{LiHo}_x\text{Y}_{1-x}\text{F}_4$

We will present now the theoretical state of affairs of  $\text{LiHo}_x\text{Y}_{1-x}\text{F}_4$  organized in two subsections. The first subsection presents theoretical aspects of the ferromagnetically ordered state and, the second one, presents studies that deal with the glassy or magnetically random phase. The reason for not having a third section, that of the “antiglass”, is because researchers have not found any theoretical evidence for the existence of this state.

### 2.3.1 The ferromagnetic state

$\text{LiHo}_x\text{Y}_{1-x}\text{F}_4$  was expected to be a physical realization of the TFIM. This idea is based on two facts: first, the crystal field ground state doublet possesses an Ising character; and second, the dipolar, exchange and hyperfine interactions are much smaller than 11K, which is the distance from the ground state doublet to the first excited crystal field level (and therefore these terms can not mix the ground state doublet with higher crystal field levels). Then, if  $g_L\mu_B H \ll 11\text{K}$ , the system would be expected to be described by a TFIM. To see how the TFIM arises, the Hamiltonian in Equation 2.1 can be projected into the lowest crystal field doublet. This reduces the size of the Hilbert space for a  $\text{Ho}^{3+}$  ion from that of a  $J = 8$  multiplet to an effective  $S = 1/2$  model.

If this projection is performed, and the hyperfine interaction is neglected for the moment, the following effective Hamiltonian is obtained for the case when  $x=1$  [15]:

$$H_{\text{eff}} = \Delta^2(H) \left[ \frac{1}{2} \frac{\mu_0}{4\pi} \left( \frac{g_{\parallel} \mu_B}{2} \right)^2 \sum_{i \neq j} D_{ij}^{zz} \sigma_i^z \sigma_j^z + \frac{1}{2} J'_{\text{ex}} \sum_{i,d} \sigma_i^z \sigma_j^z - H_{\text{eff}}(H) \sum_i \sigma_i^x \right] \quad (2.4)$$

where  $\Delta^2$  is an overall factor which depends on the external transverse field  $H$ ,  $\sigma_i^y$  are the Pauli matrices,  $g_{\parallel}$  is the renormalized Lande factor along the Ising direction,  $J'_{\text{ex}}$  is a renormalized exchange interaction and  $H_{\text{eff}}$  is an effective external transverse field which has a nonlinear dependence on  $H$  ( $\Gamma = H_{\text{eff}}$  on Figure 2.5, the dependence of  $H_{\text{eff}}$  on  $H$  is shown in Figure 2.9). It is important to mention that a nonlinear dependence of  $H_{\text{eff}}$  on  $H$  is expected [45]. This is because, as was mentioned on Section 2.1,  $\langle J^x \rangle = 0$  within the ground state doublet of the crystal field. Then, if the effect of the transverse field is introduced in a perturbation scheme, the first order contribution is zero and the lowest order contribution is quadratic in  $H$ .

It can be seen that the effective Hamiltonian in Equation 2.4 is that of the TFIM (see Equation 1.1) with dipolar plus exchange interactions. There has been considerable debate about the validity of this projected Hamiltonian. Other researchers have proposed that not only the lowest Ising levels have to be included explicitly in the calculations, but also the first excited crystal field one [45] [46] [47]. Including the first excited level is needed since it couples the

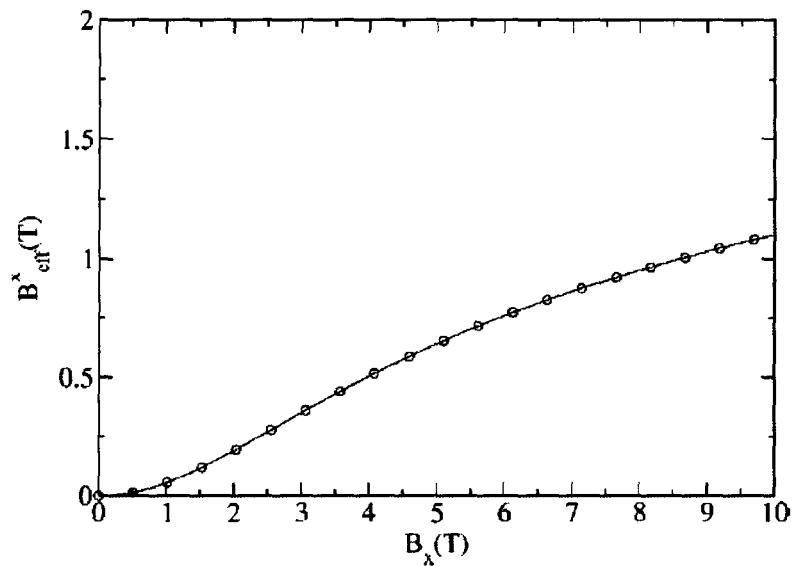


Figure 2.9: Effective transverse field in  $\text{LiHo}_x\text{Y}_{1-x}\text{F}_4$  as a function of real external transverse field  $H$ . Taken from P. B. Chakraborty *et al.* (2004) [15]. Notice that this work uses the symbols  $B_{\text{eff}}^x$  and  $B_x$  to refer to  $H_{\text{eff}}$  and  $H$  respectively.

lowest hyperfine Ising levels when a transverse field is present. This approach, which has been applied mostly to the spin glass region of the phase diagram, has been shown to be equivalent to that of the projected TFIM though (in the low field limit where Equation 2.4 is valid) [48]; and then, for the rest of this section we will deal only with the results found using the projected TFIM.

The Ising Hamiltonian in Equation 2.4 has been used to compute the  $H$ - $T$  phase diagram for  $x = 1$ , with  $J'_{\text{ex}}$  as a parameter constrained to reproduce the experimental  $T_c$  in zero external field [15]. This phase diagram is shown in Figure 2.3 as the “A=0” line. It can be observed that the hyperfine interactions must be included in the Ising Hamiltonian in order to reproduce the upturn of the ferromagnetic state at low temperatures [24]. This interesting phenomena can be understood qualitatively by considering only the single ion part of the full Hamiltonian in Equation 2.3. As mentioned before, the ground state of the crystal field is an Ising doublet; the hyperfine interaction splits this doublet into 8 doubly degenerate levels 200mK apart (remember that the nuclear spin is  $7/2$  and has multiplicity equal to  $2*7/2+1$ ). This multiplet has  $|\uparrow, -7/2\rangle$  and  $|\downarrow, 7/2\rangle$  as its ground state (in these kets the first component indicates the electronic Ising state, while the second component indicates the state of the nuclear spin). It can be shown that a small transverse field couples  $|\uparrow, -7/2\rangle$  with  $|\downarrow, -7/2\rangle$ , but not with  $|\downarrow, 7/2\rangle$ , which is the other Ising level that is now weakly coupled to  $|\uparrow, 7/2\rangle$  [45]. Then, the hyperfine coupling “protects” the system against fluctuations between the spin up and spin down electronic states and reduces the effectiveness of the field in destroying the ferromagnetic state.

The properties of  $\text{LiHoF}_4$  in zero external transverse magnetic field seem to be well understood. Recent Monte Carlo calculations of  $\text{LiHoF}_4$  show that the dipolarly coupled Ising model with nearest neighbor antiferromagnetic exchange (which is the only free parameter of the model), can reproduce quantitatively specific heat, order parameter and magnetic susceptibility measurements in zero external field [49].

When an external field transverse to the Ising axis is present though, the agreement of the theory and experiment is just qualitative, as shown in calculations of the  $H$ - $T$  phase diagram [13] [15] and excitation spectrum [17]. In particular, close to  $T_c$  and  $H=0$ , the theoretically predicted  $H$ - $T$  phase diagram grows slower upon decreasing  $T$  than what it is experimentally observed (see Figure 2.3). In order to understand the disagreement between the calculated and measured  $H$ - $T$  phase diagram, researchers have shown that variations in the crystal field parameters [13] [17] and different ways of handling the long range dipolar interactions [13], cannot account for the discrepancy. It has been proposed that, in order to reconcile theory and experiment, other factors need to be considered in calculations. These factors include effect of domain wall structure, magnetoelastic effects, distortion of the crystal field structure by the presence of different Li isotopes and higher order exchange interactions [13] [17] .

We now consider the effect of magnetic dilution in the  $x=1$  ferromagnetic Hamiltonian. Early mean field calculations show that, for a dipolarly coupled Ising system in zero field [50],  $T_c$  should decrease mean field like (linearly) with magnetic dilution for  $T_c \gtrsim D_{nn}$  ( $D_{nn}$  is the dipolar interaction strength

between nearest neighbor Ho ions). Then, for  $T_c < D_{nn}$ , the dependency of  $T_c$  with  $x$  is expected to leave its linear trend and, depending on the symmetry of the lattice <sup>‡</sup>, the ferromagnetic region can end at  $x_c$ , where a spin glass ground state could arise. Recent Monte Carlo simulations have used a dipolar-plus-exchange Ising model to study the  $x$ - $T$  phase diagram in zero external field. These calculations, which take into account the right shape of the magnetic domain to avoid shape effects [51]), obtained results that have a good agreement with the experimental boundary of the ferromagnetic state [52] [53] (see Figure 2.10). These calculations, which used the nearest neighbor exchange interaction as a parameter to obtain the right  $T_c$  at  $x=1$ , also predict that ferromagnetism should terminate at  $x_c = 0.24 \pm 0.03$  [53].

An other theoretical work in the diluted ferromagnetic state support the existence of a ferroglass ground state in the  $x=0.44$  system [28]. This study pointed out that a mean field calculation using the Sherrington-Kirkpatrick model (Section 1.3), with an external field along the Ising direction, predicts different values of magnetization for zero field cooled and field cooled protocols. This behavior recalls the experimentally observed bifurcation of  $\chi'$  for these same two processes when cooling the  $x=0.44$  system into the ferroglass state [28].

It has been noted recently that when  $x < 1$ , and the external magnetic field is nonzero, random internal fields are generated in the Hamiltonian of

---

<sup>‡</sup> The symmetry of the lattice has a direct effect on the “strength” of the ferromagnetic interaction (that is  $T_c$ ) which at low values of  $x$  has to compete against spin glass order.

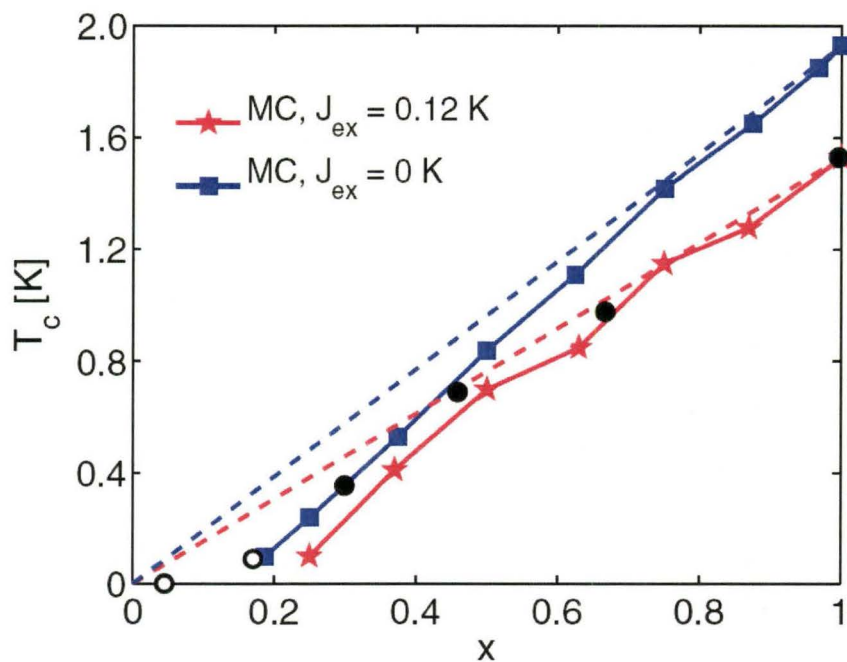


Figure 2.10: Theoretical  $T$ - $x$  phase diagram. Filled circles are experimentally determined  $T_c$ , empty circles are experimental  $T_g$ , blue squares are theoretical values of  $T_c$  where exchange interaction has been neglected, and red stars are  $T_c$  values for the same model where nearest neighbor exchange interactions have been introduced. Taken from A. Biltmo *et al.* (2007) [52].

LiHo<sub>x</sub>Y<sub>1-x</sub>F<sub>4</sub> [46] [54] [55]. It can be shown that the effective spin 1/2 Hamiltonian for  $x < 1$  is given by [54]:

$$\begin{aligned}
 H_{\text{eff}} = & D_1(H) \sum_{i,j} \epsilon_i \epsilon_j D_{i,j}^{zz} \sigma_i^z \sigma_j^z - H_{\text{eff}}(H) \sum_i \sigma_i^x + \\
 & J'_{\text{ex}}(H) \sum_{i,j} \epsilon_i \epsilon_j \sigma_i^z \sigma_j^z + D_2(H) \sum_{i,j} \epsilon_i \epsilon_j D_{i,j}^{xz} \sigma_i^z + \\
 & D_3(H) \sum_{i,j} \epsilon_i \epsilon_j D_{i,j}^{xx} \sigma_i^x \sigma_j^x \quad (2.5)
 \end{aligned}$$

The first three terms in this equation correspond to the Hamiltonian in Equation 2.4 (taking  $\epsilon=1$ ). The following two terms are the random field terms and they are not present in the Hamiltonian 2.4 because that Hamiltonian corresponds to the  $x=1$  system where these terms cancel by symmetry. Randomness, which breaks the symmetry, is explicitly contained in the Hamiltonian through the  $\epsilon$  variables. These variables take a value of 1 if a given site is occupied by a magnetic holmium, and 0 if the site is occupied by a non magnetic yttrium.

In zero external field the random field terms  $D_2(0) = D_3(0) = 0$ . That is, these terms are not only tuned by  $H$  but they are zero when the external field is zero. As a consequence, in zero external field, LiHo<sub>x</sub>Y<sub>1-x</sub>F<sub>4</sub> should be still described by a TFIM with hyperfine interactions.

The random field terms in the Hamiltonian 2.4 can be expressed in terms of the more familiar Random Field Ising Model (RFIM) if the random field terms are treated within a mean field approximation. If this is done then the

two last terms are substituted by terms depending on  $\langle \sigma_i^x \rangle \sigma_j^z$  and  $\langle \sigma_i^z \rangle \sigma_j^x$  which represent longitudinal and transverse random fields respectively.

A mean field calculation with the RFIM Hamiltonian have shown that the random fields are responsible for the increased effectiveness of the transverse field on destroying the ferromagnetic state as  $x$  is decreased [54] [56].

### 2.3.2 The spin glass state

The existence and nature of the spin glass state is not only an experimental debate but also a theoretical one. In this section we present first theoretical results which support (or just assume) the existence of a spin glass phase at low values of  $x$  in  $\text{LiHo}_x\text{Y}_{1-x}\text{F}_4$ . After this we will review the theoretical studies which find no evidence for the existence of a spin glass phase. We will end the section with a comment regarding the theoretical perspective of the “antiglass” region.

As mentioned in the previous section, early mean field calculations using a long ranged TFIM, predicted that dilution could destroy the ferromagnetic state and give rise to a spin glass [50]. These calculations also predicted that, due to the long range of the dipolar interactions, the spin glass state should persist down to  $x=0$ .

Many experimental features of the spin glass state have been explained qualitatively by theory. Calculations using a quantum spherical spin glass model with Gaussian distributed infinite ranged interactions found that the nonlinear susceptibility at low frequencies should not diverge if the system is

close to the quantum critical point (where spin glass order is destroyed with transverse field) [57]. We may recall from Section 2.2.2 that the nonlinear susceptibility of the  $x=0.167$  system was actually observed not to diverge in the presence of an external transverse field. However one difference between the experiment and the theoretical work is that in the experiment the system displays the quenched divergence even away from the quantum critical region. Other quantum Monte Carlo simulations using the same model, but this time with Ising spins, found that the low frequency behavior of  $\chi''$  was similar to that found in  $\text{LiHo}_{0.167}\text{Y}_{0.833}\text{F}_4$  [58].

It was not until recently that calculations on the spin glass state have started to consider two important aspects of  $\text{LiHo}_x\text{Y}_{1-x}\text{F}_4$ . First, it was realized that in the spin glass regime the hyperfine energy scale is the same size as (or even bigger than) the average dipolar interaction. This means that the hyperfine interaction cannot be neglected even close to the spin glass transition in zero field (classical regime) [45] [47]. Including this interaction in calculations could explain the surprisingly high  $T=0$  critical field (compared with  $k_B T_g$ ) observed in  $\text{LiHo}_{0.167}\text{Y}_{0.833}\text{F}_4$  [45], in analogy with what was already pointed out in the case of the  $x=1$  system [24].

The second aspect which was recently considered in theories aiming to describe the behavior of the spin glass phase, regards the role of the transverse and longitudinal random fields [59] [45]. Transverse-field-induced random fields can be responsible for the broadening of  $\chi'_3$  in the  $x=0.167$  system (see Figure 2.6) as the temperature decreases [54]. In particular it has been shown that the inclusion of the random longitudinal fields in the calculation

(that is, working with the full Hamiltonian in Equation 2.5), can destroy the spin glass order for any  $H \neq 0$  [46], as it had been previously shown for the case of an Ising spin glass model with random fields [60]. An effect of including random fields in the Hamiltonian is that they could prevent from observing the critical exponents characteristic of a quantum critical phase transition [46] [54].

As pointed out at the beginning of this section, some theoretical studies have not found any evidence of the spin glass phase. Monte Carlo simulations of diluted systems of classical Ising spins on a cubic lattice have shown that, in contrast to the previous consensus on the existence of a spin glass state in long range coupled classical Ising systems [50], below a critical concentration  $x_c \approx 0.2$  no spin glass order is attained [38]. Further Monte Carlo simulations using dipolar-plus-exchange coupled classical Ising spins in zero transverse field, analyzed the specific case of  $\text{LiHo}_x\text{Y}_{1-x}\text{F}_4$ . These studies found that, after ferromagnetism disappears at  $x_c = 0.24 \pm 0.03$  (see Figure 2.10), no spin glass order is attained at any doping and speculated that offdiagonal terms of the Hamiltonian might be needed to stabilize the spin glass phase [52] [53]. A more recent Monte Carlo study has found evidence of a spin glass state though, and postulate some reasons why the above mentioned works failed to find it [61].

We end here our review of the theoretical studies of the spin glass phase of  $\text{LiHo}_x\text{Y}_{1-x}\text{F}_4$  but, before finishing, we would like to make a brief remark about the “antiglass” phase. Most theoretical works do not find a difference between the spin glass region and the “antiglass” one. This is, they do not

observe any new physical behavior as  $x$  is reduced in the spin glass state. One study has dealt specifically with the  $x=0.045$  system and it predicts a low temperature phase which is most probably a spin glass [55]. In an other work, researchers have been able to calculate rather accurately the magnetic susceptibility and specific heat of the “anti-glass” sample using a “pair wise decimation procedure” on a diluted lattice of spins with uniaxial anisotropy [39]. It should be noted that this procedure, which promotes the formation of spin singlets, might not be well suited to study dipolar random systems, which probably have spin glass ground states. Also, as mentioned in Section 2.2.3, the behavior of the specific heat that this study report and describe, could not be reproduced by another research group which used a different crystal [37].

## 2.4 Study of $\text{LiHo}_x\text{Y}_{1-x}\text{F}_4$ using $\mu\text{SR}$

One of the consensuses of the scientific community about  $\text{LiHo}_x\text{Y}_{1-x}\text{F}_4$  is that more experimental data with different magnetic probes is necessary. In order to start filling this scientific necessity, we performed Muon Spin Rotation/Relaxation ( $\mu\text{SR}$ ) measurements in five different samples with dilutions  $x=1, 0.45, 0.25, 0.12, 0.08, 0.045$  and  $0.018$ . This set of samples cover the whole phenomenology of  $\text{LiHo}_x\text{Y}_{1-x}\text{F}_4$ : parent ferromagnet, diluted ferromagnet, ferromagnet/ferroglass, ferromagnet/spin glass, spin glass, spin glass/“antiglass”, “antiglass”, “antiglass”/single ion. Two of these dopings ( $x=1$  and  $0.045$ ) have been studied previously with bulk sensitive techniques, so our results can be compared directly with other experimental probes. The rest of our samples had not been measured before at the time we started our studies (specific heat

data in these samples has already been published by our collaborators for the  $x=0.08$ ,  $0.045$  and  $0.018$  systems[37]) and therefore they can contribute for a better mapping of the  $x$ - $T$  phase diagram.

$\mu$ SR is a very sensitive magnetic probe of magnetism, which has the advantage of being local ( $\mu$ SR integrates over  $Q$  space). From this point of view our work fills an important void since, as was mentioned before, most of the experimental data has been obtained using bulk probes like magnetic susceptibility (which probes only  $Q = 0$ ).  $\mu$ SR also fills another gap, it probes the system at shorter time scales.  $\chi_{AC}$  measurements can be performed up to  $10^5$  Hz. Our  $\mu$ SR time window ranges from  $10^4$  Hz to  $10^7$  Hz, so our measurements probe the system in a time window which is faster than that of the magnetic susceptibility.

Some of the questions we address with our measurements are: What is the low temperature dynamical behavior over the phase diagram? How do hyperfine interactions manifest themselves in the magnetic behavior? Can  $\mu$ SR give evidence of ferroglass and/or spin glass behavior? What is the nature of the antiglass phase from the  $\mu$ SR point of view?

## Chapter 3

### Muon spin relaxation/rotation

The technique we have used to explore the magnetism of  $\text{LiHo}_x\text{Y}_{1-x}\text{F}_4$  is muon Spin Relaxation/Rotation. In this chapter we first present a brief introduction to this technique and to the experimental setup (the reader interested to learn  $\mu\text{SR}$  in more detail should consult References [62] [63] [64]). Then, we discuss some standard techniques to model  $\mu\text{SR}$  line shapes and we present our original contributions to this matter.

#### 3.1 The basic concept

$\mu\text{SR}$  stands for muon Spin Rotation, Relaxation or Resonance; depending on the experimental setup. All these setups have in common that they all use muons implanted in samples to study the internal magnetic field at the atomic level. Nevertheless, we have performed our measurements using the Rotation and Relaxation setups, and therefore we do not discuss the Resonance one (the reader interested on it should consult the literature [62]). Also, muons can have positive or negative charge and, since our measurements were carried

out using positive muons exclusively, the rest of this writeup assumes that the implanted muons are positive.

Muons are elementary particles with a mass of  $1.883 \times 10^{-28}$  kg ( $\approx 0.113$  times the mass of a proton), charge  $e$  and spin  $1/2$  with a gyromagnetic ratio  $\gamma/2\pi = -135.5$  MHz/T ( $\mu_\mu = -4.841 \times 10^{-3} \mu_B$ ). A beam of almost 100% polarized muons (polarized in the direction opposing their momentum) can be obtained from the decay of pions through the following reaction:



The pions required to produce the muons can be created by colliding high energy particles against a light target (e.g. protons against a carbon or beryllium target for example). The spin of the muons emerging from this decay is highly polarized thanks to the fact that the pion decay is weak, and therefore it violates parity conservation [65]. In fact, if the decay occurs with the pion at rest, the muon beam can be almost 100% polarized. A muon beam created from pions which are at rest in the surface of the production target, is referred as a surface muon beam.

The muons produced from pion decay can be collected and delivered to the sample using magnetic fields. Surface muons arrive to the sample with a kinetic energy of 4.110 MeV. Once the muons enter the sample they rapidly thermalize, first by ionization of the atoms and scattering from electrons, then by several stages of muonium\* formation/dissociation, and finally by exciting

---

\* Muonium is the bound state of a positive muon and an electron, this state is analogous to a hydrogen atom [66] [67].

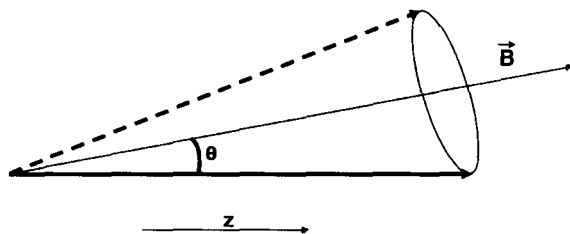


Figure 3.1: Diagram of the muon spin precessing in the presence of a field  $\vec{B}$  which makes an angle  $\theta$  with the initial muon spin direction  $z$ .

phonons in the material. During the process of thermalization the muons do not lose their polarization [62], furthermore, the thermalization process is so fast ( $\sim 1\text{ns}$ ) that for practical purposes the slowing down process can be considered essentially instantaneous. The thermalized muons will occupy a minimum of the electrostatic potential between the atoms of the material and, depending on their temperature and the local environment, they can either remain there or hop from one site to another.

A muon will couple to the local magnetic field ( $\vec{B}$ ) through its magnetic moment. If this magnetic field is constant in time, let's say, a classical picture tells us that the muon spin is going to precess around this field as shown in Figure 3.1. Let's designate the initial muon spin direction as  $\hat{z}$ , then the component of the muon spin along this direction ( $g_z$ ) is going to be given by:

$$g_z(t) = \cos^2(\theta) + \sin^2(\theta) \cos(\gamma|\vec{B}|t) \quad (3.2)$$

We can measure experimentally  $g_z$  in the following way. Muons are not stable particles, they have a mean lifetime ( $\tau$ ) of  $2.197\mu\text{s}$  and they decay by emitting a positron and two neutrinos through the following reaction:

$$\mu_+ \rightarrow e^+ + \nu_e + \bar{\nu}_\mu \quad (3.3)$$

The positron from the decay is emitted preferentially along the muon spin direction (the decay is asymmetric) with the following probability distribution:

$$W(\phi) \propto 1 + a \cos(\phi) \quad (3.4)$$

where  $\phi$  is the angle between the muon spin direction and the direction of the emitted positron, and  $a$  is a constant which depends on the energy of the emitted positron. Then, if we perform an experiment where we implant millions of muons into a sample and the muons precess accordingly to Equation 3.2, the number of positrons that is going to be emitted along the  $z$  direction ( $n_f$ ) at a given time  $t$  is given by:

$$n_f(t) \propto e^{-t/\tau}(1 + a \cos(\phi)) = e^{-t/\tau}(1 + ag_z(t)) \quad (3.5)$$

In the same way, if we monitor the number of muons that decay along the  $-z$  direction, the number of positrons that we would observe would be proportional to:

$$n_b(t) \propto e^{-t/\tau}(1 + a \cos(\pi - \phi)) = e^{-t/\tau}(1 - ag_z(t)) \quad (3.6)$$

Then if we record the information from both sets of detectors, along  $z$  (forward) and along  $-z$  (backwards), we can get a quantity proportional to  $g_z$  (called the forward-backward asymmetry or just asymmetry) by writing:

$$A_z(t) = \frac{n_f(t) - n_b(t)}{n_f(t) + n_b(t)} = ag_z(t) \quad (3.7)$$

It can be seen that the initial amplitude of Equation 3.7 is different from 1 due to the factor  $a$ , and has values between 0.2 to 0.3. The  $\mu$ SR signals (also referred as spectra) presented in further chapters have amplitudes different from unity due to this factor. The precise value of  $a$  depends on the energy of the positrons detected (which measures the level of asymmetry in the muon decay) and the geometry of the experimental setup. This number is constant for a given experiment and it is usually obtained when analyzing the data by making the total amplitude of  $A_z$  a fitting parameter. Also, it should be emphasized that the fact that the positron emission probability follows Equation 3.4, that is a cosine function, is what allows us to reconstruct  $g_z(t)$  using only two detectors (or counters).

In a real experiment the detectors have a finite size and they detect positrons within an energy range but, after integrating energy and solid angle, a set of equations equal to 3.5 and 3.6 is obtained but with new proportionality factors ( $N^0$ ) and amplitudes ( $a$ ). Both of these parameters will depend on the solid angle span by the detector and therefore will be different for each counter. Aside from this, the value of  $N^0$  is going to depend on the total amount of muons counted during the experiment and in the efficiency of the detectors. Further more, if an external magnetic field is applied, the positron trajectories are distorted changing effectively the efficiency of the counters and, therefore the value of  $N^0$ . With this in mind, we can rewrite Equation 3.7 as:

$$A_z(t) = \frac{N_f^0 n_f(t) - N_b^0 n_b(t)}{N_f^0 n_f(t) + N_b^0 n_b(t)} = \frac{(\alpha - 1) + (\alpha\beta + 1)a_b g_z(t)}{(\alpha + 1) + (\alpha\beta - 1)a_b g_z(t)} \quad (3.8)$$

where we have defined  $\alpha = N_f^0/N_b^0$  and  $\beta = a_f/a_b$ .  $\alpha$  is usually close to 1 but its exact value is usually determined in the data fit. A value of  $\alpha$  which is different from one has the effect of shifting the base line of the signal. A  $\mu$ SR signal which has been corrected for this effect, that is a signal with base line at zero, is usually referred as “corrected asymmetry”. Experimentally the value of  $\beta$  in Equation 3.8 is found to be very close to 1, and there fore it is usually set to this value.

## 3.2 Experimental setups

$\mu$ SR measurements are performed with two experimental setups. In the first one the initial muon spin direction is perpendicular to the externally applied magnetic field. This geometry is designated as “Transverse Field” (TF) and it is sketched in Figure 3.2. In this setup the spin of the muons is forced by the external magnetic field to perform full precessions, therefore these type of measurements can also be referred to as a “Rotation” experiment. This type of experiment is very similar to a free induction decay measurement in NMR.

The second geometry has the external field applied parallel to the initial muon spin direction. This setup is designated as “Longitudinal Field” (LF) and it is depicted in Figure 3.3. The case when the external magnetic field is zero can be considered a special case and it is designated as a “Zero Field” (ZF)

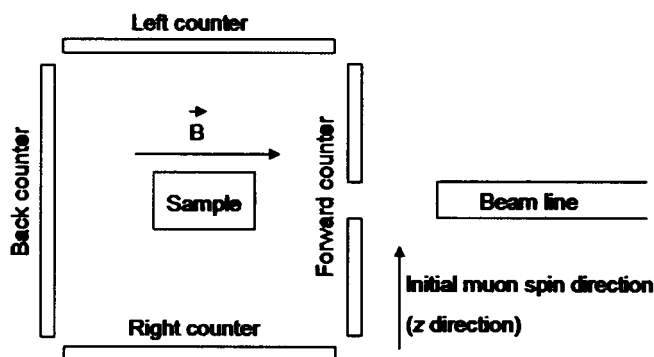


Figure 3.2: Experimental setup for a Transverse Field experiment. The muon is implanted with its spin perpendicular to the externally applied magnetic field. The asymmetry is constructed from the left and right counters.

measurement. If an LF (or ZF) setup is used, the initial muon polarization is left to freely relax or depolarize, this is the reason why this type of experiment can also be refer as a “Relaxation” experiment.

These two setups provide different and complementary information. A TF setup has the advantage that it can provide information in applied fields which are much bigger than the internal contribution of the sample to the total field. On the other side, LF measurements are able to distinguish between relaxation produced by static or dynamic magnetic environments. Finally, ZF measurements have the ability to probe a system in the complete absence of an external magnetic field.

### 3.3 Technical details of the $\mu$ SR experiment

We performed the  $\mu$ SR measurements at the M15 and M20 surface muons channels of the TRIUMF (Vancouver, Canada) national laboratory. On the

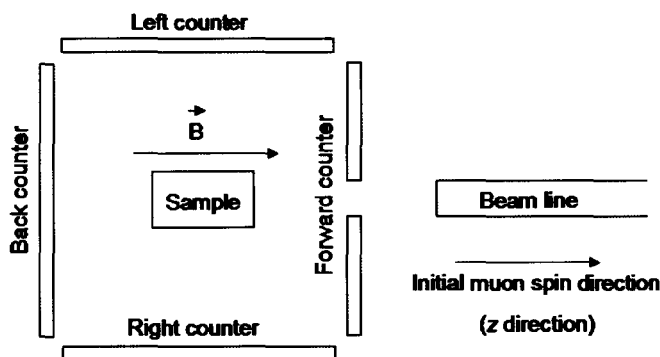


Figure 3.3: Experimental setup for a Longitudinal Field experiment. The muon is implanted with its spin parallel to the externally applied magnetic field. The asymmetry is constructed from the forward and backward counters.

M20 channel we utilized a Helium flow cryostat for temperature control of the sample. This cryostat can cover a temperature range between 1.8K and room temperature and therefore, it was used to perform all the high temperature measurements. These high temperature measurements were performed in ZF<sup>†</sup> and LF using the so called LAMPF spectrometer, which is capable of creating a maximum magnetic field in the sample of 0.3T. The samples were mounted in the cryostat using a low background sample holder. In this holder the samples are held in place by a Mylar tape which lies in front of the beam. This tape is thin enough so essentially 100% of the muons pass through it. There is a muon veto counter just behind the sample in this cryostat which allows us to discard all the muons which do not stop in the sample. The total number of muons counted in a typical run was  $\approx 6 \times 10^6$ .

<sup>†</sup> The field in the sample space is zeroed using a fluxgate magnetometer.

The M15 beam line also delivers surface muons. The temperature control of the sample in this beam line was achieved using an “Oxford Instruments” dilution refrigerator. This refrigerator allows for sample temperatures between 15mK and 10K. Then, this device allowed us to explore the phase diagram of  $\text{LiHo}_x\text{Y}_{1-x}\text{F}_4$  down to a temperature which is an order of magnitude smaller than the hyperfine interaction, and which is half the size of the characteristic dipolar interaction strength in our most diluted sample ( $x=0.018$ )<sup>‡</sup>. This dilution refrigerator has a superconducting magnet incorporated, which allowed us to apply magnetic fields up to 5T. The samples in this refrigerator are mounted on a silver sample holder, which is screwed to the mixing chamber. The silver sample holder allows for a good thermal contact between the mixing chamber and the sample. Also, since the nuclear magnetic moments of silver are very small ( $\approx 0.1\mu_n$ ), the fraction of muons which land on it depolarize very slowly, and therefore have a small effect on the total signal (an effect which can be corrected when fitting the data if needed). Most of the measurements in this refrigerator were performed in ZF and LF setups, but we also did some TF runs in the  $x=1$  and 0.45 systems. The TF geometry is achieved by rotating the initial muon spin direction by  $90^\circ$  using Wien filters (which create electric and magnetic fields at right angles) which are incorporated to the beam line.

---

<sup>‡</sup> In a continuous approximation the average distance between Ho ions is proportional to  $x^{-1/3}$ , then the dipolar interaction strength corresponding to this characteristic length is going to be proportional to  $x$ . The proportionality constant can be estimated by the numerically calculated ferromagnetic critical temperature in the absence of exchange interaction [13] and, then, the characteristic interaction energy scale as a function of  $x$  is given by:  $x \times 1.92\text{K}$ .

The beam of muons in TRIUMF is a so called continuous beam, where muons arrive one at the time to the experiment. This continuous beam allows us to have a very good time resolution (typically 0.6ns per bin in this experiment). This proved to be important for our experiment since, due to the large size of the  $\text{Ho}^{3+}$  moments, our muon ensembles relaxed very fast.

The experimental data presented in this thesis was analyzed using the “msrfit” program which is commonly used for fitting  $\mu\text{SR}$  spectra [68]. This program finds an optimal set of fitting parameters by minimizing the  $\chi^2$  function with respect to these parameters; and the minimization is performed with the MINUIT set of routines [69]. The program also uses DOPLOT to present graphically the experimental data together with the fitting function. The plots of the  $\mu\text{SR}$  data presented in this thesis were produced with this program. “msrfit” has the facility to allow for the fit of non-analytic functions through the use of numerical tables. We used this feature for analyzing part of our measurements.

### 3.4 Modeling of muon spin relaxation data

Equation 3.2 gives the evolution of the z component of the muon spin as a function of time for a given local magnetic field. The magnetic field at the muon site has different contributions which can be expressed as [63] [64]:

$$\vec{B} = \vec{B}_{\text{hf}} + \vec{B}_{\text{dip}} + \vec{B}_{\text{L}} + \vec{B}_{\text{dem}} + \vec{B}_{\text{dia}} + \vec{B}_{\text{ex}} \quad (3.9)$$

where  $B_{\text{hf}}$  is the contact hyperfine interactions of the muon with the local electronic spin density (*e.g.* spin density waves or RKKY interaction with localized magnetic moments);  $B_{\text{dip}}$  is the dipolar field created by all the magnetic moments at the muon site which are within a volume  $V$  (this contribution is usually calculated numerically by a direct sum over all the magnetic moments in the volume  $V$ , which is usually chosen as a sphere with a radius much greater than the distance between nearest neighbor magnetic moments);  $B_{\text{L}}$  is the magnetic field contribution by the bound currents at the surface of the cavity enclosing the volume  $V$  (which is zero if the magnetization of the system is zero);  $B_{\text{dem}}$  is the demagnetizing field inside the sample (which is shape dependent and it is also zero if the magnetization is zero);  $B_{\text{dia}}$  is the contribution from superconducting electric currents (in case the system is a superconductor<sup>§</sup>); and  $B_{\text{ext}}$  is the externally applied magnetic field. Notice that many of these contributions can change from one muon site to the next (*e.g.* in a spin glass the magnetic moments are frozen in random directions and every muon will see a different local magnetic arrangement), and then the polarization function from all the muon ensemble is going to be constituted from the addition of each of the individual local contributions. Furthermore, most of the times the local field will have a time dependence due to the spin dynamics. In this section we present how the the total polarization function can be calculated for different magnetic situations relevant to  $\text{LiHo}_x\text{Y}_{1-x}\text{F}_4$ .

---

<sup>§</sup> A material in the superconducting state has two main characteristics: it is a perfect conductor (it conducts electrical current without dissipation), and is a perfect diamagnet (it has a tendency to shield its interior from the external magnetic field by creating internal currents).

These theoretical polarization functions will then be used in Chapters 4 and 5 to fit the experimental  $\mu$ SR signals in order to extract physical information from the data.

### 3.4.1 Probabilistic models

Probabilistic models of muon polarization functions are useful to analyze data from disordered magnetic states (like paramagnets or spin glasses). These models assume that each muon, after thermalizing inside the sample, will precess in a local field which is randomly selected from a given probability distribution  $P(\vec{B})$ . Using Equation 3.2, we can write the ensemble average of the muon spin polarization, which we will call  $G_z$ , as:

$$G_z(t) = \int \left( \cos^2(\theta) + \sin^2(\theta) \cos(\gamma|\vec{B}|t) \right) P(\vec{B}) d\vec{B} \quad (3.10)$$

Different muons will then feel different fields and therefore precess at different rates. This will produce a dephasing of the spins and the overall polarization of the ensemble should therefore decrease. In the case where  $P(\vec{B})$  is the following spherically symmetric Gaussian distribution [70]:

$$P(\vec{B}) = \left( \frac{\gamma}{\sqrt{2\pi}\Delta} \right)^3 e^{-\gamma^2(B_x^2+B_y^2+B_z^2)/(2\Delta^2)} \quad (3.11)$$

the polarization function  $G_z$  can be analytically calculated and is given by:

$$G_z(t, \Delta) = \frac{1}{3} + \frac{2}{3}(1 - \Delta^2 t^2)e^{-\Delta^2 t^2/2} \quad (3.12)$$

where  $(\Delta/\gamma)$  is the standard deviation of  $P(\vec{B})$ . This equation is known as the Gaussian Kubo-Toyabe function. Notice the 1/3 persisting polarization of  $G_z$ , which means that in average 1/3 of the spin of the muon ensemble do not depolarize. Mathematically speaking, this is a consequence of integrating the  $\cos^2(\theta)$  term in Equation 3.12 which is positive for every  $\theta$ . Equation 3.12 is a good approximation to the polarization function that would be observed in a powder sample with randomly frozen 3D (Heisenberg) spins, with  $\Delta$  proportional to the magnetic moment size [71].

If a LF is applied in this scenario, the Gaussian distribution is shifted from the origin in the direction of the muon spin. In this case the integral in Equation 3.10 has to be performed numerically<sup>¶</sup>. Figure 3.4 shows  $G_z$  at several different fields. Note the increase of the persistent polarization, this phenomena is known as “decoupling”<sup>¶¶</sup>.

The effect of having different magnetic environments at the muon site can be taken into account by averaging Equation 3.12 over a suitable distribution of  $\Delta$ . Different magnetic environments can arise, for example, in magnetically diluted systems. In these systems all the muons which land near to a magnetic moment will see bigger random fields (characterized by a higher local value of  $\Delta$ ) than those muons which land far from a magnetic moment (characterized by lower local values of  $\Delta$ ). The distribution of  $\Delta$  can be assumed to be [73]:

---

<sup>¶</sup> All numerical integrations in this thesis were performed using a FORTRAN routine based on the trapezoidal rule [72]

<sup>¶¶</sup> When the external LF is increased so much that it becomes the dominant contribution to the local magnetic field, the muons are “decoupled” from the surrounding magnetic environment. At this point polarization is constant and almost equal to one.

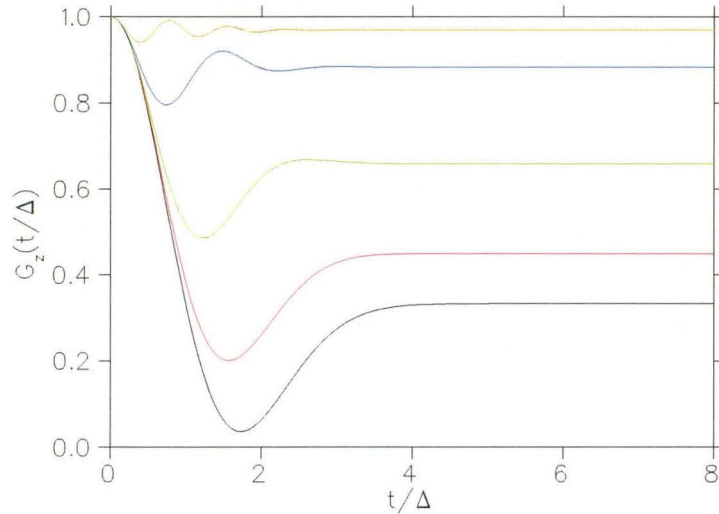


Figure 3.4: Gaussian Kubo-Toyabe function at different LF. From bottom to top: 0, 1, 2, 4 and 8 (field is in units of  $\Delta/\gamma$ )

$$\rho(\Delta) = \sqrt{\frac{2}{\pi}} \frac{a}{\Delta^2} e^{-a^2/(2\Delta^2)} \quad (3.13)$$

where  $a/\gamma$  is the averaged characteristic field strength inside the sample. This distribution of  $\Delta$  makes the total magnetic field distribution to have a Lorentzian shape. It has been shown that Lorentzian probability distributions of internal magnetic fields are a good approximation of field distributions found in real magnetically diluted random systems with frozen three dimensional magnetic moments [74] [71]. Then, averaging Equation 3.12 over the distribution 3.13, the following relaxation function is found:

$$G_z(t, a) = \frac{1}{3} + \frac{2}{3}(1 - at)e^{-at/2} \quad (3.14)$$

This equation is known as the Lorentzian Kubo-Toyabe function in ZF. Figure 3.5 shows the effect of applying a LF to the Lorentzian distribution.

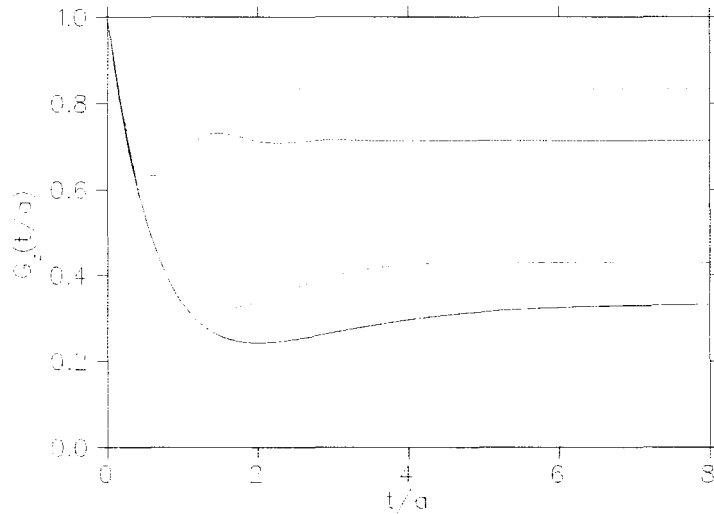


Figure 3.5: Lorentzian Kubo-Toyabe function at different LF. From bottom to top: 0, 1, 2, 4 and 8 (field is in units of  $a/\gamma$ )

Notice that the fast relaxing front of the signal in the Lorentzian case is exponential and also that the minimum in the ZF signal is shallower than in the Gaussian case.

### 3.4.2 Dynamic probabilistic models

One of the most used models for introducing effects of time dependent fields in  $\mu$ SR polarization functions is the “strong collision model” [70] [75]. This is a stochastic model which assumes that after the muon is thermalized, it will see a given field (taken from a given probability distribution) and after  $t_1$  seconds this field will change abruptly to another value (taken from the same probability distribution), then after  $t_2$  seconds it will change again and so on. This process is assumed to be a Markovian process, then the  $t_i$  have a Poisson distribution. This model is physically equivalent to assuming that the time

correlation of the magnetic field at the muon site is  $\langle B(0)B(t) \rangle \propto \exp(-\nu t)$  ( $1/\nu$  is the correlation time).

This model has no general analytic solution so the data fit to the functions that this model generates is done using numerical tables for intermediate values of  $\nu$  and analytic continuations for high fluctuation rates. In Figure 3.6 we show some  $\mu$ SR signals from Gaussian distributions in ZF and at different fluctuation rates. These signals were calculated using a stochastic algorithm. It can be observed that at low fluctuation rates, the effect of having a dynamic magnetic environment is to relax the 1/3 tail of the Kubo-Toyabe function to zero. Then, as the fluctuation rate is increased, the signal relaxes faster and faster until the fluctuation rate is approximately  $\Delta$ . After this,  $G_z$  starts relaxing slower and slower. This effect is due to the fact that the fluctuation rate at the muon site is changing faster than the muons can precess and, therefore, they depolarize much slower. The limit of fast fluctuation rate is called the “narrowing limit” and in this limit the muon polarization function in the Gaussian case is given by [70]:

$$G_z(t, \Delta, B_{\text{LF}}, \nu) = \exp\left(-\frac{2\Delta^2\nu t}{\gamma^2 B_{\text{LF}}^2 + \nu^2}\right) \quad (3.15)$$

where  $B_{\text{LF}}$  is the externally applied LF.

Equation 3.15 is plotted in Figure 3.7 for different values of LF. It is interesting to note in this figure how harder it is to decouple fluctuating magnetic fields than static ones (compare Figure 3.7 with Figure 3.4). Take for instance the signal in zero field in this figure, it is an exponential function with a characteristic time constant of  $10/2 = 5$ . If this  $\mu$ SR signal was produced by a

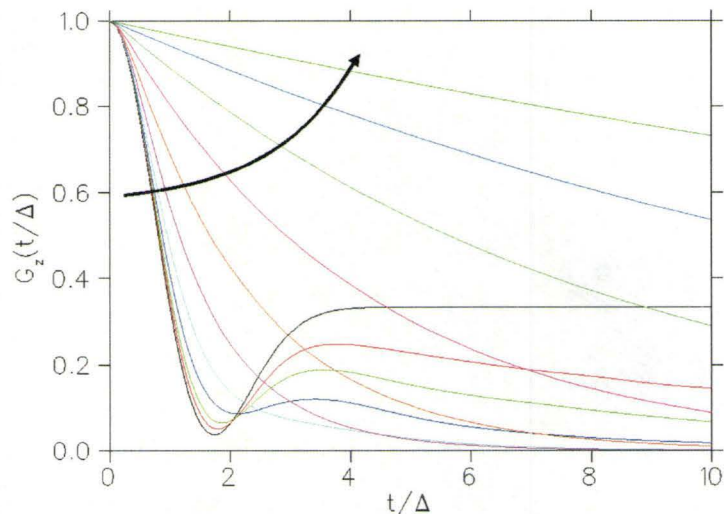


Figure 3.6: Gaussian Kubo-Toyabe functions in ZF at different fluctuation rates ( $\nu$ ). Fluctuation rate grows in the direction of the arrow: 0 (black), 0.125 (red), 0.25 (electric green), 0.5 (dark blue), 1 (aqua), 2 (magenta), 4 (brown), 8 (rich magenta), 16 (light green), 32 (light blue) and 64 (green). The fluctuation rate is in units of  $\Delta$ .

static magnetic environment lets say, we would expect the muon polarization function to be decoupled in a LF much bigger than  $1/5 = 0.25$ , so around 2.5 lets say (ten times bigger). Instead, Figure 3.7 shows that it takes a field of about 64 (160 times bigger) to decouple the signal, since the magnetic field at the muon site is dynamic. We would like to note that fluctuating magnetic fields are always harder to decouple than static ones, even if the fluctuation rate is low (in which case Equation 3.15 is not valid). LF measurements are very useful to determine if a magnetic environment is static (flat and almost decoupled signal at high fields) or dynamic (relaxation of the signal to zero even at high fields).

The muon polarization function in the slow fluctuating limit is given by [70]:

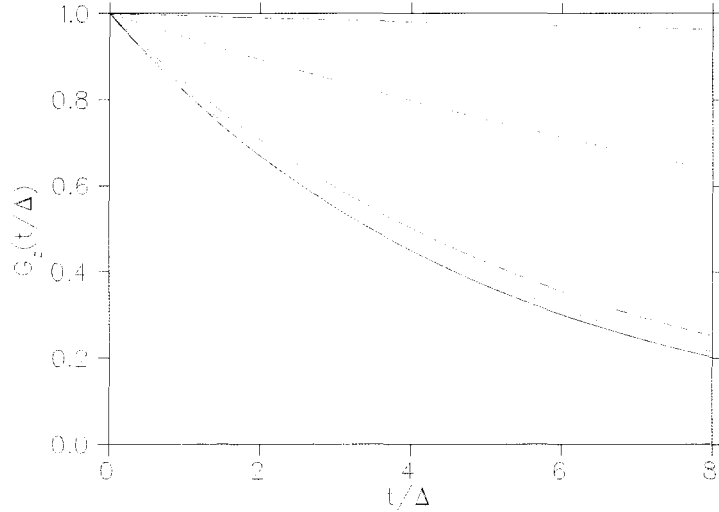


Figure 3.7: Gaussian Kubo-Toyabe functions in the narrowing limit (Equation 3.15) for  $\nu/\Delta = 10$  and at several LF (in units of  $\gamma B/\Delta$ ). From bottom to top: 0 (black), 2 (red), 4 (blue), 8 (green), 16 (magenta), 32 (aqua) and 64 (red again).

$$G_z(t) = \frac{1}{3}e^{-\frac{2\nu t}{3}} \quad (3.16)$$

for  $t \gg 1/\Delta$ . Note from this equation that, as mentioned before, the effect of slow dynamic fields is to relax to zero the  $1/3$  persistent polarization.

Using the expression for the strong collision model (which is an infinite sum of integrals [70]) and assuming a small fluctuation rate (compared to  $\Delta$ ), we have derived the following expression which generalizes Equation 3.16 to include all the time and LF axes:

$$G_z(t, \Delta, B_{\text{LF}}, \nu) = e^{-\nu t} \left( G_z^0(t, \Delta, B_{\text{LF}}) + T_B (e^{\nu T_B t} - 1) \right) \quad (3.17)$$

where  $G_z^0$  is the static Gaussian Kubo-Toyabe equation and  $T_B$  is defined to be the value of  $G_z^0(\infty, \Delta, B_{LF})$ . Note that this equation is general for a given field distribution and at long times it can be reduced to:

$$G_z(t, T, \nu) \approx T_B e^{-(1-T_B)\nu t} \quad (3.18)$$

which is the generalization of Equation 3.16 for arbitrary LF. Equation 3.17 is valid for  $\nu \ll (3\Delta^2 + \gamma^2 B_{LF}^2)^{1/2}$ ; then this equation works for higher and higher fluctuation rates as the LF is increased. This can be seen if the high LF limit of Equation 3.17 is taken and the Gaussian value of  $T_B$  (in the same high LF limit) is used:

$$\begin{aligned} G_z(t, \Delta, B_{LF}, \nu) &= T_B \exp(-(1-T_B)\nu t) \\ &= \left(1 - \frac{2\Delta^2}{\gamma^2 B_{LF}^2}\right) \exp\left(-\frac{2\Delta^2 \nu t}{\gamma^2 B_{LF}^2}\right) \end{aligned} \quad (3.19)$$

this equation, which is valid for  $t \gg (\gamma B_{LF})^{-1}$ , has the same exponent as the high LF limit ( $\nu \ll \gamma B_{LF}$ ) of Equation 3.15 which is valid at high fluctuation rates.

For intermediate fields it is convenient to have an expression for  $T_B$  to use in Equations 3.17 and 3.18. There is no analytic solution for the Gaussian case. Nevertheless, for spherically symmetric magnetic field distributions  $T_B$  can be approximated by [76]:

$$T_B = \frac{\frac{1}{3} \left( \frac{2\Delta}{\gamma} \right)^2 + B^2}{\left( \frac{2\Delta}{\gamma} \right)^2 + B^2} \quad (3.20)$$

where  $\Delta$  is the standard deviation of the magnetic field distribution.

The behavior of the muon polarization as a function of fluctuation rate can be seen in Figure 3.8 for the case of a magnetic environment with a Lorentzian field distribution\*\*. This picture shows that at low fluctuation rates the signal relaxes with the characteristic exponential behavior of the Lorentzian case, while the long time remnant polarization relaxes faster and faster as  $\nu$  is increased. In the Lorentzian case there is also a narrowing limit ( $\nu \gg a$ ) but now, the analytic solution is a power exponential with a coefficient of 1/2:

$$G_z(t, a, B_{LF}, \nu) = \exp \left( \frac{4a^2 \nu t}{\gamma^2 B_{LF}^2 + \nu^2} \right)^{1/2} \quad (3.21)$$

### 3.4.3 Stretched probability distributions

In systems with magnetic anisotropy (like Ising systems)  $P(\vec{B})$  can differ from the spherically symmetric cases discussed in Sections 3.4.1 and 3.4.2. The first approximation to model muon polarization functions arising from magnetically anisotropic systems is to allow for the magnetic field distribution to be stretched or compressed along a symmetry axis [77]. Of particular interest to our measurements is the case in which the initial muon spin direction is

---

\*\* Note that when dealing with the Lorentzian case care should be taken in performing the calculation in a physical way, that is, applying the strong collision model before performing the average over the distribution of  $\Delta$  shown in Equation 3.13 [73].

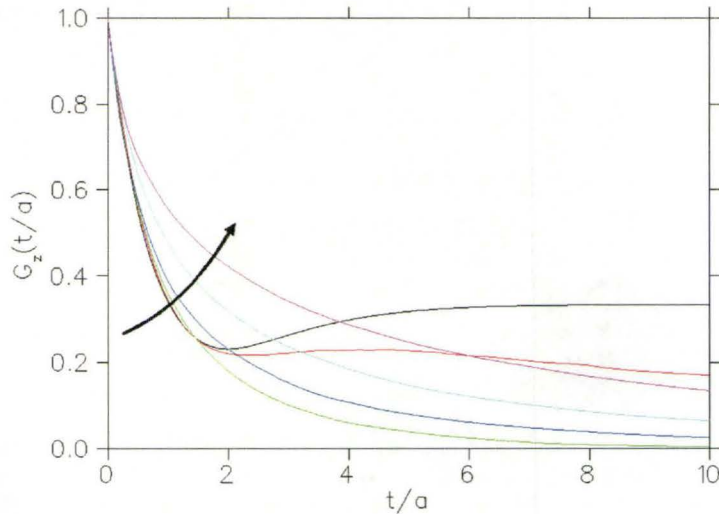


Figure 3.8: Dynamical Lorentzian Kubo-Toyabe function in ZF at different fluctuation rates ( $\nu$ ). Fluctuation rate grows in the direction of the arrow: 0 (black), 0.1 (red), 1 (electric green), 2.5 (dark blue), 5 (aqua), and 10 (magenta). The fluctuation rate is in units of  $a$ .

perpendicular to this axis, so we will deal with this particular case through most of this section.

Figure 3.9 shows three muon polarization signals in ZF arising from the following field distribution (assuming the initial muon spin direction along  $z$ ):

$$P(\vec{B}) = \left( \frac{\gamma}{\sqrt{2\pi}\Delta_x} \right) \left( \frac{\gamma}{\sqrt{2\pi}\Delta_{yz}} \right)^2 \exp \left( -\frac{\gamma^2 B_x^2}{2\Delta_x^2} - \frac{\gamma^2 B_y^2}{2\Delta_{yz}^2} - \frac{\gamma^2 B_z^2}{2\Delta_{yz}^2} \right) \quad (3.22)$$

the signals correspond to the cases where the distribution is compressed along  $x$ , spherical and stretched along  $x$ . The polarization functions in this figure were obtained by numerical integrating Equation 3.10.

Figure 3.9 shows that the distortion of the field distribution along an axis affects the muon polarization signal in two ways. The first one is the change of

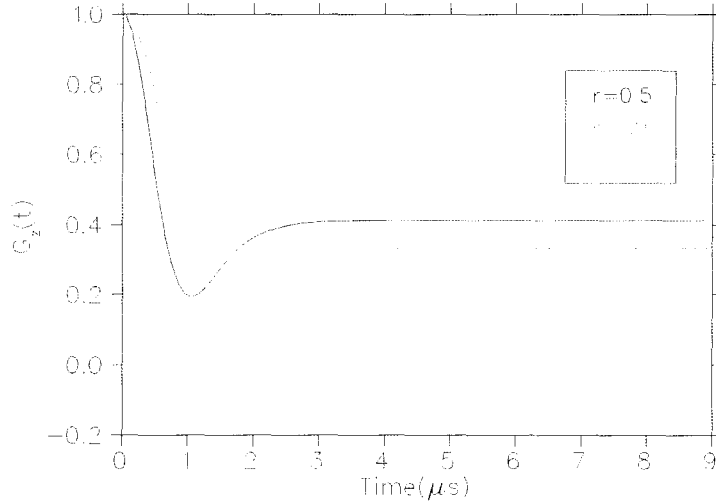


Figure 3.9: Muon polarization functions in ZF from stretched probability distributions. The field distributions are given by equation 3.22 with  $\Delta_x = 1(\mu\text{s})^{-1}$  and  $r = \Delta_x/\Delta_{yz}$ .

depth of the minimum in  $G_z$  [77]; and the second is a shift from  $1/3$  of the long time persistent polarization. Should be noted that the change of position in the minimum of the signals in Figure 3.9 is due to a change in the average size of the internal field and not due to the deformation of the field distribution.

Figure 3.10 shows a plot of the long time persisting polarization as a function of  $r$  (the ratio of the standard deviations of  $P(\vec{B})$  along  $x$  to that along  $yz$ ). Notice that in the  $r = 0$  limit (the field distribution is a plate with the initial muon spin in plane) the persisting tail equals  $1/2$ ; and that for  $r = \infty$  (a one dimensional field distribution perpendicular to the muon spin direction) the persistent polarization is zero.

This last case of an infinitely stretched distribution perpendicular to the initial muon direction, is interesting since this type of distribution would produce a muon polarization signal with no remnant polarization at long times even

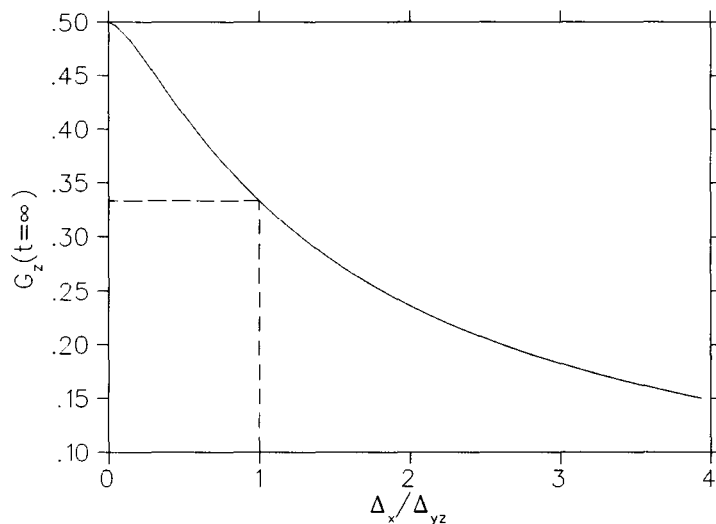


Figure 3.10: Long time persistent polarization as a function of  $\Delta_x/\Delta_{yz}$  obtained from numerical integration. Notice the expected value of  $1/3$  for the spherically symmetric case ( $\Delta_x/\Delta_{yz} = 1$ ).

if the magnetic environment at the muon site is static. This situation could be relevant for  $\text{LiHo}_x\text{Y}_{1-x}\text{F}_4$  (see Chapter 5), and therefore we will discuss it further. The field distribution for this case can be written mathematically as:

$$P(\vec{B}) = \frac{\gamma}{\sqrt{2\pi}\Delta} \delta(B_z - B_{\text{LF}}) \delta(B_y) \exp\left(-\frac{\gamma^2 B_x^2}{2\Delta^2}\right) \quad (3.23)$$

where  $B_{\text{LF}}$  is the externally applied LF. In order to get an expression for the muon polarization function this probability distribution has to be input in Equation 3.10. We will be most interested in the Lorentzian case for analyzing the signals from our most diluted samples; then, this Gaussian signal has to be averaged over the  $\Delta$  distribution in Equation 3.13. We have calculated this ZF polarization function and it is simply given by:

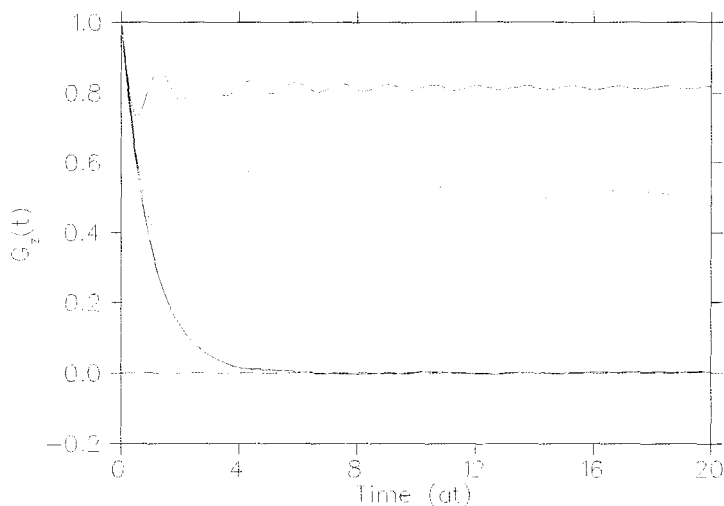


Figure 3.11: Muon spin polarization function for a one dimensional Lorentzian field distribution perpendicular to the initial muon spin direction for different LF in units of  $a$ . From bottom to top:  $B_{\text{LF}} = 0, 0.2, 1, 2, 4$  and  $8$ .

$$G_z(t) = e^{-at} \quad (3.24)$$

where  $a$  is the characteristic field strength defined in Equation 3.13. When a LF is present we calculated the polarization function integrating Equation 3.10 numerically. Figure 3.11 shows  $G_z$  for different LF. The oscillations in  $G_z$  are due to the muon ensemble oscillating at the Larmor frequency set by the external LF (which dominates the internal field contribution at fields bigger than 1). We have analytically calculated the size of the persistent polarization at long times and it is given by:

$$G_z(t = \infty) = \frac{\gamma B_{\text{LF}}}{\gamma B_{\text{LF}} + a} \quad (3.25)$$

This equation shows that the decoupling of the tail is linear in field at low fields. This is a general characteristic behavior of very stretched field distributions and it could be used to distinguish spherical like field distributions from stretched ones.

Field fluctuations can be introduced in this picture using the strong collision model. The polarization signal does not have a general analytic solution again, the muon polarization function for an arbitrary  $\nu$  has to be calculated numerically. We have done this in Figure 3.12 which shows several of these functions in ZF and at different fluctuation rates. Note that slow fluctuations have no effect over the ZF signal since slow fluctuations affect the long time polarization which in this case is zero; LF is needed to study slow fluctuations. The decrease in the relaxation of  $G_z$  as  $\nu$  increases is due to the narrowing effect mentioned previously.

As will be discussed in Chapter 5, we analyzed part of our data using these one dimensional Lorentzian Kubo-Toyabe functions. For doing that we simulated several polarization functions using a Monte Carlo algorithm and constructed an unformatted numerical table with the appropriate structure to be used in the “msrfit” program.

The  $\mu$ SR spectra arising from the opposite case, that of a completely flat field distribution with the initial muon spin direction in plane, are shown in Figure 3.13 for the case of ZF and at several fluctuation rates. These signals were simulated with a Monte Carlo algorithm. It can be seen that for  $\nu=0$  the remaining polarization is 0.5 as expected from Figure 3.10. One characteristic feature of this distribution with respect to the (spherical) Lorentzian Kubo-

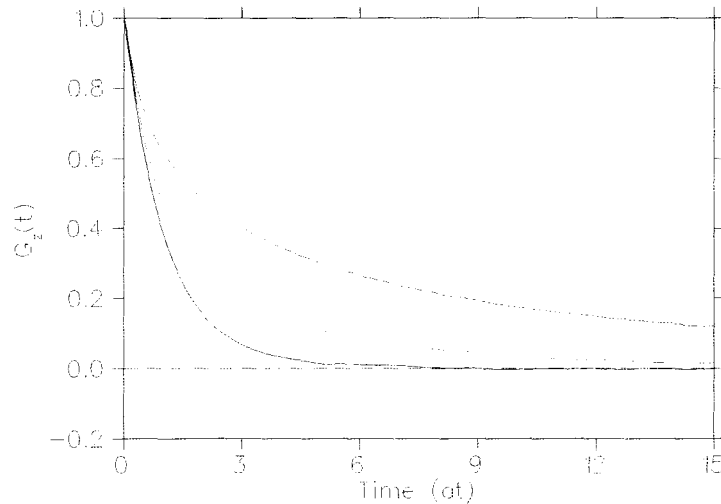


Figure 3.12: Muon spin polarization function for a one dimensional Lorentzian field distribution perpendicular to the initial muon spin direction at different fluctuation rates (in units of  $a$ ) and ZF. From bottom to top:  $\nu=0, 10, 20, 40$  and  $80$ .

Toyabe function is the shallower dip of  $G_z$  (approximately half) for  $\nu=0$ . We also would like to note the big effect that low fluctuation rates of the internal field have on the shape of  $G_z$ , in contrast to the one dimensional case. This last fact, which can be used to distinguish the two different magnetic scenarios, exemplify the significant effect that the shape of the field distribution can have on the response of the  $\mu$ SR signal to dynamic fields.

Now, we will present a method that we developed which can be used to experimentally measure  $r = \Delta_x/\Delta_{yz}$  (this is, how stretched or compressed the field distribution is at the muon site inside the sample). This method assumes that we are probing the system in the narrowing limit ( $\nu \gg \Delta$ ) and it is based on the theory presented in Reference [77]. In fact, our method is similar to the one proposed in that work but it is easier to implement and it is good

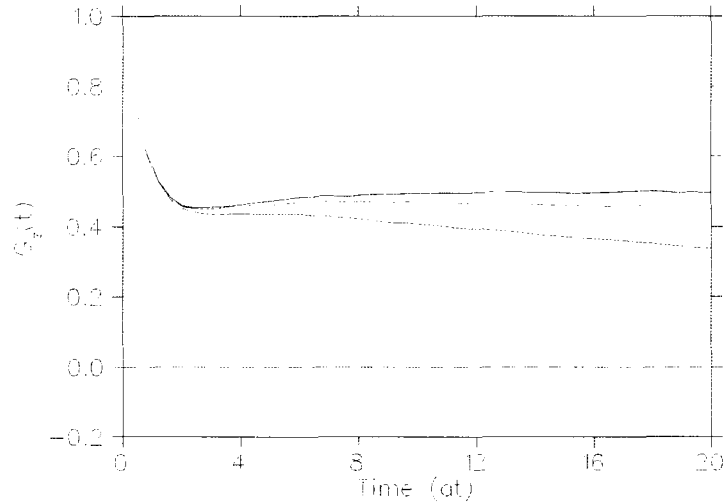


Figure 3.13: Muon spin polarization function for a two dimensional Lorentzian field distribution with the initial muon spin direction in plane and for different fluctuation rates (in units of  $a$ ) and ZF. From top to bottom:  $\nu= 0, 0.01, 0.02, 0.04, 0.08$  and  $0.16$ .

for systems where dynamic magnetism is present, which is the most common case.

The early time behavior of the static Gaussian Kubo-Toyabe in ZF can be expressed in a Taylor series as:

$$G_z(t) \approx 1 - (\Delta t)^2 \tag{3.26}$$

If the muon is in an anisotropic Gaussian environment, the early time relaxation is different depending if the experiment is performed with the initial muon spin parallel to the anisotropy axis ( $G_x$ ) or perpendicular to it ( $G_z$ ). It can be shown that the early time relaxation for these two cases is given by [77]:

$$G_x(t) \approx 1 - (\Delta_{yz}t)^2 \quad (3.27)$$

$$G_z(t) \approx 1 - \frac{\Delta_x^2 + \Delta_{yz}^2}{2} t^2 \quad (3.28)$$

We now let the anisotropic field at the muon site fluctuate. In order to obtain an analytic expression for  $G_x$  and  $G_z$  in the narrowing limit, one has to note that in this limit, all that matters is the early time behavior of the static function. So comparing Equations 3.27 and 3.28 with 3.26, we can use the narrowing limit of the spherical case (Equation 3.15 with  $B_{LF} = 0$ ) to get:

$$G_x(t, \nu) = \exp\left(-\frac{2\Delta_{yz}^2 t}{\nu}\right) = e^{-\lambda_x t} \quad (3.29)$$

$$G_z(t, \nu) = \exp\left(-\frac{(\Delta_x^2 + \Delta_{yz}^2)t}{\nu}\right) = e^{-\lambda_z t} \quad (3.30)$$

If in a  $\mu$ SR experiment one takes two measurements at the same high temperature (so the internal field fluctuates fast), and in one of them the muon spin is parallel to the anisotropy axis while in the other the muon spin is perpendicular, one can fit the data to two exponential functions and get their relaxation rates:  $\lambda_x$  and  $\lambda_z$ . Then the value of  $r$ , which is a measure of how stretched/compressed is your distribution function, can be calculated from these relaxation rates by evaluating:

$$r = \frac{\Delta_x}{\Delta_{yz}} = \sqrt{\frac{2\lambda_{yz}}{\lambda_x} - 1} \quad (3.31)$$

### 3.4.4 The F- $\mu$ -F bond

When ZF  $\mu$ SR experiments are performed on insulating materials which contain fluorine, it is not surprising to observe the characteristic signal from the formation of an F- $\mu$ -F bond [78] [79]. In these materials the positive muon, after thermalizing inside the sample, finds a minimum of potential between the negatively charged F<sup>-</sup> ions. If the magnetic field at the muon site is dominated by the nuclear dipolar field from the two closest fluorine ions (<sup>19</sup>F is a stable isotope with angular momentum of 1/2 and a magnetic moment of  $2.628868\mu_n$ ), the fluorine nuclei and muon will precess in each others magnetic field. Figure 3.14 shows an example of the  $\mu$ SR signal characteristic of the formation of an F- $\mu$ -F bond.

If one assumes that the fluorine nuclear spins are unpolarized upon the arrival of the muon, and that there are three muon sites in the unit cell (one where the initial muon spin points along the bond direction and two where it is perpendicular), the ZF  $\mu$ SR signal is given by:

$$G_z(t) = Ae^{-(\lambda_1 t)^{\beta_1}} G_{F\mu F}^C(t, \omega) + (1 - A)e^{-(\lambda_2 t)^{\beta_2}} \quad (3.32)$$

where  $G_{F\mu F}^C$  is the contribution to the signal from the F- $\mu$ -F bond formation in the above mentioned (cubic) environment and, assuming that the F ions interact only with the muon and not between them, is given by [78]:

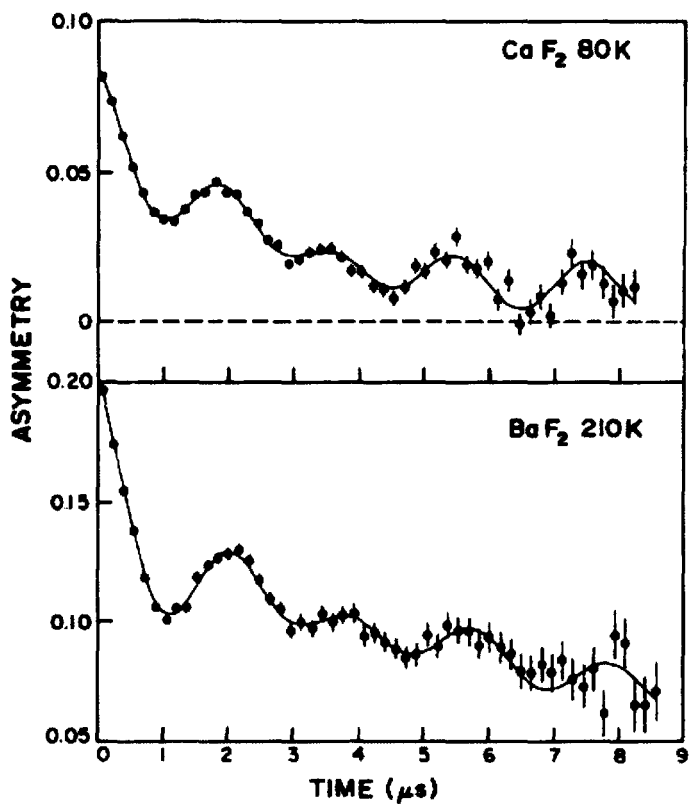


Figure 3.14: Characteristic signal from the formation of an F- $\mu$ -F bond in CaF<sub>2</sub> and BaF<sub>2</sub> in ZF and with the initial muon spin direction along (100). Taken from J. H. Brewer *et al.* [78].

$$G_{F\mu F}^C(t, \omega) = \frac{1}{6} \left[ 3 + \cos(\sqrt{3}\omega t) + \left(1 - \frac{1}{\sqrt{3}}\right) \cos\left(\frac{3 - \sqrt{3}}{2}\omega t\right) + \left(1 + \frac{1}{\sqrt{3}}\right) \cos\left(\frac{3 + \sqrt{3}}{2}\omega t\right) \right] \quad (3.33)$$

The first power-exponential term in Equation 3.32 is a way to introduce phenomenologically the relaxation of  $G_{F\mu F}^C$  by the magnetic field environment around the bond [79]; or to describe, also phenomenologically, muon diffusion (a more useful way to analyze muon diffusion data from materials with F- $\mu$ -F formation is to treat it within the strong collision model [80]). The second power-exponential term represents a fraction of spins which does not participate in the F- $\mu$ -F formation and which remains paramagnetic. The nature of this fraction, which is present in almost every system with F- $\mu$ -F formation, is believed to be due to the formation of muonium but its precise origin is not known [79].

The fitting parameter  $\omega$  in Equation 3.32 gives information about the strength of the magnetic interaction between the muon magnetic moment and those of the fluorine nuclei. As mentioned earlier, this interaction is dipolar, therefore  $\omega$  is given by:

$$\omega = \frac{\mu_0 \hbar \gamma_\mu \gamma_{^{19}\text{F}}}{2\pi r^3} \quad (3.34)$$

here  $\gamma_\mu$  and  $\gamma_{^{19}\text{F}}$  are the muon and fluorine-nuclear gyromagnetic ratios and  $r$  is the distance from the muon position to a fluorine nucleus. It has been noticed that in ionic insulators,  $r$  is always very close to the ionic radius of

$F^-$  ( $\approx 1.16\text{\AA}$ ) so in most cases the muon is able to distort the position of the fluorine ions by pulling them together. This means that the bond can be visualized as two hard balls barely touching each other and with a positive muon just between them. This is the picture for the hydrogen bonding of two  $F^-$  ions, hence the name F- $\mu$ -F bond [78]. The fact that the muon can behave similarly to hydrogen makes  $\mu$ SR a powerful probe to study hydrogen dynamics in matter [81] [66]. We note that F- $\mu$ -F bonding has been observed not only in ionic insulators, but also in materials where the fluorines are covalently bonded [82].

Equation 3.32 is commonly used to analyze data from systems which present F- $\mu$ -F formation. Nevertheless, the use of this equation should be restricted to situations where the sample is in the form of a powder and/or the bonds have cubic symmetry. In general, the F- $\mu$ -F signal for a given bond depends on the angle  $\theta$  formed between the initial muon spin direction and the bond direction. Using an exact numerical diagonalization of the density matrix for the single bond problem, we obtained for the first time numerical expressions for the amplitudes of the different Bohr-frequency terms in the muon polarization signal as a function of  $\theta$ . Then, we fitted this numerical results to analytical formulas (which describe exactly the dependence of the coefficients with  $\theta$ ), and checked that our results could reproduce the cubic case shown in Equation 3.33. We found that the muon polarization function for a single F- $\mu$ -F bond is given by:

$$\begin{aligned}
 G_{F\mu F}(t, \omega, \theta) = & A_1(\theta) + A_2(\theta) \cos(\sqrt{3}\omega t) + A_3(\theta) \cos\left(\frac{3 - \sqrt{3}}{2}\omega t\right) \\
 & + A_4(\theta) \cos\left(\frac{3 + \sqrt{3}}{2}\omega t\right)
 \end{aligned} \tag{3.35}$$

where the  $A_i$  coefficients are given by:

$$A_1(\theta) = \frac{13}{24} + \frac{1}{8} \cos(2\theta) \tag{3.36}$$

$$A_2(\theta) = \frac{5}{24} + \frac{1}{8} \cos(2\theta) \tag{3.37}$$

$$A_3(\theta) = \frac{1}{8} \left(1 - \frac{1}{\sqrt{3}}\right) (1 - \cos(2\theta)) \tag{3.38}$$

$$A_4(\theta) = \frac{1}{8} \left(1 + \frac{1}{\sqrt{3}}\right) (1 - \cos(2\theta)) \tag{3.39}$$

Figure 3.15, shows how  $G_{F\mu F}$  behaves, as a function of time and  $\theta$ . Then, the following general equation should be used to fit  $\mu$ SR data from a system where the bonds are not in a cubic arrangement:

$$G_z(t) = \frac{1}{N} e^{-(\lambda t)^\beta} \sum_{i=1}^N G_{F\mu F}(t, \omega, \theta_i) \tag{3.40}$$

where the summation should be carried over all the F- $\mu$ -F bonds inside the unit cell, and the power exponential factor is introduced to account phenomenologically for the relaxation of the signal (see Figure 3.14) [78].

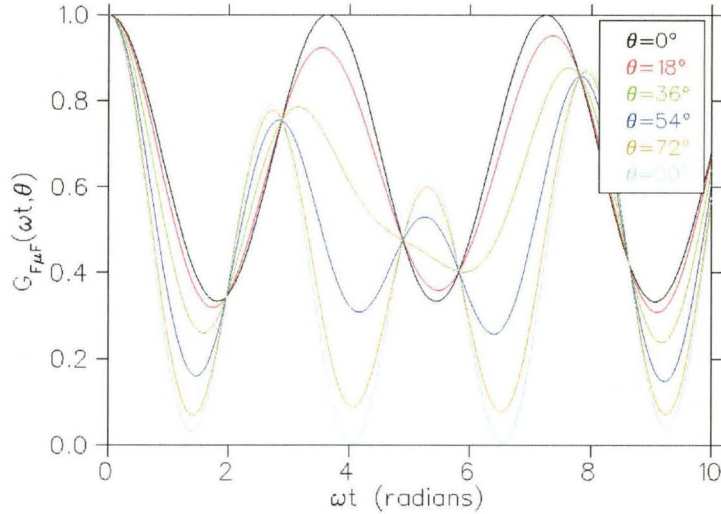


Figure 3.15: Muon polarization function as a function of time from a single F- $\mu$ -F bond that makes an angle  $\theta$  with the initial muon spin direction.

### 3.4.5 The $\mu$ SR signal from a ferromagnet

The muon spin polarization function produced by an ideal ferromagnet is given by (see Equation 3.2):

$$G_z(t) = \sum_i \left( \cos^2(\theta_i) + \sin^2(\theta_i) \cos(\gamma |\vec{B}_i| t) \right) \quad (3.41)$$

where  $\vec{B}_i$  is the local magnetic field at the muon site (proportional to the magnetization), and the summation is carried over all the magnetically inequivalent muon sites inside the crystallographic unit cell. This equation shows that an spontaneous precession of the  $\mu$ SR signal in ZF is a feature of a ferromagnetic state (and almost any magnetically ordered long range state). We note that for a ferromagnet all the terms in Equation 3.9 will contribute to the total field (except for  $\vec{B}_{\text{dia}}$ ); but if the system splits into domains, such that the total

magnetization is zero, then is possible that the demagnetizing term ( $\vec{B}_{\text{dem}}$ ) does not contribute towards the total field [64].

Real ferromagnets generally break up into magnetic domains. As a result, muons which land near the magnetic domain wall see a wide range of magnetic fields. These muons will precess with different Larmor frequencies and depolarize the time dependent part of  $G_z$ . In order to account for this effect (and for disorder)  $\mu\text{SR}$  spectra from ferromagnets are fitted to:

$$G_z(t) = \sum_i A_i e^{-(\lambda_i t)^\beta} \cos(\omega_i t) + B \quad (3.42)$$

where the summation is carried over all the magnetically inequivalent muon sites. We note that it is common to find ferromagnets where the  $\lambda_i$  are so big that no precession rate is observed [64].

Dynamic fields (caused by dynamic moments or by muon diffusion) can cause further depolarization of  $G_z$  so a relaxing term is usually multiplied to the  $B$  constant in Equation 3.42 to account for slow dynamic fields.

## Chapter 4

# $\mu$ SR studies of the $x=1$ and $0.45$ systems

In this chapter we present an overview of the sample preparation procedure, followed by a section where we present the high temperature data ( $T > 20\text{K}$ ) where we observe F- $\mu$ -F bond formation. After that, the following two sections present the analysis of our data on the  $x=1$  and  $x=0.45$  ferromagnetic compounds; and in the last section we make some comments on the outcome of the analysis.

### 4.1 Sample preparation

As mentioned in Chapter 2,  $\text{LiHo}_x\text{Y}_{1-x}\text{F}_4$  is used by the laser industry as a resonant cavity medium; therefore, high quality single crystals are commercially available. We purchased our crystals from “Tydex J.S. Co.” with the following stoichiometries:  $x=1$ ,  $0.45$ ,  $0.25$ ,  $0.12$ ,  $0.08$ ,  $0.045$  and  $0.02$  (see Figure 4.1). It was found later that the Ho concentration of the  $x=0.02$  system was actually equal to  $0.018$  [37].

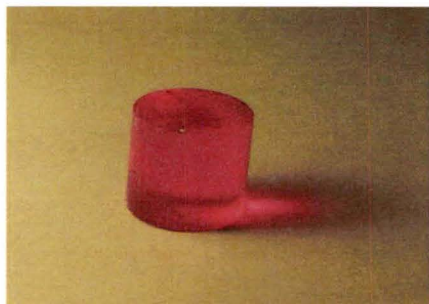


Figure 4.1: Crystal of  $\text{LiHo}_x\text{Y}_{1-x}\text{F}_4$

The crystals were cylindrically shaped with a diameter of 8mm and a length of 1cm. The axis of the cylinders was approximately  $5^\circ$  off from the crystallographic [310] direction. We aligned the crystals along this direction using an X-ray Laue diffractometer at the “Brockhouse Institute for Materials Research” (McMaster University, Canada). For this purpose, the samples were mounted on a goniometer and a Laue pattern was registered in a back scattering geometry onto a photographic film. The good quality of the crystal was confirmed by the clear and well resolved diffraction patterns (see Figure 4.2). The photographic film was digitized using a transmission scanner and the pattern was analyzed with “OrientExpress” software [83] which outputs the rotation angles necessary for aligning the desired crystallographic direction along the x-ray beam direction. Three Laue images were typically taken for each crystal; one for rough alignment, another for fine tuning, and a third one to check the final position.

After alignment the samples were carefully transferred from the goniometer onto a glass sample holder for cutting. This was done by mounting the glass sample holder and the goniometer in a straight rail in such a way that the sample was positioned just in front of the glass holder. After this, epoxy resin

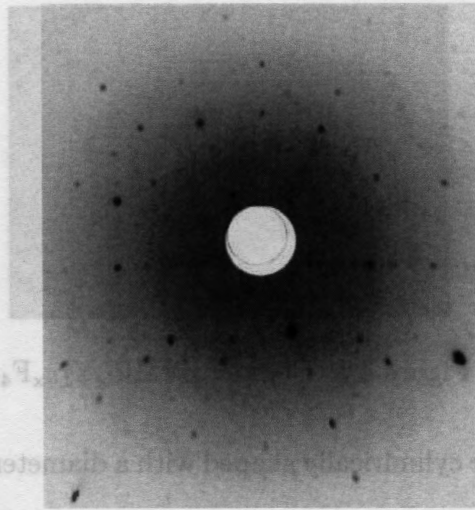


Figure 4.2: Characteristic Laue pattern from  $\text{LiHo}_x\text{Y}_{1-x}\text{F}_4$ . Central spot is [310].

was used to fill the gap between the glass holder and the sample. Once the resin dried the sample could be safely removed from the goniometer. The crystals were cut using a high speed diamond saw. Three disks of 0.6mm thickness were sliced from the main crystals with the [310] crystallographic direction perpendicular to the flat face of the plate (to have the  $\hat{c}$  axis in the plane of the disk). These plates were further cut in a way that they could form a compact array when placed in the  $\mu\text{SR}$  sample holder. Finally, the epoxy was removed from the sample by letting it rest for 24 hours under dichloromethanol.

For the Zero Field (ZF) and Longitudinal Field (LF) measurements the muons were implanted with their spin parallel to the [310] crystallographic direction and, therefore, perpendicular to  $\hat{c}$ , the Ising direction (see figure 4.3). The TF measurements were performed in the spin rotated mode. In this mode the external magnetic field is kept fixed along the beam direction but

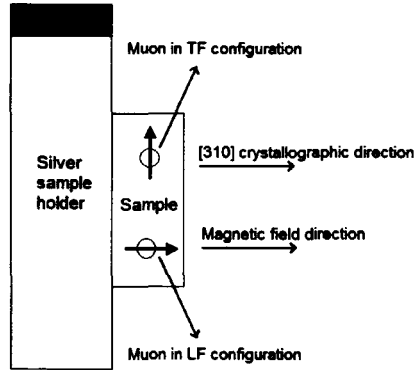


Figure 4.3: Diagram for the experimental setup used in  $\text{LiHo}_x\text{Y}_{1-x}\text{F}_4$ . Muons in the LF (and ZF) configuration were implanted with the initial spin direction along the crystallographic  $[310]$  direction, while those in the TF configuration were perpendicular to it.

the muon spin is rotated such that it is perpendicular to it and, therefore, perpendicular to  $[310]$  (see figure 4.3).

## 4.2 F- $\mu$ -F in $\text{LiHo}_x\text{Y}_{1-x}\text{F}_4$

As observed in many fluorine systems, muons in  $\text{LiHo}_x\text{Y}_{1-x}\text{F}_4$  produce a characteristic signal from the formation of an F- $\mu$ -F bond (see Figure 4.4). We observed this type of signal at high temperatures ( $T \gtrsim 20\text{K}$ ) and (nominal) ZF regardless of the doping value.

In order to fit the F- $\mu$ -F signals, we assumed that the muon site inside the crystal is half way between nearest neighbor fluorines, as is the case in many other fluorine systems [84]. Using this position together with the known initial

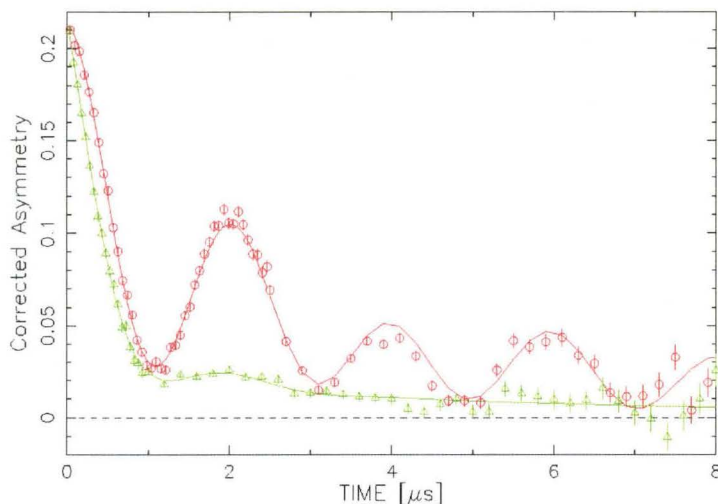


Figure 4.4: F- $\mu$ -F signal from LiHoF<sub>4</sub> at 200K (red circles) and 20K (green triangles). The initial muon spin direction is along (001).

muon spin direction\*, we computed the angles in Equation 3.40 and used this equation to fit our data. We also assumed further that  $\beta$  in this equation was equal to 1 (exponential relaxation of the F- $\mu$ -F signal) in order to reduce the number of free parameters and their uncertainties. We confirmed a posteriori that this assumption did not significantly affect the quality of the fit.

The fitted values of the relaxation rate of the F- $\mu$ -F signal ( $\lambda$ ) are shown in Figure 4.5. It can be seen that for temperatures above  $\approx 50$ K the relaxation rate is independent of doping level and converges to a high temperature value. This doping independent value at high temperature indicates that the Ho ions are fluctuating too fast and that the depolarization of the muon ensemble is dominated by interactions with nuclear moments of the fluorine ions. Below

---

\* Only in the high temperature measurements (taken in the helium flow cryostat) of the x=1 system the initial muon spin direction was [001] and angle of the F- $\mu$ -F bond was calculated accordingly.

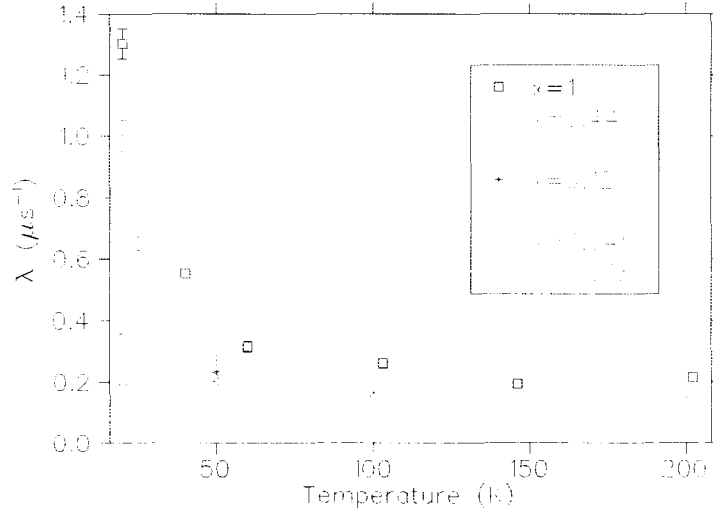


Figure 4.5: Relaxation rate of the F- $\mu$ -F signal ( $\lambda$  in Equation 3.40) as a function of temperature and doping level in ZF. This data was taken in the He flow cryostat at the M20 beam line.

$\approx 50\text{K}$  the relaxation rate of all of our samples increases due to the slowing down of the Ho moments into the  $\mu\text{SR}$  time window [41], as well as to the increase of the thermal average of the Ho magnetic moment (see Figure 5.6 in next chapter). Also note that this relaxation rate is slightly bigger for samples with bigger values of  $x$ . This is due to the fact that the average internal field at the muon site is bigger in samples which are magnetically denser.

Figure 4.6 shows the characteristic frequency of the F- $\mu$ -F bond ( $f_{\text{F}\mu\text{F}}$ ) as a function temperature and doping level. It can be observed that, if the two lowest temperatures for the  $x=1$  system is put aside, there is no significant temperature or doping dependence in this parameter. This is expected, since the average length of the F- $\mu$ -F bond should not be altered by temperature or substitution of Ho by Y. The apparent increase with temperature of the fitted value of  $f_{\text{F}\mu\text{F}}$  is due to a trade off between this parameter and the relaxation

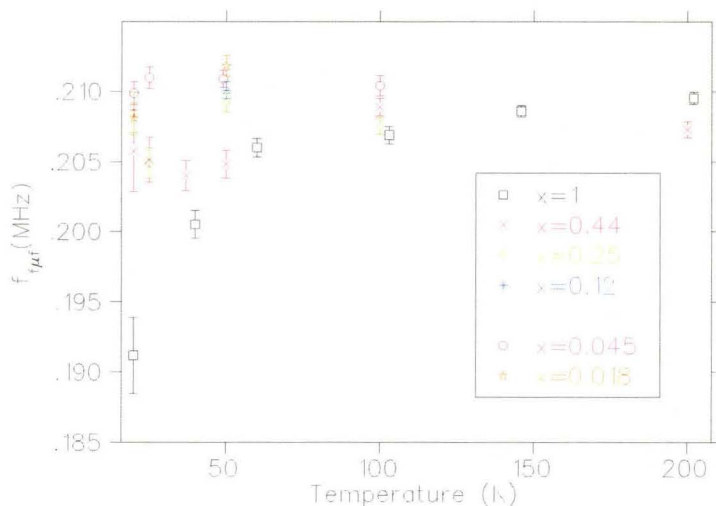


Figure 4.6: Characteristic frequency of the F- $\mu$ -F signal ( $f_{F\mu F}$ ) as a function of temperature and doping level in ZF. This data was taken in the He flow cryostat at the M20 beam line.

rate of the signal. This fact is implied by plot of  $\lambda$  versus  $f_{F\mu F}$  which shows an almost linear relationship between their fitted values. If one leaves in aside the lowest temperature point of the  $x=1$  system, the averaged value of  $f_{F\mu F}$  is  $0.208 \pm 0.003$  MHz (where the uncertainty is the standard deviation of the distribution). This value gives an F- $\mu$ -F bond length of  $1.200 \pm 0.006$  Å. The value of  $f_{F\mu F}$  agrees within error bars with that reported for an  $x=0.002$  sample in the literature [41]. Also, our value of  $f_{F\mu F}$  agrees well with what has been reported for other fluorine systems where it can range from 0.2 MHz (in  $ZnF_2$ ) to 0.226 MHz (in  $CaF_2$ ) [79].

When analyzing the F- $\mu$ -F data we noticed that the fit of some of our systems improved if a small Gaussian background term was added to the fitting function. The presence of a background has already been observed in other fluorine systems [78] [84] but its nature is not yet known. We also observed

that sometimes a background term was also present at low temperature where the signal relaxes so fast that no precession from the F- $\mu$ -F bond formation can be observed. At low temperatures the background contribution could be identified thanks to the fact that we could fully decouple it with a LF of 50G (this decoupling can be seen in Figure 5.1 in the following chapter). If present, the background was always observed to be temperature independent and, therefore, it was easy to account for it by adding a common Gaussian term to the fitting functions. Table 4.1 shows the amplitude and relaxation rate of the background for all the ZF (or low LF) measurements. This table shows that the background term was most common on the low temperature measurements taken in the dilution refrigerator at the M15 beam line. We will further discuss about this fraction in Chapter 5.

### 4.3 LiHoF<sub>4</sub>

Below 20K the relaxation produced by the magnetic environment becomes bigger than  $f_{F\mu F}$  (see Figure 4.4) so the signal is damped faster than it can oscillate. This prevented us from fitting  $f_{F\mu F}$  at low temperatures in any of the samples. As we mentioned before, the increase of the relaxation rate below 20K is due to the slowing down of the paramagnetic Ho ions [41], and to the increase of the averaged magnetic moment size (see Figure 5.6 in the next chapter). The effect of the slowing down of the Ho magnetic moments with temperature can be seen in Figure 4.7. It can be seen in this figure that at 50mK (in the ferromagnetic regime) the signal is partially decoupled due to the externally applied 2T of LF. This indicates that at this temperature

Cryostat	x	% of asymmetry	Relaxation rate ( $\mu s^{-1}$ )
He flow	1	7	0.3
He flow	0.45	0	
He flow	0.25	0	
He flow	0.12	0	
He flow	0.08	6	0.4
He flow	0.045	0	
He flow	0.018	0	
DR	1	10	0.6
DR	0.45	10	0.4
DR	0.25	15	0.3
DR	0.12	20	0.3
DR	0.08	6	0.6
DR	0.045	8	0.6
DR	0.018	0	
DR	0.018	0	

Table 4.1: Background term observed in our ZF (or low LF) measurements. The amplitude of the background is expressed as a percentage of the total amplitude of the signal. DR stands for dilution refrigerator.

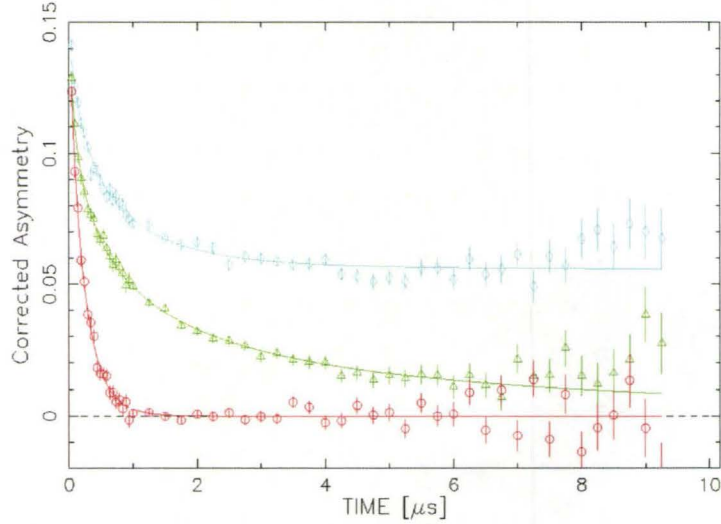


Figure 4.7: Corrected asymmetries for  $\text{LiHoF}_4$  in a LF of 2T at three different temperatures: 10K (red circles), 2K (green triangles) and 50mK (blue diamonds).

the magnetic environment around the muon is static within the  $\mu\text{SR}$  time window (see Section 3.4.2). Then, as the sample is warmed up, the long time tail starts relaxing faster and faster as the fluctuation rate of the magnetic moments increase with temperature and the system is driven paramagnetic. The partial decoupling with a 2T field also indicates that the internal field at the muon site has a characteristic strength of  $\approx 2\text{T}$ , this point will be discussed later in this section (see Figure 4.13).

The low LF data taken at low temperature was fit to the following polarization function:

$$G_z(t) = Ae^{-\lambda_1 t} \cos(2\pi f_{\text{ferro}} t) + (1 - A)e^{-(\lambda_2 t)^2} \quad (4.1)$$

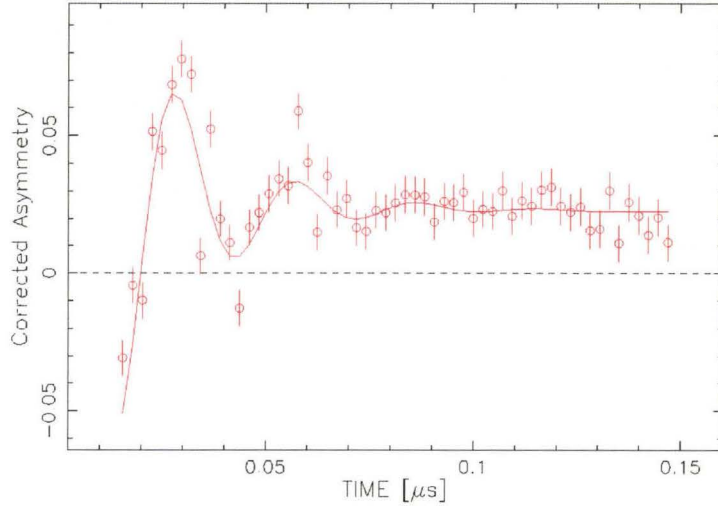


Figure 4.8:  $\mu$ SR signal for  $\text{LiHoF}_4$  measured at 50mK and a LF equal to 20G inside the ferromagnetic state.

where the second term accounts for the background. This fitting function was motivated by the shape of the signal which is shown in Figure 4.8. The precession of the signal below  $T_c$  indicates to us that the average magnitude of the internal field generated by the ferromagnetic state is bigger than the typical width of the distribution. The average magnitude of the internal field is expected to track the magnetic domain magnetization and therefore it should be proportional to the ferromagnetic order parameter. The fits were performed leaving all the parameters in Equation 4.1 free (including the parameter  $\alpha$  in Equation 3.8). It was checked that there was no trade off between parameters.

The temperature dependence of  $f_{\text{ferro}}$  is shown in Figure 4.9. For  $T \geq 1.5\text{K}$ , the fits were performed setting  $f_{\text{ferro}}$  equal to zero. This was done in order to reduce the noise of the other fitted parameters in a region where the relaxation of the signal is faster than the precession frequency and, therefore, the fitting

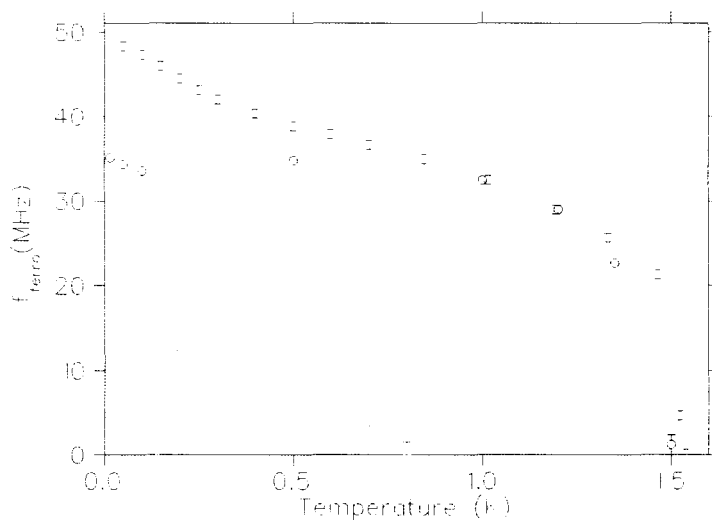


Figure 4.9: Precession frequency of the muon ensemble in ZF in  $x=1$  (black circles, nominal  $T_c=1.53\text{K}$ ) and in  $x=0.45$  (blue diamonds). Note that the highest temperature points (at  $1.5\text{K}$  for  $x=1$  and  $0.8\text{K}$  for  $x=0.45$ ) are not fitted values; they only represent the range of values of  $f_{\text{ferro}}$  which could not be resolved at that temperature due to the fast relaxation of the signal. The green crosses is the ZF ferromagnetic order parameter mapped using optical spectroscopy (taken from Reference [85]). The red circles signal the boundary of the scaled  $H_c(T)$  phase diagram (taken from [24]). The analysis of the  $x=0.45$  system is presented in Section 4.4.

program cannot distinguish the value of  $f_{\text{ferro}}$  from zero. Note that because of this reason, the  $1.5\text{K}$  point is not a fitted value but it represents the the range of values which  $f_{\text{ferro}}$  could take at this temperature without being able to be resolved.

Figure 4.9 shows that the temperature evolution of  $f_{\text{ferro}}$  (black circles) follows that of the system magnetization (mapped using optical spectroscopy [85] and which is shown with green crosses in the figure). This confirms that  $f_{\text{ferro}}$  is proportional to the ferromagnetic order parameter (see section 3.4.5). In our measurements though, we have tracked this order parameter down to

13mK. To our knowledge, this is the first time that the ZF order parameter has been directly measured at temperatures well below the hyperfine energy splitting ( $\approx 200\text{mK}$ ).

In Figure 4.9 we also plotted the order parameter that one would expect from mapping the  $H$ - $T$  phase diagram (obtained with  $\chi_{AC}$  measurements [24]) into magnetization by assuming that the relation  $H(T) \propto M(T)$  holds (the term on the left of the proportionality is the critical transverse field and that on the right is the ferromagnetic order parameter) [86]. The figure shows that this relation, which can be derived from a mean field treatment of the transverse field Ising model (TFIM) [2], does not hold in general in the case of  $\text{LiHoF}_4$ ; and therefore previous calculations based on this assumption should be revised for the low temperature points [23]. The reason why this relationship does not apply in  $\text{LiHoF}_4$  is the presence of the hyperfine interaction in our system (that this is the case can be shown with a mean field solution of the TFIM with hyperfine interactions, see Reference [87]). Since the effect of the hyperfine interaction on the physical behavior of the system is strongest in high external fields (where it prevents fluctuations between the electro-nuclear Ising levels as explained in Section 2.3), then for  $\text{LiHo}_x\text{Y}_{1-x}\text{F}_4$  the relation  $H(T) \propto M(T)$  should be used only when the externally applied field is very low.

Figure 4.10 shows how  $\lambda_1$  increases monotonically with decreasing temperature down to 1.5K. At this point there is an increase at a different rate down to  $\approx 0.5\text{K}$ . This increase coincides with  $T_c$  and it is due to the dynamics of the system moving below the  $\mu\text{SR}$  time window (remember that the system is static at base temperature, see Figure 4.7). This increase can also reflect

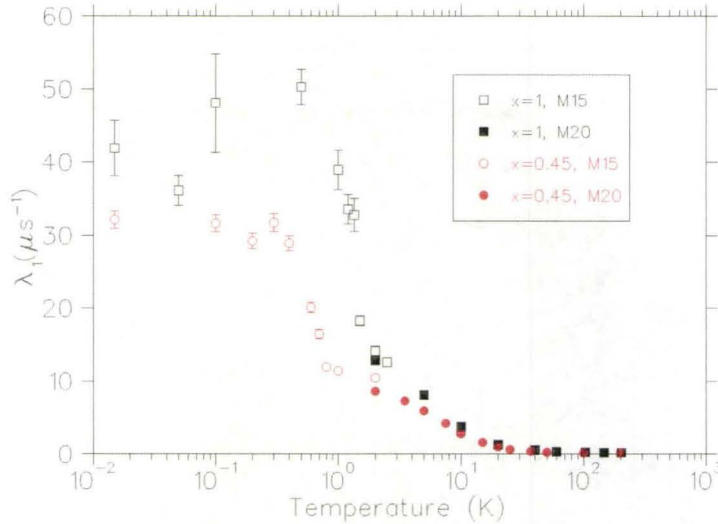


Figure 4.10: Relaxation rate of the non-paramagnetic fraction of the  $\mu\text{SR}$  signal as a function of temperature for  $x=1$  and  $x=0.45$  in in 20G LF. The analysis of the  $x=0.45$  system is presented in Section 4.4.

a broadening of the field distribution caused by the splitting of the system into magnetic domains. The error bars on  $\lambda_1$  are big due to the fact that the signal relaxes very fast and, therefore, the number of muons counted in the first  $0.1\mu\text{s}$  is small.

Figure 4.11 shows the  $\mu\text{SR}$  signals from a LF scan at  $T=50\text{mK}$  (remember that the applied field is always perpendicular to the Ising axis). It can be observed that the signal is being decoupled with field. Again, the decoupling of the signal is due to the presence of static magnetism within the  $\mu\text{SR}$  time window up to 4T (we took measurements at 4.5T and 5T but the signal is completely decoupled at these fields). This observation indicates the absence of low lying magnetic excitations at the muon Zeeman splitting energy (which at 4T is 25mK or  $2.25\mu\text{eV}$ ) and  $T=50\text{mK}$ .

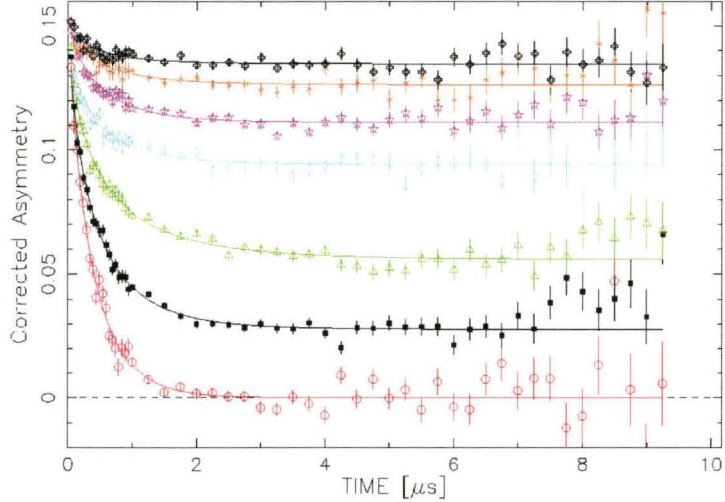


Figure 4.11:  $\mu$ SR signal for the  $x=1$  system as a function of LF at 50mK. 1T(at 10K for reference) - red circles; 1T - black squares; 2T - green triangles; 2.5T - aqua diamonds; 3T - magenta stars; 3.5T - orange X; and 4T - black crosses.

Since the signals in LF showed decoupling with an exponential like front (with no oscillatory term), we fitted them with the following relaxation function:

$$G_z(t) = Ae^{-(\lambda_{LF}t)^{\beta_{LF}}} + (1 - A) \quad (4.2)$$

In the LF runs the parameter  $\alpha$  (see Equation 3.8), which increases with LF, presented some random variations. Nevertheless we were able to set an appropriate value for it by comparing the LF signals at low temperature with other LF runs at the same fields but at 10K where the system is in the paramagnetic state and the signal relaxes to zero. In a preliminary fit with all the parameters free it was noticed that  $\beta_{LF}$  in Equation 4.2 had no dependence on field. Then, this parameter was fixed to 0.7, its average value, and the data

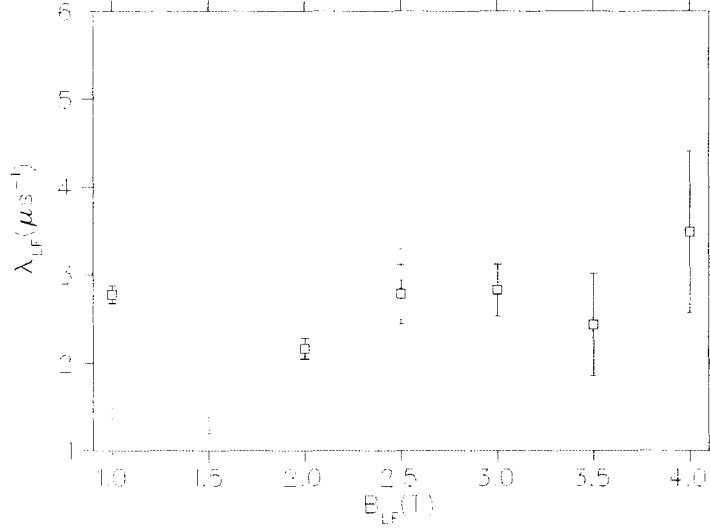


Figure 4.12:  $\lambda_{LF}$  as a function of LF for  $x=1$  at 50mK (black squares) and for  $x=0.45$  at 15mK (red circles). The analysis of the  $x=0.45$  system is presented in Section 4.4.

was refit, obtaining typical reduced- $\chi^2$  values of 1.1. The fitted values of  $\lambda_{LF}$  are shown in Figure 4.12. This figure shows that the value of  $\lambda_{LF}$  seems to be constant at least up to 4T, which is below the critical field. We do not report fitted values of  $\lambda_{LF}$  for our runs at 4.5T and 5T since the signal in these runs is almost decoupled and the fitted parameters have large error bars.

Figure 4.13 shows the fitted value of  $A \cdot A_{total}$  as a function of field <sup>†</sup>. The characteristic size of the internal magnetic field distribution at the muon site can be estimated by how the asymmetry is decoupled. To do this we fitted the data in this figure to the following equation:

<sup>†</sup> Remember from section 3.1 that the total experimental asymmetry, which we call  $A_{total}$ , is different from one; and then, the parameter  $A$  in Equation 4.2 is the relaxing fraction of the asymmetry.

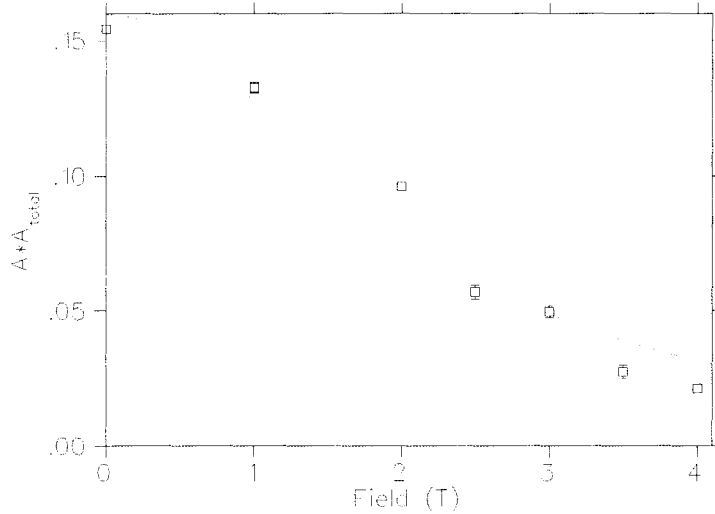


Figure 4.13: Relaxing asymmetry for  $x=1$  at  $T=50\text{mK}$  as a function of longitudinal field. The continuous red line is a fit to Equation 4.3 .

$$A = \frac{H_{\text{int}}^2}{H_{\text{int}}^2 + H^2} \quad (4.3)$$

where  $H_{\text{int}}$  is the characteristic scale of the field distribution and  $H$  is the applied external field. This equation represents the value of  $A$  as a function of LF that would be observed if all the muons feel an internal Transverse Field (TF) equal to  $H_{\text{int}}$  (note that we assume that this value does not change with the externally applied field). The fitted value of  $H_{\text{int}}$  is  $2.0 \pm 0.2\text{T}$  (or  $270\text{MHz}$ ).

It is interesting to notice the two different field scales obtained in the LF fit. One is that of the relaxing front, which is  $\approx 3\mu\text{s}^{-1}$ , and the other is that of the decoupling of the signal,  $\approx 270\mu\text{s}^{-1}$ . This fact can mean that the internal field distribution is anisotropic with two characteristic field strengths. More about this point will be discussed in Section 4.5.

We have interpreted our data in terms of a bare-muon ensemble which probes a field distribution but, before we continue present our results on the  $x=0.45$  system, we would like to discuss other mechanisms of muon-matter interaction which could change this interpretation. First, in  $\text{LiHo}_x\text{Y}_{1-x}\text{F}_4$  the muons are not bare but, as it was seen before, they form F- $\mu$ -F bonds and therefore this interaction should be taken into account when calculating the evolution of the muon polarization under the presence of a local magnetic field. Still, the F- $\mu$ -F interaction can be neglected in the analysis of the low temperature data since the relaxation rate of the muon polarization produced by the internal field is much faster than the characteristic bond frequency. In addition, we should not worry about the F- $\mu$ -F bond influence in the LF signals since at high temperature the F- $\mu$ -F precession was observed to decouple in 100G of LF. We also have considered whether muonium formation could be present in  $\text{LiHoF}_4$ . For example, we wondered if the oscillations observed in low LF could have their origin in the  $\omega_{12}$  Bohr frequency of muonium [67] which could find itself at a high internal transverse field when the system enters the ferromagnetic state. In this case the hyperfine interaction of muonium (4.5GHz for free muonium) is much bigger than that of the F- $\mu$ -F bond formation (0.2MHz); and therefore if muonium was present the interaction of the fluorine nuclei with the muonium atom would have appeared as a perturbation of the muonium Hamiltonian (probably through a hyperfine interaction with the fluorine nuclei). This scenario is in contradiction with the observed F- $\mu$ -F signal (observed down to 15K in the  $x=0.018$  system) which has the right frequency of a bare F- $\mu$ -F bond. It is because of this reason that we do not

believe there is muonium formation in  $\text{LiHoF}_4$ , or at least, that most of the muons do not form it.

We also would like to consider the case in which the low LF oscillations of the signal in the ferromagnetic regime had their origin in muons which land in the silver sample holder and which feel the magnetic field created by the nearby ferromagnetic sample. We do not believe that this mechanism is present either in our measurements since the oscillating signal (which would correspond to the amount of muons which land in the sample holder) seems to have the full asymmetry of the high temperature (paramagnetic) signal, furthermore, there is no change in  $\alpha$  when going into the ferromagnetic regime as one would expect from muons in the sample holder which start to depolarize as the sample enters in the ferromagnetic state.

#### 4.4 $\text{LiHo}_{0.45}\text{Y}_{0.55}\text{F}_4$

The behavior of the signals from the  $x=0.45$  sample is qualitatively the same as those from the  $x=1$  sample. Below  $T_c$  we observed precession of the  $\mu\text{SR}$  signal (see Figure 4.14) and therefore we fit the low LF data (13.5G) using Equation 4.1. The fitted values of  $f_{\text{ferro}}$  are shown in Figure 4.9. We observed the first nonzero value of  $f_{\text{ferro}}$  at 0.7K upon cooling. It is interesting to notice that the point at 0.2K shows a decrease in  $\lambda_1$  and  $f_{\text{ferro}}$ . This effect happens at the hyperfine energy scale and, therefore, it is possible that it is due to the depopulation of the hyperfine levels. The depopulation of the hyperfine levels can affect the dynamical behavior of the magnetic moments, which would be reflected in  $\lambda_1$ ; and this can affect  $f_{\text{ferro}}$  through a small trade off between the

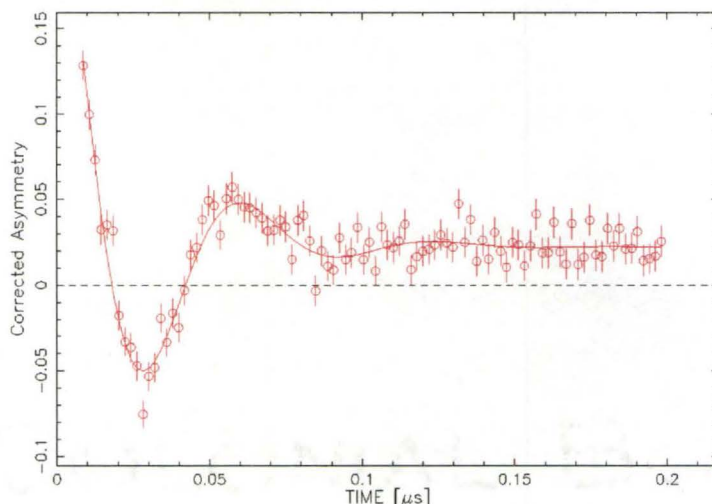


Figure 4.14: Corrected asymmetry for the  $x=0.45$  sample in low LF (13.5G) and early times. The oscillating asymmetry is evidence for the ferromagnetic state.

two fitting parameters. It is also possible that this decrease in  $f_{\text{ferro}}$  is due to a statistical fluctuation of the fit at at this single point. An other run at this field and temperature would be needed to rule out this last scenario.

The behavior of  $\lambda_1$  with temperature follows the same trend as that of the  $x=1$  with a smaller average value inside the ferromagnetic regime (see Figure 4.10). The smaller value for  $\lambda_1$  is an effect of dilution. The random nature of dilution can broaden the magnetic field distribution from an ordered system but, at the same time, it increases the average distance between muons and magnetic moments, decreasing the magnetic field strength at the muon site. The combination of these two effects is such that in this case the overall relaxation rate decreases.

The high LF data of the  $x=0.45$  also follows the same behavior as that of the  $x=1$  system so we used Equation 4.2 to fit it. A preliminary fit showed

the value of  $\beta_{\text{LF}}$  to be again approximately equal to 0.7 and, therefore, it was fixed to this value for the final fit. The values for  $\lambda_{\text{LF}}$  are shown in Figure 4.12. It can be seen that  $\lambda_{\text{LF}}$  seems not to have any temperature dependence below the critical field ( $H_c \approx 1.7\text{T}$  for  $x=0.45$  at  $T=0$  [27]) as observed for the  $x=1$  system (which has  $H_c=4.95\text{T}$  and therefore all our measurements shown in Figure 4.12 are below the critical field). Above  $H_c$ ,  $\lambda_{\text{LF}}$  seems to increase as you get deeper into the paramagnetic regime.

The LF signal displayed decoupling up to the highest fields (3T), showing the system is static within our time window. This again indicates the absence of low lying magnetic excitations in this system at 15mK and up to 3T in the paramagnetic regime (the muon Zeeman splitting at 3T is 20mK or  $1.7\mu\text{eV}$ ). The decoupling of the signal can give us an internal field scale by fitting the values of  $A$  using Equation 4.3.  $H_{\text{int}}$  was found to be equal to  $1.30 \pm 0.05\text{T}$ . The reader can observe that in this sample also there are two different field scales in the LF signals. One for the time dependent part ( $\approx 1.5\mu\text{s}^{-1} \approx 0.01\text{T}$ ) and one for the decoupling of the signal ( $\approx 175\mu\text{s}^{-1} \approx 1.3\text{T}$ ). As we will discuss in Section 4.5, we believe that these two field scales correspond to two different parameters which characterize the structure of the field distribution.

For this system we also performed a Transverse Field (TF) scan at base temperature (15mK). In these measurements the muon spin was rotated so it lay perpendicular to the external field (which was kept along the (310) crystallographic direction). The TF signal had two components which relaxed at different rates (see Figure 4.15). Each signal was fitted in two parts: first the long time part of the signal, with only the slow relaxing component, was

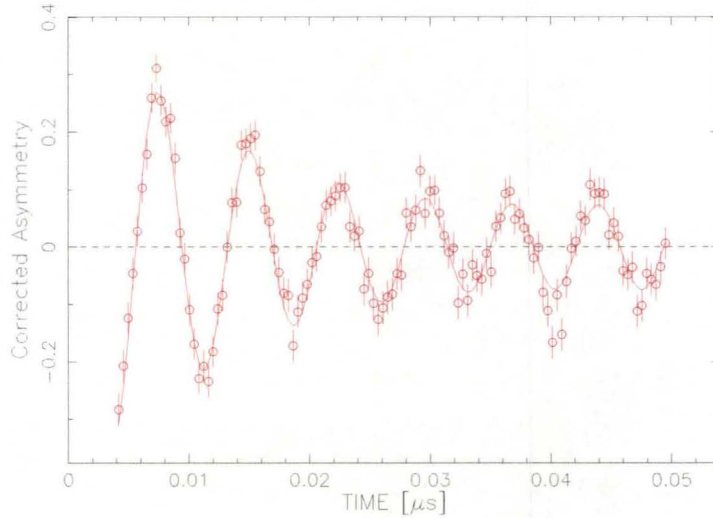


Figure 4.15: Corrected asymmetry for  $x=0.45$  in a TF of 1T, the slow and fast relaxing components of the signal can be observed in this picture.

fitted in the rotational reference frame [88]; and then the very early times were fitted in the laboratory frame keeping the slow relaxing component constant. The polarization function used to fit the TF data is:

$$G_{TF}(t) = Ae^{-\lambda_{\text{fast}}t} \cos(2\pi f_{\text{fast}}t + \phi) + (1 - A)e^{-\lambda_{\text{slow}}t} \cos(2\pi f_{\text{slow}}t + \phi) \quad (4.4)$$

The fitted value of  $A$  was found to be  $\approx 0.8$  and the fitted values of  $\lambda_{\text{slow}}$  and  $\lambda_{\text{fast}}$  are shown in Figure 4.16. It is likely that the slowly relaxing component, which corresponds to 20% of the muons, is produced by muons which land in the silver sample holder. Measurements in the dilution refrigerator spectrometer generally have a background component from muons which land in the holder. The typical relaxation rate of muons which land in the sample holder is  $\sim 0.1\mu\text{s}^{-1}$ , but Figure 4.16 shows that the relaxation rate of this fraction is an order of magnitude bigger than that. This increase in the relaxation rate is

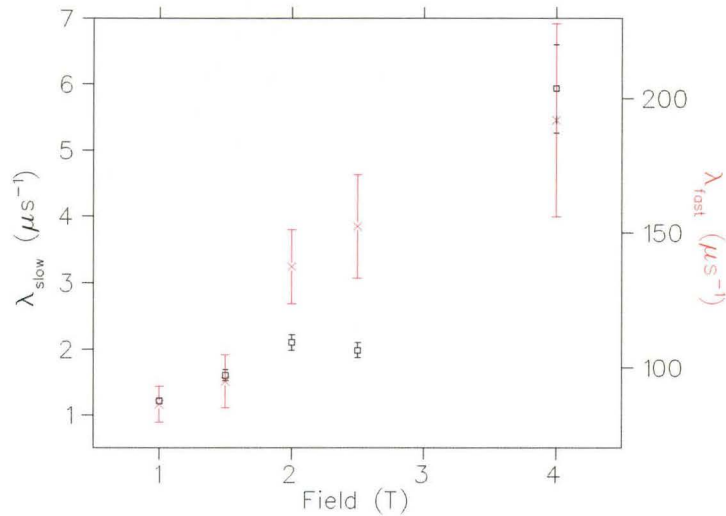


Figure 4.16:  $\lambda_{\text{fast}}$  (red crosses on the right axis) and  $\lambda_{\text{slow}}$  (black squares on the left axis) as a function of TF at 15mK in  $x=0.45$ .

most probably produced by the nearby ferromagnetic sample which broadens the field distribution in the sample holder. At 15mK the  $x=0.45$  system is driven paramagnetic in an external field bigger than 1.7T, still it is possible that the highly polarized paramagnetic sample broadens the field distribution in the holder.

The fraction of muons which depolarize rapidly correspond to muons that landed inside the sample then, since we know from the LF measurements that the magnetic field environment is static,  $\lambda_{\text{fast}}$  corresponds to the characteristic width of the internal field distribution along the externally applied magnetic field (times a factor of order one which depends on the actual shape of the field distribution) [70]. This is,  $\lambda_{\text{fast}}$  is the width of the field distribution along the crystallographic (310) direction. Unfortunately knowing the width of the

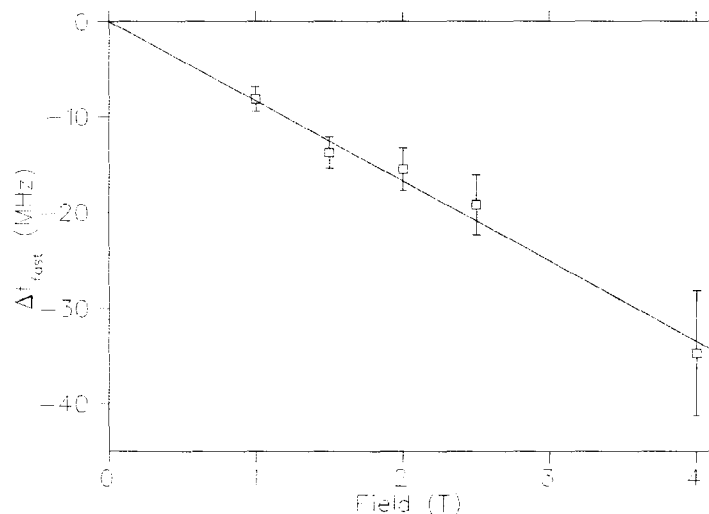


Figure 4.17: Frequency shift of the fast component of the TF signal as a function of externally applied magnetic field at 15mK in  $x=0.45$ .

field distribution along other directions and eventually its shape, is a difficult task which we discuss in the next section.

The contribution from the sample to the total field can be obtained from the frequency shift of the fast component with respect to the externally applied field. This is, by calculating:

$$\Delta f_{\text{fast}} = f_{\text{fast}} - \gamma_{\mu} H_{\text{ext}} \quad (4.5)$$

This quantity is shown in Figure 4.17. The line in this plot is a fit to  $\Delta f_{\text{fast}} = a * H$  which produce a value of  $-8.4 \pm 0.3 \text{ MHz/T}$  for  $a$ .

## 4.5 Comments on the ferromagnetic state

Figure 4.18 shows the fitted values of  $f_{\text{ferro}}$  (which, as we show in Section 4.3, is proportional to the order parameter) together with two plots of the  $H = 0$  mean field order parameter of the TFIM calculated using Equation 1.3 and setting  $T_c$  equal to 1.54K. The the mean field order parameter plots are not fits to the data and they are just shown for comparison with the measurements. The continuous line has been chosen such that it approximately matched the low temperature points, while the dashed line was chosen such that it represents closer the trend in the higher temperature points. From this figure we would like to notice that the mean field formalism can not describe accurately the trend of the order parameter of the system close to the critical temperature (not even if  $T_c$  is allowed to vary). This discrepancy has been observed also in the  $H$ - $T$  phase diagram for this system [13] (remember that at low values of  $H$  the relation  $H \propto M$  is valid). Recently it has been shown that, to account for this discrepancy, the magnetic domain structure has to be taken into account by the theory [49] (thing that can not be done with a simple mean field treatment). In Chapter 6 we will further discuss the importance of the magnetic domain structure in the ferromagnetic phase of  $\text{LiHo}_x\text{Y}_{1-x}\text{F}_4$ .

Figure 4.9 shows that for the  $x=0.45$  system the order parameter not only has a lower  $T_c$ , as expected for a system with lower  $x$ , but it grows slower than that of the  $x=1$  system close to  $T_c$  (see also Figure 6.1 for a scaled plot). This effect might be produced by the random doping of the  $x=0.45$  system which in zero (or low) external field produce random dipolar fields along the Ising direction. As the thermal average of the magnetic moment (or magnetization)

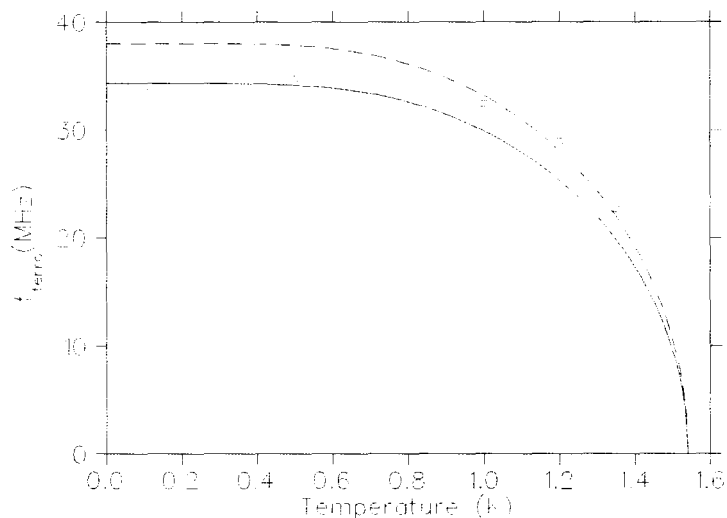


Figure 4.18:  $f_{\text{ferro}}$  as a function of temperature for the  $x=1$  sample. The continuous line is the mean field order parameter from the TFIM with  $T_c=1.54\text{K}$  and scaled such that  $f_{\text{ferro}}=35\text{MHz}$  at  $T=0$ . Dashed line is the same order parameter but with  $f_{\text{ferro}}=38\text{MHz}$  at  $T=0$ .

grows with lowering temperature, so could be the strength of the internal random fields and, since random fields compete with the ferromagnetic order (Section 1.2), this would produce a slower increase in the order parameter. The continuous red curve in Figure 4.19 shows that random longitudinal fields which are proportional to the order parameter can indeed produce a slower increase on  $\langle m_z \rangle$ . This curve was calculated using the mean field solution of the ferromagnetic random TFIM (Equation 1.8) with  $H=0$  and with the strength of the random field proportional to the magnetization ( $z_0 \rightarrow \langle S_z \rangle z_0$ ). An analogous effect has been shown to occur in the  $H$ - $T$  phase diagram, but in that case the random field is strengthened by the field-induced transverse random fields as shown in Reference [54].

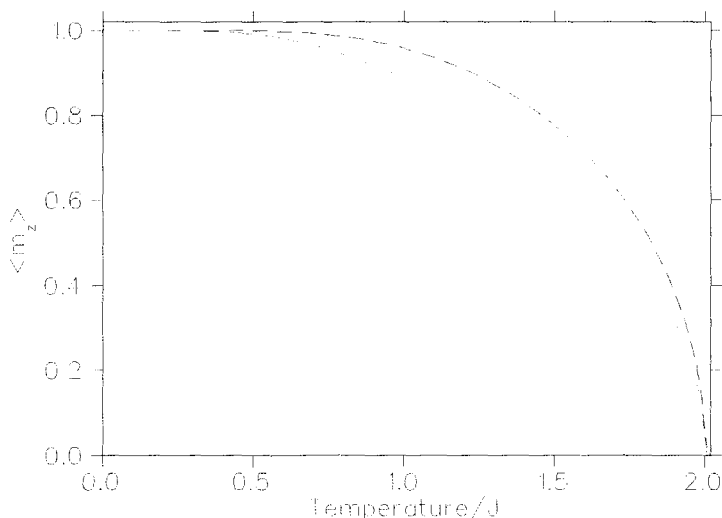


Figure 4.19: Mean field solution of the Ising model with infinite ranged ferromagnetic interactions. The continuous red line is the solution with binary random fields proportional to the order parameter; and the dashed black line was calculated without random fields. The random field strength used was  $H/J=0.8$  (see Equation 7 in Reference [6]).

Fits of our data at base temperature and in the presence of a field produced a series of field scales which are summarized in Table 4.2. Unfortunately, constructing a magnetic field distribution which could account for our observations when an external field is applied ( $H \geq 1\text{T}$ ) is a hard task which has not been accomplished yet. It is because of this reason that the amount of information that we have been able to extract from our LF and TF measurements is limited. In the remaining of this section we discuss some characteristics of the internal field distribution for  $H \geq 1\text{T}$  which can be implied from our LF and TF data.

The internal magnetic field distribution at the muon site for  $H \geq 1\text{T}$  has a structure with different field scales. In order to show this, we can calculate the ratio of  $\lambda_{\text{LF}}/H_{\text{int}}$  from Table 4.2. This ratio is  $\approx 96$  for the  $x=1$  sample,

Parameter	x=1 (MHz, $\mu s^{-1}$ )	x=0.45 (MHz, $\mu s^{-1}$ )
$f_{\text{ferro}}$	$35.1 \pm 0.4$	$15.7 \pm 0.2$
$\lambda_{\text{ferro}}$	$42 \pm 4$	$32 \pm 1$
$\lambda_{\text{LF}}$	$2.8 \pm 0.2$	$1.36 \pm 0.08$
$H_{\text{int}}$	270	175
$\lambda_{\text{fast}} @ 1\text{T}$	-	$86 \pm 7$

Table 4.2: Compilation of characteristic field strength for the x=1 system at 50mK, and for the x=0.45 system at 15mK.

and  $\approx 128$  for the x=0.45 one. In the case of a spherical field distribution, for example, all the behavior of the signal is described by only one field scale (*e.g.* the spherically symmetric field distributions from the Kubo-Toyabe theory on Section 3.4.1 were described by one parameter:  $\Delta$  or  $a$ ); and the ratio  $H_{\text{int}}/\lambda_{\text{LF}}$  is of order one. A non spherical field distribution might need more than one variable to characterize it, therefore introducing different field scales in the problem (as in the case of the stretched field distributions in Section 3.4.3). The presence of different field scales will be reflected in the value of  $H_{\text{int}}/\lambda_{\text{LF}}$  and, if one scale is much bigger than the other one, this ratio will significantly differ from one, as seen in our measurements.

One known fact about the internal field distribution for  $H \geq 1\text{T}$  and x=0.45, is that its characteristic width along the [310] direction is given by  $\lambda_{\text{fast}}$  (times a factor of order one<sup>‡</sup>). This parameter was found to be approx-

---

<sup>‡</sup> This factor depends on the shape of the internal field distribution and therefore is unknown. For a Gaussian distribution the factor is  $\sqrt{2}$  [70].

imately constant within the ferromagnetic state and has a value of  $\approx 90\mu s^{-1}$ . It is expected that the decoupling of the signal in LF would scale with this same characteristic field width, since the decoupling is most sensitive to field components parallel to the initial muon spin direction (the origin of the decoupling is in the  $\cos^2(\theta)$  term in Equation 3.10). This is what we actually found from the value of  $H_{\text{int}}$  which is 174MHz and is similar to  $\lambda_{\text{fast}}$  (once it would be multiplied by the unknown  $\mathcal{O}(1)$  factor).

In order to know if the field scales shown in Table 4.2 are sensible, we calculated numerically the internal magnetic field at the muon site (assumed to be between nearest neighbor fluorines) for the  $x=1$  system in the ferromagnetic state. The calculation was performed adding the dipolar field produced by a spherical lattice of  $7\mu_B$  Ho moments with radius equal to  $1500\text{\AA}$  and at which center was the muon site assumed to lie half way between nearest neighbor fluorine ions. This calculation of the magnetic field in is a conditionally convergent one and we have arbitrarily chosen a spherical sample shape. Nevertheless, we are only interested in an order of magnitude and therefore our estimation should be useful regardless of the sample shape. This calculation gave a field strength of  $\approx 3\text{T}$  ( $405\mu s^{-1}$ ) which is the same order of magnitude as the measured decoupling field scale of  $2\text{T}$  (or  $270\mu s^{-1}$ ) in the  $x=1$  system.

## 4.6 Overview

The  $\mu\text{SR}$  measurements from the ferromagnetic systems with  $x=1$  and  $0.45$  have a similar qualitative behavior. At high temperature and in a low LF of  $20\text{G}$ , the  $\text{Ho}^{3+}$  ions fluctuate very fast and we observe the characteristic

oscillations of the formation of an F- $\mu$ -F bond with a length of 1.2Å. Upon cooling, the Ho<sup>3+</sup> ions start slowing down, and at 20K their fluctuation rate enters the  $\mu$ SR time window. Upon further cooling we observe ferromagnetism arise in both of our systems, evidenced by spontaneous oscillations of the muon ensemble. The oscillations are damped rather fast due to a broad internal field distribution. This broadening is caused most probably by the splitting of the system into ferromagnetic domains. The spontaneous oscillations allowed us to trace the ferromagnetic order parameter down to 15mK. For the x=1 system the order parameter shows deviations from the mean field solution of the Ising model. We believe that these deviations are due to the splitting of the sample into ferromagnetic domains. The order parameter from the x=0.45 system shows a slower increase upon cooling. We have shown that a slower increase in the order parameter can be explained by the generation of internal random longitudinal fields which are proportional to the order parameter. When an external LF was applied at 15mK we observed decoupling of our signals with a completely flat tail at long times. This gives evidence for static magnetism within the  $\mu$ SR time window (with no low lying excitations) at these fields and temperature.

## Chapter 5

### $\mu$ SR studies of systems with $x \leq 0.25$

In this chapter we present the results of our  $\mu$ SR measurements for the  $x=0.25$ , 0.12, 0.08, 0.045 and 0.018 samples. The chapter is divided in two sections, one dedicated to the analysis of the data from the magnetically dense  $x=0.25$  system, and another one which presents the results of all the more diluted samples together.

Analyzing the data of  $\text{LiHo}_x\text{Y}_{1-x}\text{F}_4$  at high dilutions was a very challenging task. One of the problems encountered was to identify the background signal in low Longitudinal Field (LF) which was mentioned at the end of Section 4.2. It was noticed during early analysis of our data, that there was a partial decoupling of the signal with a LF as low as  $\approx 50\text{G}$ , as shown in the raw asymmetry\* spectra in Figure 5.1. In order to know if this decoupling was intrinsic to the sample, we tested different microscopic models (*e.g.* different stretched-distribution models as in Section 3.4.3, the Uemura spin glass function [73], etc.) to fit the data of the diluted (random) systems. All these models could, in principle, produce a fast decoupling at long times. Never-

---

\* The raw asymmetry spectrum is the straight output from Equation 3.7, that is, without correcting for  $\alpha$  and  $\beta$

theless, no model produced a satisfactory explanation of the the data of the  $x \leq 0.25$  samples. Using phenomenological power-exponential fits we realized that the amplitude and relaxation rate of the background fraction was temperature independent for a given sample and beam line (constant even if a phase transition was crossed as in the case of the  $x=1$  and 0.45 systems). To account for the background, we fitted our low LF data adding a constant Gaussian term. The amplitude and relaxation rate of this term were usually determined by fitting a low LF run (with a background term) together with a  $\sim 100\text{G}$  LF run (where the relaxation rate of the background was fixed to zero) at the same temperature. Table 4.1 on Section 4.2 shows the fitted amplitudes and relaxation rates the background in the different samples and beam lines.

The origin of this temperature independent background is not known to us. Table 4.1 shows that this signal was most common in the dilution refrigerator measurements (observed in 6 of the 8 beam periods) than in those from the He flow cryostat (in 2 of the 7 beam periods see Table 4.1). In the He flow cryostat line the measurements were performed using a low-background sample holder, so it is most probable that the background is not intrinsic to the sample but due to muons which land in other places than the sample (*e.g.* cryostat walls or sample holder). Since we could easily fit out this small and temperature independent fraction of muons, we did not consider necessary any further measurements to investigate its origin.

Another difficulty we encountered when analyzing the data of  $\text{LiHo}_x\text{Y}_{1-x}\text{F}_4$  was determining the total asymmetry (*i.e.* amplitude) of our signals. It was not possible to perform a weak transverse field run in this system since at

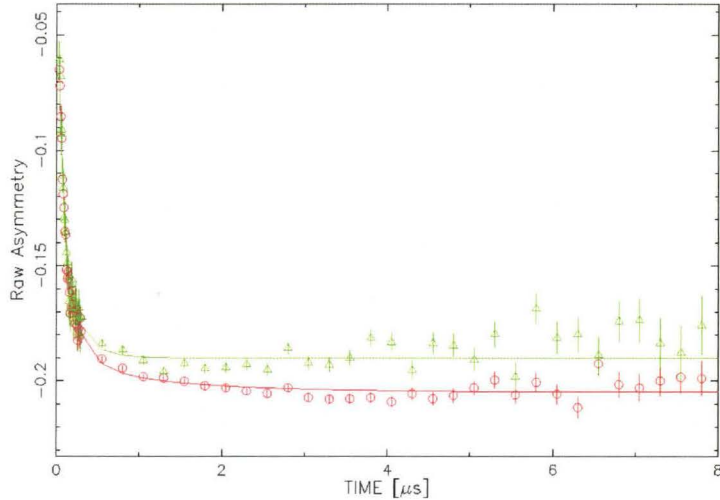


Figure 5.1: Raw asymmetry of the  $x=0.08$  sample at 15mK. Red circles is data in a LF of 5G while green triangles is data in 100G. The decoupling of the background is shown in the different position of the long time tails.

high temperature the  $F\text{-}\mu\text{-}F$  frequency is of equal size as the muon precession frequency and therefore the spectra presented small oscillations at many frequencies instead of the whole precession of the asymmetry. At lower temperatures the fast relaxation of the signal produced by the large Ho magnetic moments prevented us from observing any oscillation of the asymmetry under weak transverse field. We finally decided to extract the total asymmetry from fitting the low LF runs at 10K where the signal relaxed almost exponentially and there was a zero-asymmetry flat tail at long times. Still, not knowing the total asymmetry precisely is a source of uncertainty in our analysis, especially when the signal relaxes rapidly.

Fitting our data to microscopic models (*e.g.* Kubo-Toyabe) was also challenging. It was observed many times, for example, that when a microscopic model was used, the fitted parameters would trade against each other and/or

show large fluctuations. We had to be especially careful in choosing which parameters had to be fixed during the fit of microscopic models. More details about this issue will be presented later.

In this chapter we present two types of analysis for each sample: a phenomenological one (using power exponential functions), and a microscopic-model-based one (using functions based on the Kubo-Toyabe formalism). For this reason both sections of this chapter are further divided in two subsections, each of which presents the results of a type of analysis. Both of these fits are complementary and they were checked against each other for self consistency.

## 5.1 $\text{LiHo}_{0.25}\text{Y}_{0.75}\text{F}_4$

In this section we present our results on the  $x=0.25$  system. This system, which is expected to lie close to the boundary of the ferromagnetic and spin glass phases, has not been studied before. The sample was prepared as described in Section 4.1 and the experimental details are outlined in Section 3.3.

### 5.1.1 Phenomenological analysis

In this system, as in the ferromagnetic samples presented in the previous chapter, the relaxation rate of the signal increases below  $\approx 20\text{K}$  due to the slowing down of the magnetic Ho ions. Figures 5.2 and 5.3 show the behavior of the the  $\mu\text{SR}$  spectra as a function of temperature and LF respectively. At base temperature the  $\mu\text{SR}$  signal relaxes to zero even if a LF is present. This

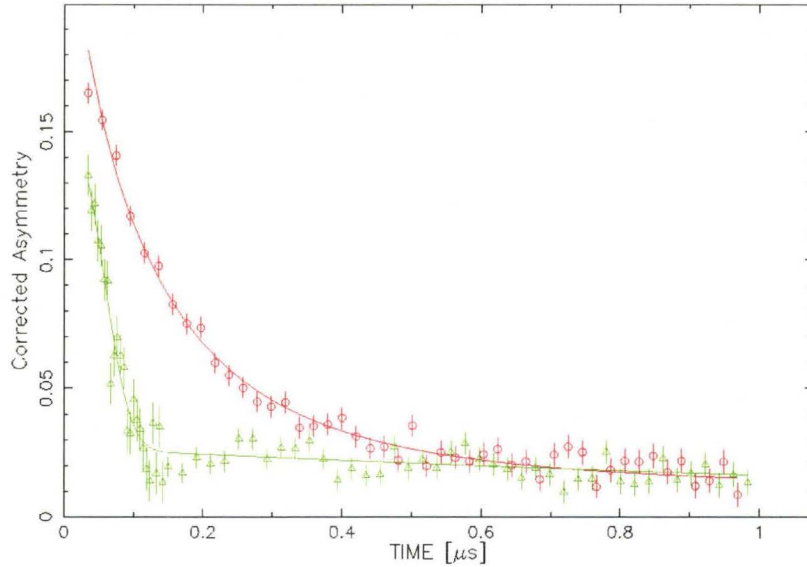


Figure 5.2:  $\mu$ SR signals in ZF for  $x=0.25$  at 3.5K (red circles) and 0.025K (green triangles). Continuous lines are fits to a power exponential function as described in the text.

means that the Ho moments remain dynamic within the  $\mu$ SR time window down to 25mK.

It is a common practice to fit  $\mu$ SR data from spin glasses to a power exponential function [89]. Then, since the  $x=0.25$  system is expected to lie near the boundary of the ferromagnetic-spin glass state, we used the following phenomenological function to analyze the data below 15K:

$$G_z(t) = Ae^{-(\lambda t)^\beta} + (1 - A)e^{-(\lambda_B t)^2} \quad (5.1)$$

In this equation the Gaussian term represents the temperature independent background alluded to in the introduction of this chapter. This term was

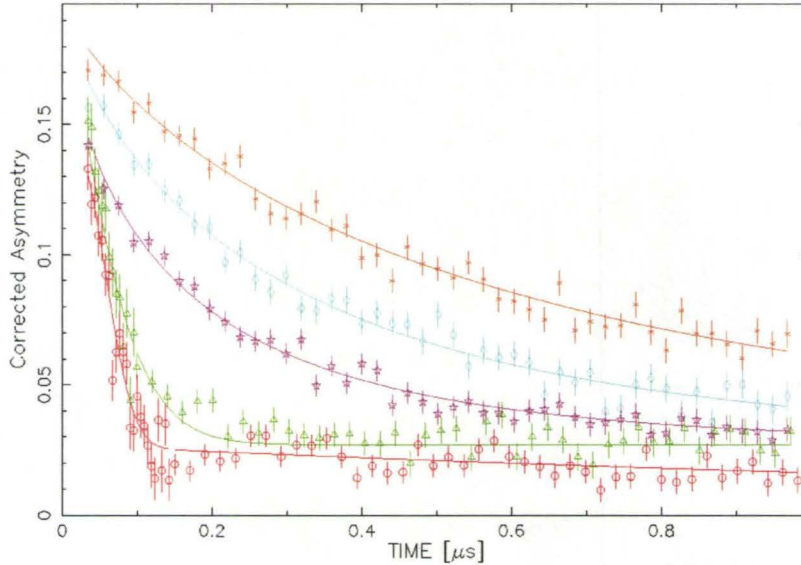


Figure 5.3:  $\mu$ SR signals for  $x=0.25$  at 25mK and as a function of LF: ZF (red circles), 100G (green triangles), 500G (magenta stars), 1000G (aqua diamonds) and 2000G (brown crosses).

determined by performing a global-fit<sup>†</sup> of the Zero Field (ZF) data where  $A$  and  $\lambda_B$  were common to all the runs (this background was then checked against the value obtained in a global fit of a ZF and a 100G run). The amplitude and relaxation rate of the background is reported in Table 4.1; no background was observed in the runs taken in the He flow cryostat. Since the background was completely decoupled at 100G, we set  $\lambda_B$  equal to zero in all the fits of runs with LF different from zero. All the fits were performed with  $A$  fixed to the value found at high temperature and ZF. Typical values for the reduced  $\chi^2$  of the fits of the ZF data were 1.22.

<sup>†</sup> In a global-fit, several  $\mu$ SR signals are fitted simultaneously with some common fitting parameters.

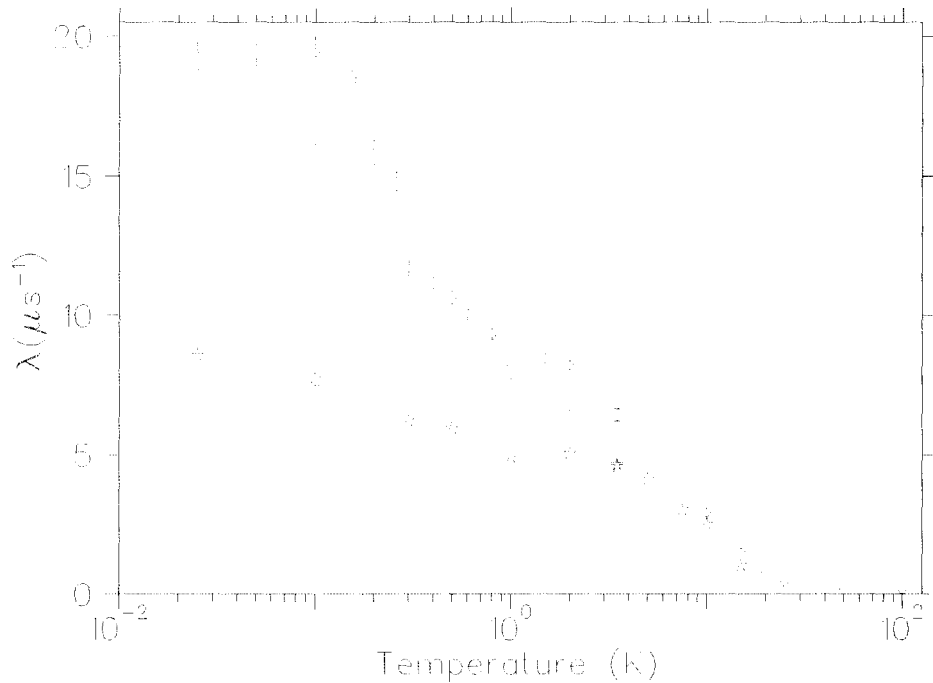


Figure 5.4: Relaxation rate of the  $\mu$ SR signal for  $x=0.25$  as a function of temperature for different LF: ZF (red circles), 100G (green triangles), 500G (magenta stars), 1000G (aqua diamonds) and 2000G (brown crosses). The fitting function is Equation 5.1.

The fitted values for  $\lambda$  in Equation 5.1 are shown in Figure 5.4 as a function of temperature and LF. Comparing the ZF results in Figure 5.4 with those from the  $x=1$  and 0.45 systems (Figure 4.10), it can be seen that the relaxation rate at base temperature is smaller in the present case. This is due to a smaller average field at the muon site caused by the fact that the muons are on average further from the Ho ions at this doping level. As it will be shown later, the increase of  $\lambda$  below 0.3K is due to a further slowing down of the magnetic Ho ions.

Figure 5.5 presents the temperature dependence of the power parameter  $\beta$  in Equation 5.1 as a function of temperature and LF. This parameter shows a transition from an almost exponential behavior at high temperature to a more Gaussian-like as the temperature is lowered in ZF. An early time relaxation of the asymmetry with an exponent equal to 2 is characteristic of magnetically dense random systems with medium or low fluctuation rates (see the Gaussian Kubo-Toyabe (GKT) function in Figure 3.6). On the other side, in very diluted magnetic systems the exponent of the relaxation function decreases to 1 (note the exponential behavior of the Lorentzian Kubo-Toyabe (LKT) function at early times on Figure 3.8). The  $x=0.25$  system is at an intermediate dilution level so the value of  $\beta$  at base temperature and ZF lies at an intermediate point between these limits (numerical simulation which placed random moments in a cubic lattice have shown that the  $x=0.2$  system can produce  $\mu$ SR spectra with an intermediate coefficient [71]).

The increase of  $\beta$  from 0.9 to 1.5 upon cooling and in ZF can be understood from the Kubo-Toyabe model. In Section 3.4.2 we saw that the relaxation rate of a GKT in ZF was exponential (power equal to 1) when the internal field fluctuates very fast. So the power of the dynamical GKT goes from 2 to 1 as the fluctuation rate increases. The same is true for the LKT where the exponent goes from 1 at slow fluctuation rates, to 0.5 at higher ones. Again, the  $x=0.25$  system is at an intermediate dilution so, as the fluctuation rate of the internal magnetic field increases with temperature, the value of  $\beta$  decreases.

The decrease of  $\beta$  upon the application of a LF at base temperature is also predicted by the Kubo-Toyabe formalism. As shown in Equation 3.19, at high

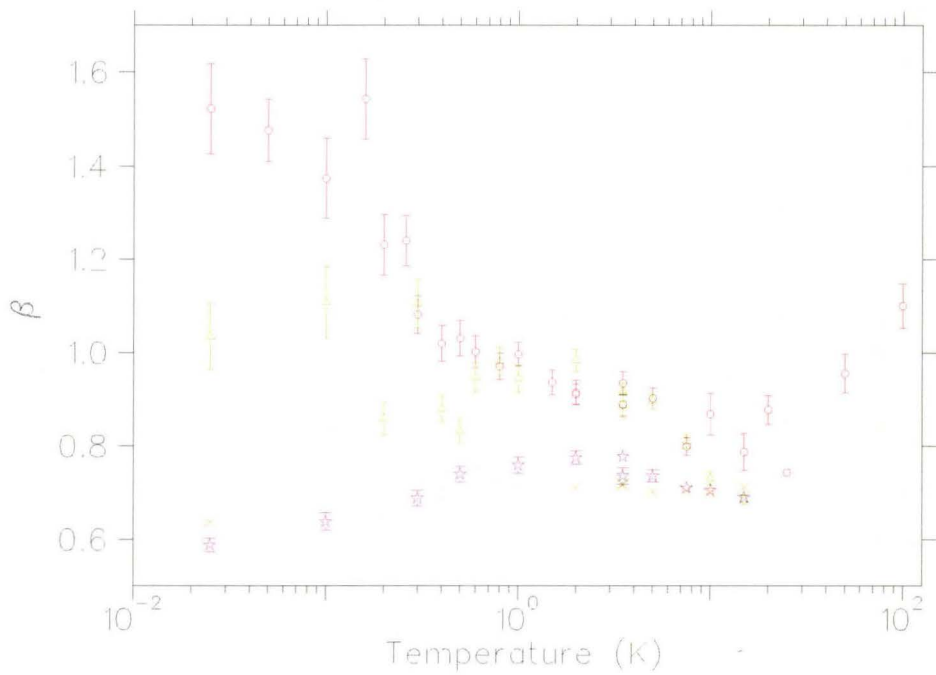


Figure 5.5: Power of the  $\mu$ SR signal as a function of temperature and LF: ZF (red circles), 100G (green triangles), 500G (magenta stars), 1000G (aqua diamonds) and 2000G (brown crosses). The fitting function is Equation 5.1.

LF and slow fluctuation rate the relaxation of the GKT is exponential, so the exponent decreases from 2 to 1 upon the application of a LF. This same effect is observed in our system where the exponent decreases from about 1.5 to 0.6 upon the application of a LF.

We want to point out that the value of  $\beta$  in ZF increases monotonically from 0.9 to 1.5 upon cooling. This is in contrast with the behavior of diluted spin glass systems where the value of  $\beta$  slowly decreases upon cooling to approximately  $1/3$  at  $T_g$ . This decrease in  $\beta$  is believed to be due to the widening of the relaxation spectrum of the system and also to the development of non exponential time correlation functions of the magnetic moments[89]. Then, below  $T_g$ , the power should increase again as the magnetic moments slow down and the averaged moment size (the Edwards-Anderson order parameter in Equation 1.11) acquires a non zero value.

### 5.1.2 Microscopic analysis

As we have seen, it is possible for a dynamical Kubo-Toyabe model to account for the temperature and field behavior of  $\beta$  shown in Figure 5.5. It is for this reason we present the analysis of our data using a GKT function. This analysis was performed only in the low temperature data taken in the dilution refrigerator since we are most interested in the low temperature properties of the system.

The  $x=0.25$  system seems to be at an intermediate dilution between the dense Gaussian and the diluted Lorentzian cases. Nevertheless, since no Kubo-Toyabe model has been produced which can be used in magnetically diluted

systems with intermediate dilutions, we have analyzed our functions using a dynamical GKT model. The reason for choosing a Gaussian and not a Lorentzian function was based purely on how the signals look, which seem to be closer to that of the Gaussian type. Even though we expect our fitted values to be quantitatively biased, fitting the data to the Gaussian model can at least provide us with the qualitative evolution of the fluctuation rate of the magnetic moments as a function of temperature and LF.

We fit the low temperature data from the dilution refrigerator ( $T \leq 3.5\text{K}$ ) using a dynamical GKT with the same value of  $\Delta$  (see Equation 3.12 for the static case). Doing this has the advantage of restricting the number of free parameters <sup>‡</sup> and it is justified by the fact that, for practical purposes, the holmium ions possess a constant Ising character in this temperature range (the parameter  $\Delta$  in the GKT function depends not only on the magnetic moment size, because the local field is proportional to it, but also it depends effectively in the Ising nature of the magnetic moments since this affects the shape of the internal magnetic field distribution). That the holmium moments have an approximately constant Ising nature below 3.5K can be observed in Figure 5.6. This figure shows the thermal average of the Ising component of the angular moment of a single Ho ion as a function of temperature; and it was obtained by numerically diagonalizing the single ion part of the Hamiltonian in Equation 2.1 and using the eigen values and eigen vectors to obtain:

---

<sup>‡</sup> Our  $\mu\text{SR}$  signals relax so fast that the fewer the number of free parameters in the fit the less noisy their fitted values are.

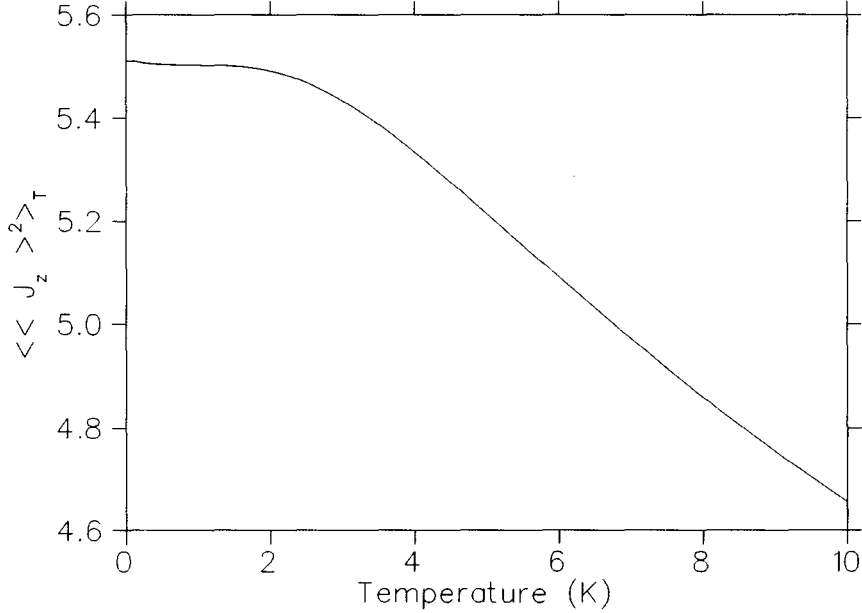


Figure 5.6: Thermal average of the single  $\text{Ho}^{3+}$  moment size as a function of temperature. This plot was obtained by numerical diagonalization of the density matrix of the single ion part of the Hamiltonian in ZF.

$$\langle\langle J_z^2 \rangle\rangle_T = \frac{\sum_i \langle i | J_z^2 | i \rangle e^{-(E_i/K_B T)}}{Z} \quad (5.2)$$

where the sum on  $i$  runs over all the eigen states and  $Z$  is the partition function. The diagonalization of the single ion Hamiltonian was achieved using the *ZHEEV* routine of the *LAPACK* [90] numerical library. The Stevens coefficients used in our calculation are those recommended by Reference [17] and the strength of the hyperfine interaction was that reported in Reference [16].

The fitted value of  $\Delta$  was found to be  $17.7 \pm 0.2 \mu\text{s}^{-1}$ , which was obtained by performing a common fit of a ZF run together with a 500G run at base temperature. The LF field (which is transverse to the Ising axis) is expected to renormalize the magnetic moment size of the Ho ions [45], and therefore,

this should affect the value of  $\Delta$  (see Section 3.4.1). At base temperature we could fit our data in ZF, 100G and 500G with a single value of  $\Delta$ . For fields above 500G the fast relaxing (static) front of the signal cannot be observed and, therefore, the value of  $\Delta$  can not be determined for these fields (only a single relaxation rate is observed at high LF and therefore  $\Delta$  and  $\nu$  can not be determined independently, see Equation 3.19). Since the magnitude of the magnetic moment is not expected to change much for LF smaller than 2T [45], we have fitted our high LF data (up to 0.5T) with the same value of  $\Delta$  that was found from fitting the low LF runs.

The temperature evolution of the fluctuation rate of the local magnetic field (parameter  $\nu$  in the strong collision model, see Section 3.4.2) as a function of temperature is shown in Figure 5.7. The reduced  $\chi^2$  values for the ZF and 100G temperature scans were observed to increase with temperature. Below 0.4K, the typical value of the reduced  $\chi^2$  was 2 for the ZF scan, while it was 1.5 for the 100G scan. Above this temperature the typical reduced  $\chi^2$  value of the ZF scan increased to 3, while that of the 100G was 2.5. The values of  $\chi^2$  are a bit off from the optimal value of one because of two reasons: first, because we are using a GKT function to fit an intermediate dilution system, and second, because the shape of the internal field distribution might differ from that of a sphere (which the GKT model assumes, see next section). Also, the reason why the fits at 100G are better than those in ZF is because the background term, which is present in the ZF scan, could not be fitted accurately. Actually, fitting a ZF run and a 100G run with a common fluctuation rate barely altered the quality of the fit. This means that, not only that the value of  $\nu$  is the same in ZF and 100G, but also that the bigger values of reduced  $\chi^2$  in ZF are due

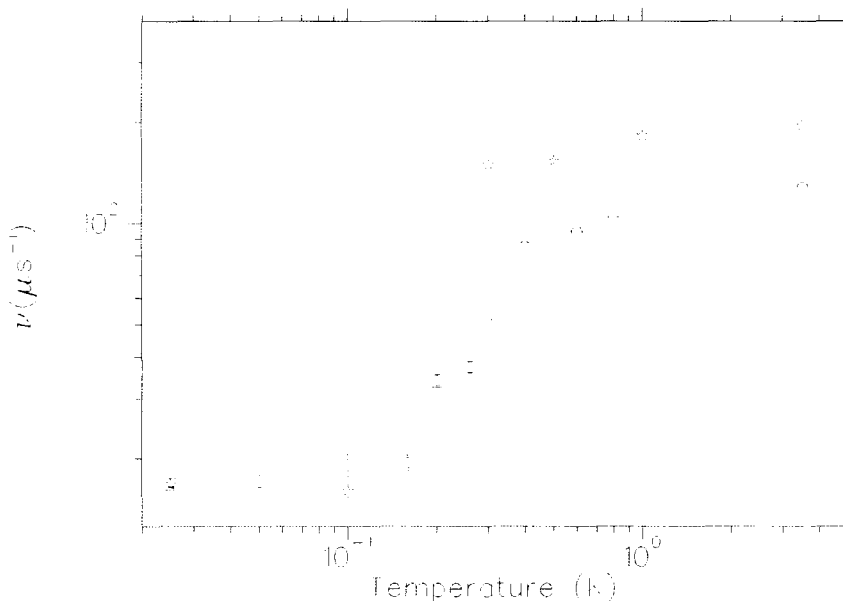


Figure 5.7: Fluctuation rate of the internal magnetic field for the  $x=0.25$  sample as a function of temperature at different LF: ZF (red circles), 100G (green triangles), 500G (magenta stars) and 1000G (aqua diamonds).

to the presence of the background term. At 500G the fast front end is barely visible and the signal looks almost exponential (see Figure 5.3). The value of the reduced  $\chi^2$  did not depend in temperature at this LF and had an averaged value of  $1.3 \pm 0.3$  (the uncertainty being the standard deviation). The average value for the reduced  $\chi^2$  in the 1000G temperature scan was  $1.5 \pm 0.3$ .

Figure 5.7 shows that for fields smaller than 500G there is a steady decrease of  $\nu$  upon cooling until  $\approx 0.4$ K. At this point  $\nu$  decreases at a faster rate until it levels off below  $\approx 0.15$ K. The decrease of the fluctuation rate starting at around 0.4K coincides with that expected from the evolution of  $\beta$  with temperature (Figure 5.5) as mentioned in the previous section. Notice also that for  $T > 0.3$ K the 500G temperature scan has a higher value of  $\nu$  than that of the ZF and

100G one. It cannot be ruled out that this effect is due to some systematic error caused by using the Dynamical Gaussian Kubo-Toyabe functions to fit the data, but it should be remembered that field induced fluctuations are expected in the transverse field Ising model. It is actually this effect which we believe is responsible for the higher fluctuation rate of the 1000G scan. A small reduction in  $\nu$  can also be observed in this scan at  $\approx 0.3\text{K}$ . It seems then that the temperature below which the system slows down is independent of the applied LF, and might be dictated by the hyperfine energy scale which is  $\approx 0.2\text{K}$ .

The dynamical behavior of a canonical spin glass is expected to move to longer and longer time scales as the temperature is decreased below  $T_g$ . In contrast, Figure 5.7 shows that below  $T \approx 0.2\text{K}$  the fluctuation rate is constant within the accuracy of our measurement. We point out that the dynamical behavior below  $0.2\text{K}$  cannot be ascribed to paramagnetic nuclear moments of the fluorine ions since these moments are 1000 times smaller than the Ho ones and usually nuclear magnetic moments are decoupled in a LF of  $100\text{G}$ , where we still see dynamical relaxation. Another interesting feature is that, even though the slowing down temperature does correspond to that where one would expect to observe  $T_g$  ( $T_c \times 0.25 \approx 0.38\text{K}$  is the interaction strength scale), the temperature at which the system is observed to slow down ( $\approx 0.3\text{K}$ ) seems not to depend on the applied LF up to a field of  $500\text{G}$ .

Before finishing this section it should be noted that we also analyzed our data using the microscopic model proposed by Y. J. Uemura [73] *et al.* which

successfully described ZF and LF data of canonical spin glasses. This model assumes that the spin time correlation of the system is given by:

$$[\langle S(t)S(0) \rangle / \langle [S(0)]^2 \rangle]_{\text{av}} = (1 - Q)e^{-\nu t} + Q \quad (5.3)$$

where  $\langle \ \rangle$  denotes the thermal average of a single spin,  $[ \ ]_{\text{av}}$  denotes the spatial average over the sample spins, and  $Q$  is the spin glass order parameter. If a  $\mu\text{SR}$  experiment is performed in a system with Heisenberg spins which follows the above correlation function, the observed  $\mu\text{SR}$  signal is the product of two Gaussian Kubo-Toyabe functions: a static one which accounts for the frozen component of the spin (with  $\Delta_s = \sqrt{Q}\Delta$ ) and a dynamic one which accounts for the fluctuating spin component (with  $\Delta_d = \sqrt{1-Q}\Delta$ ). Our fits with this function showed that the value of  $\Delta_s$  started growing at 0.3K (which coincides with the slowing down temperature in Figure 5.7). Nevertheless,  $\Delta_d$  was almost temperature independent from base temperature up to 0.6K (in contrast to the two orders of magnitude divergence observed in canonical spin glasses at  $T_g$  [73]). Our LF data indicates that the dynamical behavior of the system does depend in temperature, so it is possible that the insensitivity of this model to the dynamical channel is associated with the function having too many free parameters to describe such a rapidly relaxing signal.

## 5.2 $\text{LiHo}_x\text{Y}_{1-x}\text{F}_4$ for $x \leq 0.12$

The  $\mu\text{SR}$  data from the four most diluted samples ( $x=0.12, 0.08, 0.045$  and  $0.018$ ) are all qualitatively very similar. The ZF and low temperature

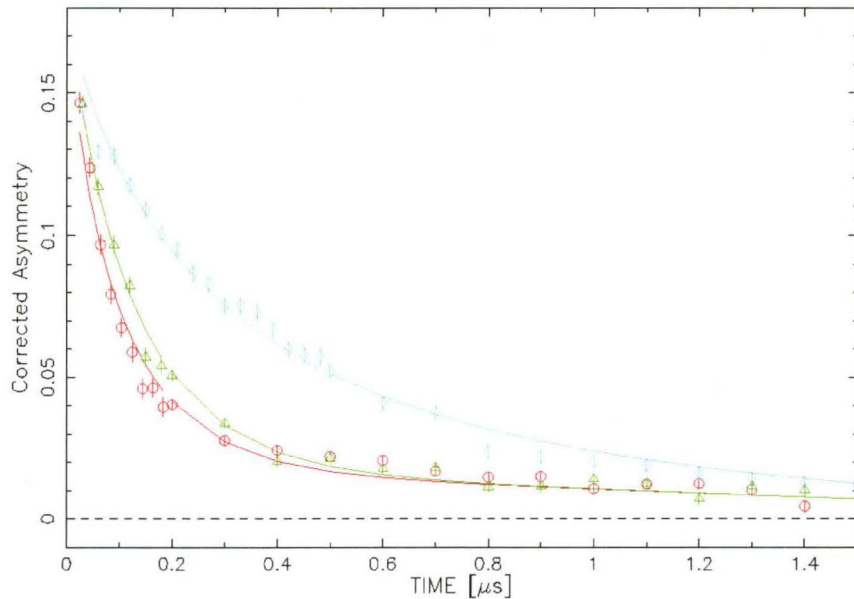


Figure 5.8:  $\mu$ SR signals of the  $x=0.045$  system at 15mK (red circles), 1K (green triangles) and 10K (aqua diamonds) in a LF of 20G. The continuous lines are fits to a power exponential function plus a background.

( $T < 0.5$ K) spectra from all these dopings present a fast exponential-like relaxation of the asymmetry at early times followed by a slower relaxing component (see Figure 5.8). Also, at higher temperature, the relaxation in ZF looks almost single exponential. It is because of these similarities that we present the analysis of all these samples together in a single section.

### 5.2.1 Phenomenological analysis

As mentioned in Chapter 2, models for systems of dipole-coupled Ising spins predict a spin glass ground state to appear when enough random magnetic dilution is introduced. These studies also predict that the spin glass ground

state should prevail up to the highest dilution levels with an ever decreasing  $T_g$ . As in the previous section, we have analyzed the data from the most diluted samples using a power exponential function (Equation 5.1) in order to look for the characteristic features of spin glass behavior in our  $\mu$ SR signals.

The fits were performed with the total asymmetry fixed to the value found at high temperature (typically 10K) and, for the case of the low LF runs, with the background also fixed. The background was found by fitting together two runs (one at low LF and one typically at 100G) with the same fitting parameters except for the relaxation of the background which was set to zero in the high LF run. The size and relaxation rate of the background for the different samples in different beam lines is shown on Table 4.1.

The reduced  $\chi^2$  values from the fits of the low temperature runs taken in the dilution refrigerator at low LF are:  $1.26 \pm 0.24$  for  $x=0.12$ ,  $1.54 \pm 0.34$  for  $x=0.08$ , and  $1.73 \pm 0.48$  for  $x=0.045$ . It can be seen that the fits were better at higher values of  $x$ . Actually the fit of the signals of the  $x=0.018$  system to a power exponential had such a big  $\chi^2$  that we do not present this analysis. As will be seen in the next section, fitting the data to a microscopic model is needed to produce a better outcome.

Figures 5.9 and 5.10 show the fitted parameters from Equation 5.1 in ZF as a function of temperature for different dopings. It can be observed that the relaxation rate of the three samples in Figure 5.10 follow approximately the same trend as that of the  $x=0.25$  sample (Figure 5.4). The increase of  $\lambda$  upon cooling starts at around 20K due to the slowing down of the Ho magnetic moments into the  $\mu$ SR time window. The increase is monotonic down to

$\approx 0.1\text{K}$  after which it seems to become constant. The apparent discontinuity at around  $1\text{K}$  in the  $x=0.12$  and  $0.08$  data on Figure 5.9 is likely an artifact. It is in this region where the high temperature data taken in the helium flow cryostat at the M20 beam line meets the low temperature scan taken in the dilution refrigerator at the M15 beam line. The step could be produced by deviations of our estimated total asymmetry from its actual value (remember that it was not possible to perform a weak transverse field run in this system and therefore we do not know the total asymmetry very accurately). Since the relaxation rates for these systems are high, then a small shift on the asymmetry can produce a noticeable difference between the fitted values of the relaxation rates. Aside from this effect, no sharp features can be observed in the fitted relaxation rate.

Figure 5.10 shows the evolution with temperature of the fitted values of  $\beta$  in Equation 5.1. Upon cooling there is a decrease of the value of  $\beta$  down to approximately  $10\text{K}$  where it reaches a minimum. This minimum, which is reported in the literature [41], is associated with a slowing down of the fast fluctuating Ho moments into the  $\mu\text{SR}$  time window. After this, the value of  $\beta$  increases with decreasing temperature as consequence of a further slowing down. Even though noisy, the parameter  $\beta$  does not show the gradual characteristic reduction to  $1/3$  at  $T_g$  observed in  $\mu\text{SR}$  studies of spin glass systems [89]. Instead it seems to level off below  $0.2\text{K}$ .

The signals taken in low LF were observed to relax to zero down to the lowest temperatures ( $12\text{mK}$  for  $x=0.12$ ,  $15\text{mK}$  for  $0.08$ ,  $20\text{mK}$  for  $0.045$  and  $15\text{mK}$  for  $0.018$ ) giving evidence for dynamic magnetism down to tempera-

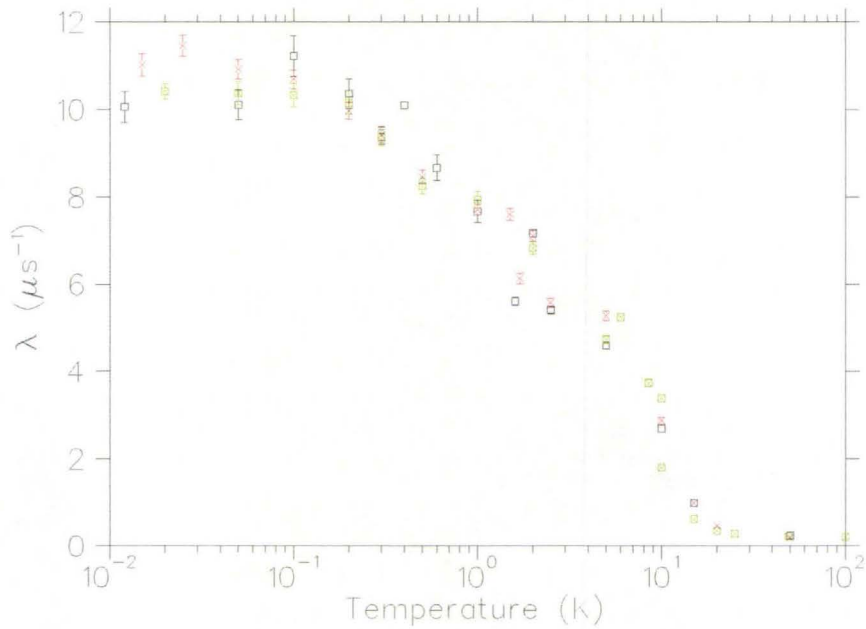


Figure 5.9: Relaxation rate of a power exponential fit as a function of temperature in low LF. Black squares is data from the x=0.12 sample, red crosses from 0.08, and green crossed squares from 0.045.

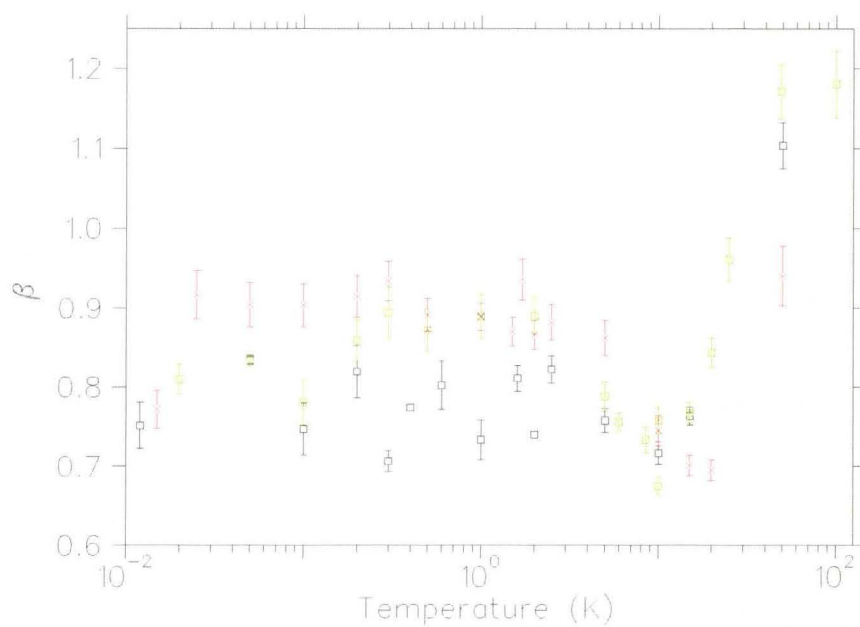


Figure 5.10: Exponent of the power exponential fit as a function of temperature in low LF. Black squares is data from the  $x=0.12$  sample, red crosses from 0.08, and green crossed squares from 0.045.

tures lower than any energy scale of the single ion Hamiltonian, and even lower than the characteristic energy scale of the dipolar interaction between magnetic moments. The dipolar interaction energy scale is the relevant interaction between the Ho moments at high dilutions since most Ho ions do not have a neighbor with which they can interact through the antiferromagnetic exchange interaction (for  $x=0.12$  60% of the Ho ions do not have a nearest neighbor, for  $x=0.08$  is 72%, for  $x=0.045$  is 83%, and for  $x=0.018$  it is 93%). So the interaction energy scale can be estimated from the ferromagnetic  $T_c$  in the absence of exchange interaction. This  $T_c$  has been calculated to be equal to 1.92K [13] and, therefore, the dipolar interaction strength is estimated to be  $1.92x$ . This expression gives a characteristic interaction strength of 230mK for  $x=0.12$ , 154mK for 0.08, 86mK for 0.045 and 34mK for 0.018; again, notice that all these energy scales are higher than the base temperature of our measurements.

Then, we have found that neither the trend of  $\beta$  with temperature, nor the presence of dynamic magnetism at low temperatures (lower than the characteristic interaction strength) are compatible with a spin glass ground state in the most diluted systems. In the following section we apply again the Kubo-Toyabe formalism to analyze our data.

### 5.2.2 Microscopic analysis

In order to obtain quantitative information from our measurements we also analyzed our data using microscopic-model functions. One of the models was the Uemura *et al.* spin glass function which was mentioned at the end of

Section 5.1.2. With this function we fit the 20G LF data of the  $x=0.045$ . The fit parameters did not match the expected trend of spin glass behavior. Specifically, the fit showed the unphysical result that the static component of the spin was nonzero even at temperatures as high as 1K.

Another microscopic model that we used to analyze the data was the one dimensional LKT function which was presented in Section 3.4.3. The decoupling of the background with a low LF motivated us to test the hypothesis of having an almost static magnetic environment at base temperature. We deduced that a static and highly stretched magnetic field distribution perpendicular to the initial muon spin direction would produce a fast decoupling in LF (the decoupling of the signal, if static, should follow Equation 3.25); while also accounting for the fact that the asymmetry relaxes to zero at base temperature in low LF even if the magnetic moments are static. This hypothesis can be valid for  $\text{LiHo}_x\text{Y}_{1-x}\text{F}_4$  since its Ising spins could produce, in principle, an anisotropic field distribution. We decided to approximate this highly stretched field distribution by a one dimensional Lorentzian function (we choose Lorentzian so we could match the exponential-like relaxation of the asymmetry at early times). Fits of the low LF data were satisfactory but the decoupling of the signal under LF at base temperature was much too fast and did not match our observations.

In order to know how stretched along the Ising direction the field distribution is, we performed several overlapping runs on the  $x=0.08$  system but this time implanting the muon with its initial spin along the Ising direction (instead of perpendicular to it as the rest of our measurements). The overlap-

ping runs were taken in the helium flow cryostat at the M20 beam line in three different temperatures at ZF and in 3 different nonzero fields at 2.5K. All the runs showed a slightly smaller relaxation than that observed when the muon was implanted perpendicular to the Ising axis (see Table 5.1). From what was explained in Section 3.4.3, one would expect that if the shape of the magnetic field distribution is constant in temperature and LF, then the ratio between the two relaxation rates should be also constant. Table 5.1 also shows this ratio. It can be seen that the ratio of the relaxation rates agree with each other within error bars, except for that at 500G. The reason for the discrepancy at 500G is not clear to us; it could be produced by a real effect (like the change of the magnetic field distribution upon the application of LF) or it could be an artifact of the fit. If the 500G point is left aside and only the runs at low field are considered one gets an averaged ratio of  $1.36 \pm 0.06$ . One can now use Equation 3.31 to get the ratio  $r$  of the field distribution width along the Ising axis to that perpendicular to it. We note that Equation 3.31 was derived for a field distribution which is the product of Gaussian functions. The  $x=0.08$  system is so magnetically diluted that the Gaussian scenario is no longer valid. Nevertheless notice that the narrowing limit (on which Equation 3.31 is based) of a Lorentzian case differs from that of the Gaussian only by the power of the exponential while the dependence of the relaxation on the field distribution width and fluctuation rate is the same. Since we fitted our signals to a power exponential function we will assume that we can use Equation 3.31 to estimate how stretched is the field distribution in the  $x=0.08$  sample. The input for this formula is the above mentioned ratio of relaxations perpendicular and parallel to the Ising axis, and one gets  $r=1.31 \pm 0.05$ . This means that the field

Run	$\lambda_x$ ( $\mu s^{-1}$ )	$\lambda_{yz}$ ( $\mu s^{-1}$ )	$\lambda_x/\lambda_{yz}$
ZF 1.7K	$7.81 \pm 0.59$	$5.38 \pm 0.39$	$1.45 \pm 0.21$
ZF 2.5K	$8.11 \pm 0.74$	$6.14 \pm 0.58$	$1.32 \pm 0.25$
ZF 10K	$3.50 \pm 0.24$	$2.62 \pm 0.18$	$1.34 \pm 0.18$
100G 2.5K	$7.59 \pm 0.18$	$5.84 \pm 0.16$	$1.30 \pm 0.07$
200G 2.5K	$7.16 \pm 0.18$	$5.19 \pm 0.17$	$1.38 \pm 0.08$
500G 2.5K	$3.69 \pm 0.13$	$3.42 \pm 0.12$	$1.08 \pm 0.08$

Table 5.1: Relaxation rate of the  $\mu$ SR signal parallel ( $\lambda_{yz}$ ) and perpendicular ( $\lambda_x$ ) to the Ising axis of the system.

distribution width along the Ising direction is approximately 30% bigger than that perpendicular to it.

We also analyzed our data using a standard dynamical LKT model. This is one of the simplest microscopic models which can be applied and, as we will shown now, it is able to describe qualitatively the behavior of the signals.

It was noticed while fitting the data with the LKT function that the “msrfit” program produced inconsistent results when the fluctuation rate  $\nu$  was bigger than the parameter  $a$  (see Equation 3.13). This problem is most probably due to the parameters of the fit getting out of the range of the numerical table. To solve this problem we calculated an extended “msrfit” numerical table of the LKT function which included all the parameter space in which we were interested. To do this we improved the Monte Carlo algorithm that was used to build the one dimensional LKT table. One of the improvements consisted in adding GKT functions instead as tracking the evolution of the

muons one by one. In order to do this the new algorithm calculated the the GKT function at discrete values of time, and then used nonlinear interpolation to obtain values in between these points. An other improvement of the algorithm consisted in accounting exactly for the long tail of the distribution on Equation 3.13 (this was achieved by splitting the distribution in two parts, one for  $\Delta < 10a$  which was simulated by Monte Carlo methods, and an other for  $\Delta > 10a$  which was simulated by generating a random numbers and projecting them in such a way that the final distribution of numbers was that of the tail of the distribution). This new algorithm converged faster, reduced the noise in the simulated signal, and produced accurate functions at long times.

The analysis with the LKT model was applied only to the low temperature sets of data taken in the dilution refrigerator. The fit function was the addition of a LKT function plus a Gaussian background when fitting low LF data. The total asymmetry of the LKT function was fixed to the value found from the power exponential fit at high temperature. The field distribution width  $a$  was determined from letting this parameter free in a common fit of a low LF run at base temperature together with an other at 100G with the same temperature (except for the  $x=0.02$  system where  $a$  was determined only from fitting the run at base temperature and low LF). Then, the  $a$  parameter was kept fixed in every fit of a given sample.

Table 5.2 shows typical  $\chi^2$  values for the fits in low LF, and Figure 5.11 plots one of these fits at early times for a run of the  $x=0.045$  sample at 20mK. The reduced  $\chi^2$  are not optimal. Specifically, the  $\chi^2$  values increased with temperature causing the average and standard deviation to increase. We be-

lieve that the main contribution to these reduced  $\chi^2$  values is the deviation of the internal field distribution from the spherical-Lorentzian one assumed by the model. For instance, and from what we have said above, we know that the internal field distribution is about 30% elongated in the Ising direction and also, by symmetry, it is possible that this distribution is a function of the azimuthal angle (four fold around the crystallographic Ising direction). Another difference between the internal field distribution and that of the LKT model is that this last one overestimates the fraction of muons which feel very high internal fields. That this might be at play is observed in Figure 5.11. The inset of this figure shows that, in order for the Lorentzian asymmetry to follow the right decay at long times it has to have a faster relaxation at early times. This faster exponential relaxation of the LKT is known to be produced by an excess of high field sites in the Lorentzian field distribution, and it is very similar to the trend that can be observed in the main part of Figure 5.11. Regardless of these problems, as we present the results of the analysis it will be shown that a stochastic microscopic theory (like the of the LKT model) does capture all the main features of the observed signals.

Figure 5.12 shows the fitted values of  $a$  as a function of doping. The continuous line in this plot is a fit to a square root trend which is expected at high dilution (see appendix A). The square root behavior is roughly followed by the data and deviations can be due to systematic error introduced by a different shape of the internal field distribution (as mentioned in the previous paragraph) and to the uncertainty on determining the total asymmetry of the  $\mu$ SR signals.

x	Reduced $\chi^2$
0.12	1.29±0.22
0.08	2.67±1.2
0.045	2.02±0.6
0.018	2.64±1.03
	1.39±0.03

Table 5.2: Typical reduced  $\chi^2$  values for the fits of the low LF data for the samples with  $x \leq 0.12$ . The typical values are the average of the set of reduced  $\chi^2$  while the error its standard deviation. The two values of the  $x=0.018$  sample correspond to two different sets of data taken at different beam times.

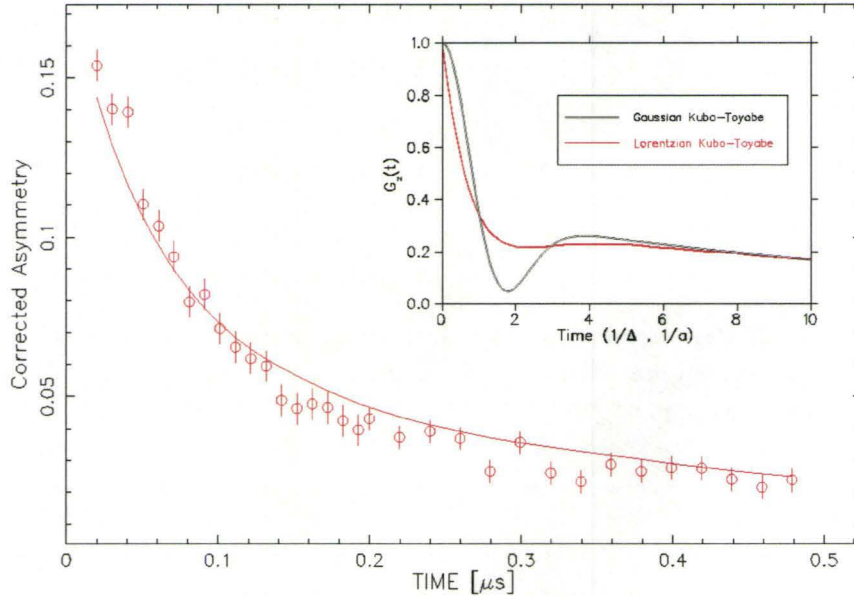


Figure 5.11: Corrected asymmetry for the  $x=0.045$  sample in a LF of 20G at 20mK. The continuous line is a fit using a Lorentzian Kubo-Toyabe function. Inset: Gaussian and Lorentzian Kubo-Toyabe functions with both values of  $\nu/\Delta$  and  $\nu/a$  equal to 0.1

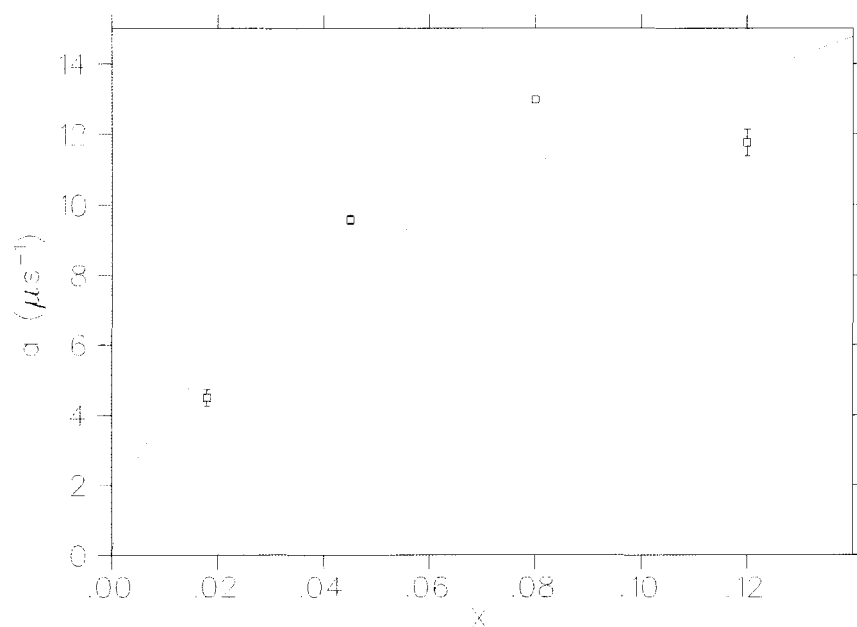


Figure 5.12: Parameter  $a$  from the Lorentzian Kubo-Toyabe theory as a function of  $x$ , for samples with  $x \leq 0.12$ . The continuous line is a fit to of the data to the expected square root trend.

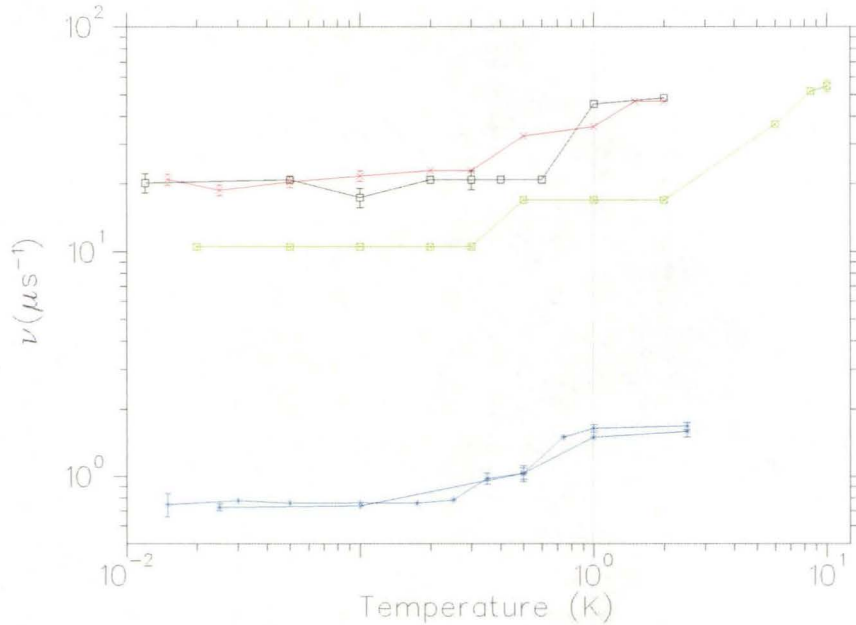


Figure 5.13: Fluctuation rate of the internal magnetic field at the muon site as a function of temperature for  $x=0.12$  (black squares),  $0.08$  (red crosses),  $0.045$  (green cross squares) and  $0.018$  (blue crosses). The two lines of the  $0.018$  system correspond to two sets of data taken at different beam times. The dots are connected by straight lines for clarity.

The fluctuation rate as a function of temperature is shown in Figure 5.13. One important finding from our measurements is that the fluctuation rate is constant and nonzero at low temperature. Also, this low temperature fluctuation rate is a function of the  $H_0$  concentration  $x$ . The low temperature fluctuation rate is plotted in Figure 5.14 as a function of doping level. The fluctuation rate was observed to increase from its low temperature (constant) value at  $T \approx 1\text{K}$  for  $x=0.12$ ;  $T \approx 0.5\text{K}$  for  $x=0.08$ ;  $T \approx 0.5\text{K}$  for  $x=0.045$ ; and  $T \approx 0.35\text{K}$  for  $x=0.018$ .

When fitting higher LF data of the  $x=0.12$  and  $0.045$  systems at base temperature (the LF scan for  $x=0.08$  was carried up to  $100\text{G}$  only) we noticed

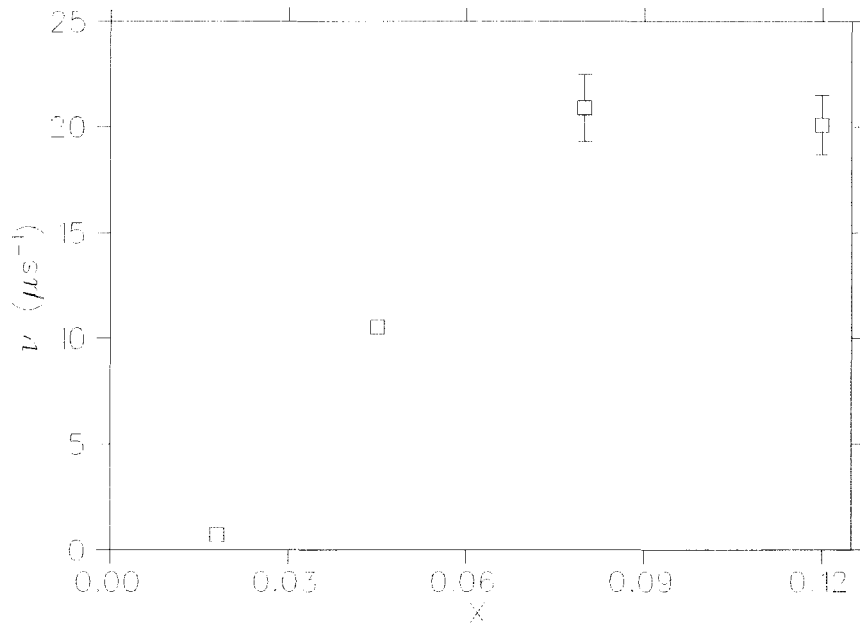


Figure 5.14: Low temperature ( $T \approx 15\text{mK}$ ) fluctuation rate of the internal magnetic field at the muon site as a function of Ho concentration  $x$ .

that the low LF fitted parameters could nicely reproduce the observed signal just by increasing the LF in the Kubo-Toyabe model. Figure 5.15 show a LF scan for the  $x=0.12$  sample at base temperature. The lowest two runs (red circles and green triangles) were fit together to obtain values for  $a$  and  $\nu$ . In the following three runs at higher LF (aqua diamonds, magenta stars and orange X) all the parameters of the fit were held constant except  $\alpha$  ( $\alpha$  has to be free since we know that this parameter is a function of LF, see Section 3.1). Notice that the same set of parameters could nicely predict the LF behavior of the signal up to 0.1T. At higher fields (black crosses and blue skewed-squares) the fluctuation rate had to be left free in order to be able to follow the time evolution of the signal. The fitted values of  $\nu$  at high LF were higher than that at base and the trend can be seen in Figure 5.16. We recall that theoretical

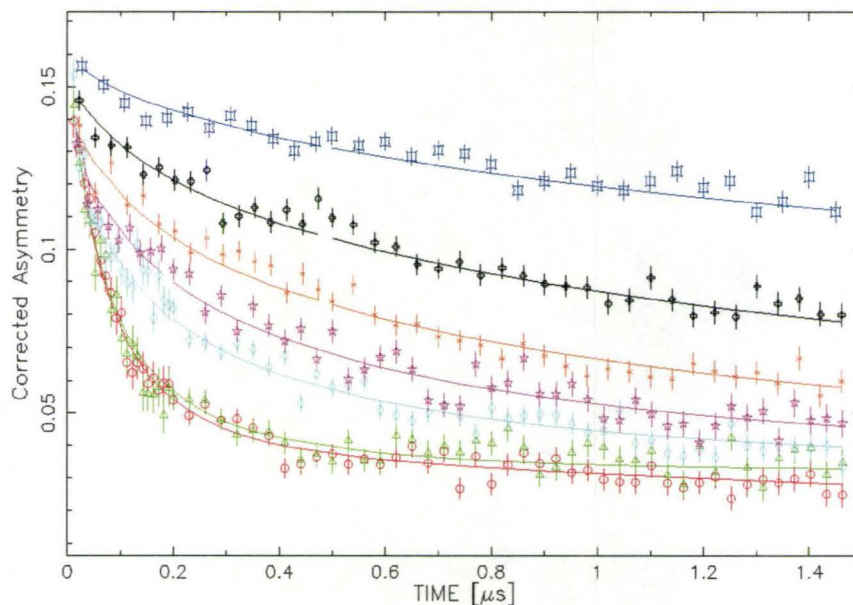


Figure 5.15: Corrected asymmetry for a LF scan at  $T=12\text{mK}$  in the  $x=0.12$  system: ZF (red circles),  $0.01\text{T}$  (green triangles),  $0.05\text{T}$  (aqua diamonds),  $0.07\text{T}$  (magenta stars),  $0.1\text{T}$  (orange X),  $0.2\text{T}$  (black crosses), and  $0.4\text{T}$  (blue skewed-squares).

studies already predicted fluctuations between the Ising levels of the single Ho ion starting (and increasing) at  $\sim 0.2\text{T}$  [45]. For the case of  $x=0.045$  we found that the low LF fitted parameters of the LKT model could nicely reproduce all the LF data up to  $0.2\text{T}$ .

Figure 5.17 shows an LF scan of the  $x=0.018$  system at  $25\text{mK}$ . The continuous lines in these fits are again fits where only  $\alpha$  was allowed to vary and the amplitude,  $a$  and  $\nu$  were fixed to the value found in a run at  $5\text{G}$  LF and  $15\text{mK}$ . It can be seen that the LKT function does not closely follow the evolution of the signal at long times when the LF is at an intermediate range. This effect is probably due also to the shape of the real internal field distribution not

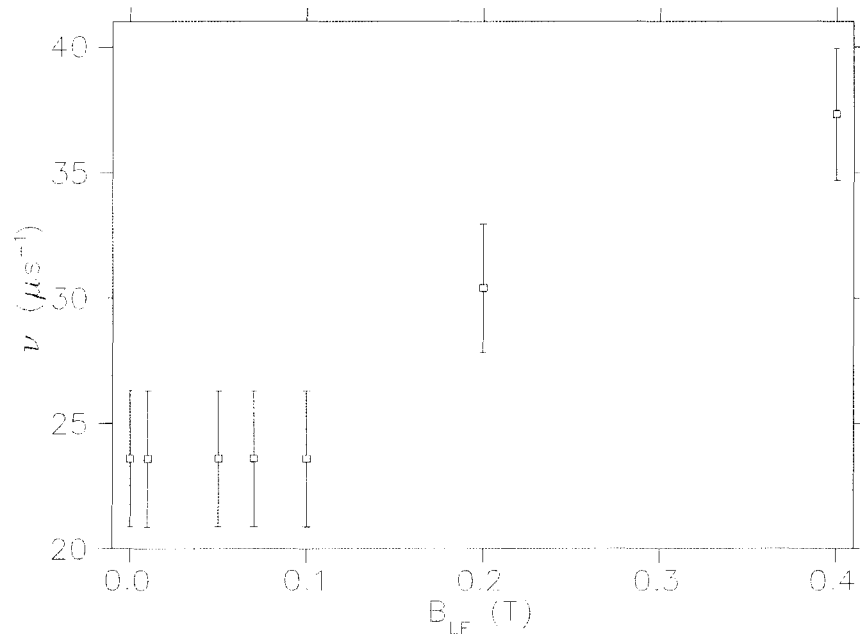


Figure 5.16: Fluctuation rate of the internal magnetic field as a function of LF at 12mK for the  $x=0.12$  sample. The values at 0.05T, 0.07T and 0.1T are fixed to those found in the common fit of the ZF and 0.01T runs. It is because of this that the low field points have the exact same value and error bars.

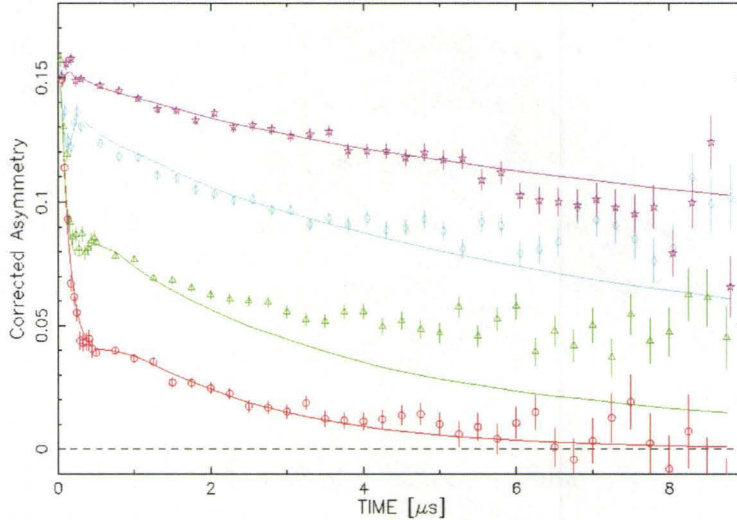


Figure 5.17: Corrected asymmetry for a LF scan at 25mK for  $x=0.018$ : 0.001T (red circles), 0.01T (green triangles), 0.025T (aqua diamonds), and 0.05T (magenta stars).

being a spherically symmetric Lorentzian as we discussed before. The shape of the internal field distribution has a big impact on how the (static) tail of the polarization function is decoupled. If the fluctuation rate is low, as we have shown is the case for the  $x=0.018$  system, the tail of the function will tend to relax almost from its constant value and, therefore, if this value is wrongly estimated by the fit function, the whole long time relaxation will be offset. This is not longer a problem at high fields since the position of the static tail is almost the same regardless of the shape of the internal field distribution, as we can see in this case.

Now we can point out the reason why the low LF data of the  $x=0.018$  system could not be fit to a power exponential function. Figure 5.17 shows that the fluctuation rate at base temperature has decreased so much at this

doping that a shoulder at around  $1\mu\text{s}$  can be observed and a power exponential function cannot fit this type of behavior (note that in the measurements of this doping we did not observe a background signal in low LF, see Table 4.1). On the other hand, this type of shoulders are predicted by stochastic models like the LKT and they happen when the fluctuation rate of the internal magnetic field is small enough such that the dynamical effects appear until the function is close to its static minimum (see Figure 3.8).

We would like to point out another feature of our low temperature data which is nicely accounted by the LKT model. At high fluctuation rates the Kubo-Toyabe formalism predicts the observation of the narrowing effect, regardless of the shape of the internal field distribution. This effect is observed in our data in Figure 5.8 for the  $x=0.045$  system. This figure shows that as the temperature increases the overall relaxation rate of the signal decreases. Then, the decrease in relaxation rate of the signal can be interpreted with the Kubo-Toyabe formalism as an increase of the already large fluctuation rate of the internal field with temperature. For the  $x=0.018$  system, where the fluctuation rate at base temperature is small, the Kubo-Toyabe model would expect that the long time tail relaxes faster as the fluctuation rate is increased. This is indeed what happens in the  $x=0.018$  system as can be seen in Figure 5.18. This figure shows that as temperature is increased the signal relaxes faster at long times due to an increase of the low fluctuation rate. At the same time, the fast relaxing front end at early times is not affected by the increase in the fluctuation rate since, as expected from the LKT model, its shape is only determined by  $a$  when  $a > \nu$ .

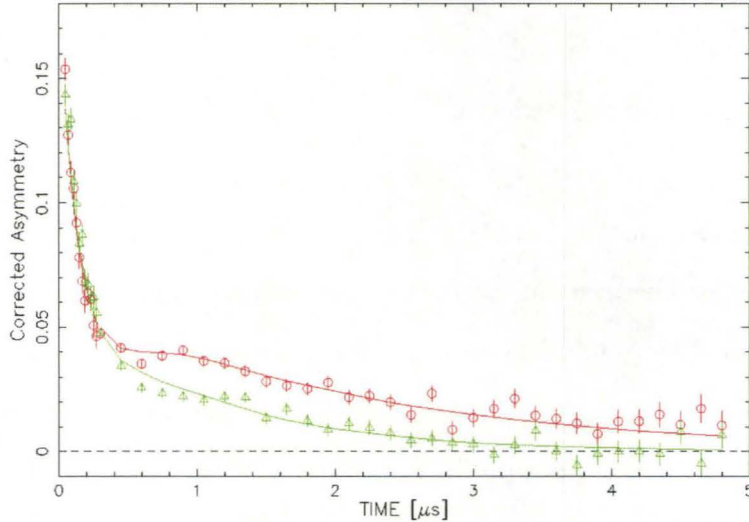


Figure 5.18: Corrected asymmetry for the  $x=0.018$  system at 25mK (red circles) and at 2.5K (green triangles) in a LF of 10G

Based on what has been discussed before, we would like to restate that the qualitative behavior of our most diluted samples is well accounted by a stochastic Kubo-Toyabe picture both in ZF and LF; and that, therefore, the fitted values of  $\nu$  are reliable and track the dynamical behavior of the systems as a function of temperature and doping. Discussion about the results of the analysis of our data will be presented in the following chapter.

### 5.3 Overview

We have found that the  $\mu$ SR signals from our  $x \leq 0.25$  systems has the same qualitative behavior. As in the case of the ferromagnetic samples, we observed F- $\mu$ -F bond formation at high temperature, and the  $\text{Ho}_{3+}$  slowing down into the  $\mu$ SR time window at approximately 20K. We have not observed

any signature for a spin glass transition in any of the samples. In particular, fits to a power exponential function of our low LF data (0-20G), did not show the characteristic reduction of  $\beta$  to  $1/3$  at  $T_g$ , and the signals were observed to relax to zero down to base temperature (down to temperatures which are much smaller than the characteristic interaction strength of any of the samples studied) giving evidence for dynamic magnetism. Further more, the data for the  $x=0.018$  system could not even be satisfactorily described by a power exponential function. Also, a fit of the data using the Uemura spin glass function, did not produced sensible results. Instead it was observed that the Kubo-Toyabe stochastic functions could give a reasonable account for our data. This analysis showed that the  $\text{Ho}^{3+}$  ions slowdown upon cooling down to a temperature  $T^*$  which is approximately 0.2K, but which is possible that has some dependence on  $x$ . Below this temperature the characteristic fluctuation rate of the moments is observed to be constant and  $x$  dependent (decreasing with  $x$ ). From analyzing signals from the  $x=0.08$  system in ZF and LF at high temperature (2.5K and 5K), we found evidence for the internal field distribution at the muon site to be 30% longer along the Ising direction. We believe that including this stretching of the internal field distribution in a Kubo-Toyabe like model would produce a better account of our data, specially for the  $x=0.018$  system.

# Chapter 6

## Discussion

### 6.1 F- $\mu$ -F

The F- $\mu$ -F fitting function that we used to analyze our data is the one corrected for the bond symmetry found in  $\text{LiHo}_x\text{Y}_{1-x}\text{F}_4$  (see Equation 3.40). We compared the quality of the fit using this corrected function to other fits using the up to now standard cubic one [78] [79] (care was taken to use the same number of fitting parameters and degrees of freedom in both fits). The averaged value of  $\chi^2$  for the fitted runs are shown in Table 6.1 as a function of doping. It can be seen that the corrected function produced averaged  $\chi^2$  values which are closer to 1, furthermore, all the values of  $\chi^2$  from the individual runs were systematically closer to 1 when using the corrected fitting function. Still the values of  $\chi^2$  are not optimal. We believe that further tuning of the fitting function could be performed (see Section 6.5).

As was mentioned in Chapter 3, when the positive muon forms an F- $\mu$ -F center it pulls the negative fluorine ions together, displacing them from their crystallographic positions. This rises the question of how much is the

x	$\chi^2_{\text{corrected}}$	$\chi^2_{\text{cubic}}$
0.08	1.87	2.03
0.045	1.67	1.74
0.018	1.85	2.86

Table 6.1: Average value of  $\chi^2$  obtained from fitting the F- $\mu$ -F signals (for T>20K) with a fitting function corrected for the right symmetry of the bond, and with the standard cubic-environment function used in the literature.

muon going to affect the crystal field levels of the nearest Ho ions through a polarization of the nearby crystal environment. The F- $\mu$ -F bond length in  $\text{LiHo}_x\text{Y}_{1-x}\text{F}_4$  is 7.6% smaller than the unperturbed distance between nearest neighbors  $\text{F}^-$  ions (2.602Å, for details on the crystallographic structure of  $\text{LiYF}_4$  see Reference [91]). That is, the fluorine ions are displaced about 0.1Å from their equilibrium position towards each other. This displacement seems small and, naively speaking, its effect on the crystal field levels of the Ho ion should be accordingly small. We believe that the biggest contribution to the crystal field distortion at the Ho site would come mostly from the presence of the muon charge itself and not so much from the polarization of the lattice. There are a few reported systems where the muon charge is thought to affect the crystal field level structure of the nearby magnetic ions ( $\text{PrNi}_5$  [92] [93] [94],  $\text{PrIn}_3$  [95],  $\text{UNi}_2\text{Al}_2$  [96] and  $\text{TmNi}_2\text{B}_2\text{C}$  [97]). Generally speaking, the muon electric field would tend to align the Ho magnetic moment perpendicular to the line connecting them [98], but an exact crystal field calculation is needed for a quantitative estimation. Nevertheless it should be noted that, regardless of whether the muon electric field affects the crystal field levels of the near Ho

ions or not, our  $\mu$ SR measurements have shown themselves to be sensitive to the bulk magnetic phenomena. This is evidenced by the oscillating asymmetry in the  $x=1$  and 0.45 systems which sets in as the samples are cooled into the ferromagnetic regime (see Figures 4.8 and 4.14) and which track the order parameter as measured by optical spectroscopy (Figure 4.9). Furthermore, the effect of the muon on the Ho ions would be expected to decrease as  $x$  is decreased since, on average, the Ho moments are further from the muon.

## 6.2 Ferromagnetism

Inside the ferromagnetic state our low LF measurements indicate that the internal field distribution in both ferromagnetic systems is broad. This can be seen from the fact that, as Table 4.2 shows, the spontaneous precession frequency ( $f_{\text{ferro}}$ , which is approximately the average field magnitude) is the same size as the relaxation rate of the signal ( $\lambda_{\text{ferro}}$ , which is approximately the width of the field distribution). At a high LF the internal field distribution seems to be even broader with a typical width along the muon spin direction of order of 0.67T ( $90\mu\text{s}^{-1}$ ) for  $x=0.45$  (Figure 4.16). The most likely source for the broadening of the internal field is the splitting of the sample into magnetic domains. If this is the case, and since the muon probes the system in a scale ( $\sim 1\text{\AA}$ ) that is shorter than the typical size of the magnetic domains ( $5\mu\text{m}$  [85]), the magnetic field distribution at the Ho ions can also be broadened (only along the  $\hat{c}$  axis due to the Ising nature of the spins in Zero Field (ZF)). Then, it might not be appropriate for theoretical calculations to account for the magnetic domain structure assuming that the Ho ion is “deep”

inside a domain [15], since this assumption might not apply for most Ho ions. The effect of the magnetic domain structure on the microscopic physics has already been pointed out as a possible source of quantitative disagreement between calculations and experiment [13] [17]; and recently it has been shown that taking into account the magnetic domain shape in the calculations, can produce quantitative agreement in the  $x=1$  system [49].

The  $x=0.45$  system was expected to have a reentrant transition into a ferroglass state [27]. We did not find any feature in our fitted parameters that might indicate this transition, furthermore, the behavior of the signal was qualitatively the same as that of the  $x=1$  system as we have already mentioned. Nevertheless it is possible that we have had missed the ferroglass behavior altogether because the signature for glassy physics lies in the dynamical behavior of the system, to which low LF measurements are not always very sensitive. Field scans are needed to study the dynamics of magnetic moments, but the only field scans that we performed in our ferromagnetic samples were at base temperature (50mK for  $x=1$  and 15mK for  $x=0.45$ ). These LF scans (from 1T to 4T) showed that the magnetic moments in both of our samples were already static at these temperatures and, therefore, indicated the absence of low lying excitations (muon Zeeman splitting is  $0.56\mu\text{eV}/\text{T}$ ). This is expected for the  $x=1$  system, where excitations are gaped even at the critical field [18] [17], and for the  $x=0.45$  this might indicate that we are much colder than  $T_g$  for the given field. As a matter of fact  $\chi_{AC}$  measurements have shown that  $T_g$  at 1T is  $\approx 250\text{mK}$  in  $x=0.44$  [27] which is 16 times higher than the temperature of our field scan.

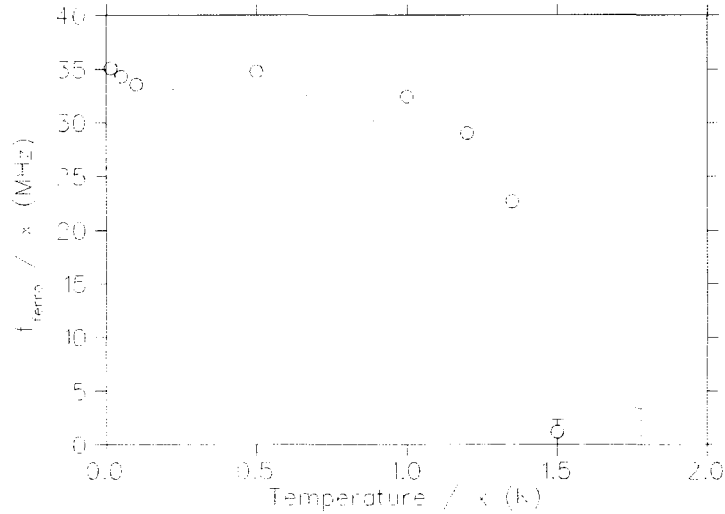


Figure 6.1: Precession frequency of the muon ensemble in ZF divided by the doping level as a function of  $T/x$ . Black circles is data from the  $x=1$  ( $T_c=1.53\text{K}$ ) system while the blue diamonds are from  $x=0.45$ . The highest temperature point for each sample is not a fitted value; it represents the range of frequencies that cannot be fitted due to the fast relaxation of the asymmetry.

In order to investigate if the order parameter follows a mean field behavior with dilution ( $M \propto f_{\text{ferro}} \Rightarrow M(x, T) = xM(1, xT)$ ) we re-plot in Figure 6.1 the data from Figure 4.9 scaled by  $1/x$ . It can be seen that the relation holds well at low temperatures, except for the kink around  $(T/0.45)=0.45\text{K}$ . The origin of this kink, which occurred at  $0.2\text{K}$  and is shifted to  $0.5\text{K}$  in Figure 4.9 due to the scaling by  $x$ , was discussed in Section 4.4 and it might be produced by a trade off between fitting parameters at the hyperfine energy scale. The different temperature dependence of the two order parameters at higher temperature was discussed in Section 4.5, and it could be due to random internal fields which are proportional to the order parameter (see Figure 4.19).

## 6.3 The disordered phase

Our  $\mu$ SR measurements show that, once ferromagnetism is destroyed with dilution, there is qualitatively no change in the magnetic behavior of the system as it is further diluted. That is, we see no feature which signals the onset of an “anti-glass” phase. The absence of an “anti-glass” phase is in agreement with some experimental data ( $\chi_{AC}$  [32] [36] and specific heat [37]) and most theoretical calculations (the only theoretical calculation which supports the “anti-glass” observations is shown in Reference [39]). Also, the analysis of the signals using power exponential functions showed that none of the characteristic signatures of spin glass behavior is present in the  $x=0.25, 0.12, 0.08$  and  $0.045$  systems; in agreement with some AC susceptibility measurements [32]. Furthermore, this analysis showed that in low LF and below approximately  $0.3\text{K}$ , the relaxation functions are temperature independent (see Figures 5.4, 5.5, 5.9 and 5.10).

The  $\mu$ SR signals from the diluted samples seem to be well described by the Kubo-Toyabe theory. This analysis supports the microscopic picture of a paramagnetic system where the magnetic moments fluctuate slower as temperature is decreased. It was observed that below a temperature which we will call  $T^*$ , the fluctuation rate becomes constant within the  $\mu$ SR time window down to base temperature ( $15$  to  $20\text{mK}$ ). It is possible that the peak in the  $\chi_{AC}$  susceptibility data, which has been interpreted as an onset of spin glass physics, is associated with the slowing down at  $T^*$ .

Our measurements also show that the dynamic behavior of the magnetic moments in diluted  $\text{LiHo}_x\text{Y}_{1-x}\text{F}_4$  is broader than what was expected from  $\chi_{AC}$

measurements \* [99]. We would like to point out that we do not believe that the observed fluctuations of the Ho moments are muon induced. The reason for this is the following: if the Ho distribution is assumed to be a continuum, then we would expect that the muon induced fluctuations would go approximately as<sup>†</sup>  $x^{2/3}$ ; and experimentally we do not see a continuous evolution of  $\nu$  with  $x$ , but a rather sharp feature between  $x=0.045$  and  $0.08$  (see Figure 5.14).

It is not possible to determine accurately the dependence of  $T^*$ , the slowing down temperature, on  $x$  from our data (see Figures 5.7 and 5.13). Nevertheless, the size of the temperature-independent fluctuation rate does have a clear dependence on  $x$  (see Figure 5.14). In order to understand this dependency notice that that a transition from an interaction-dominated picture to a single-ion-dominated one as a function of  $x$  would occur at the point given by:  $0.2\text{K} = x \times 1.92\text{K}$  (see footnote on Page 55). This is the point where the hyperfine interaction (which is the smallest energy scale of the single ion part of the Hamiltonian) is equal to the dipolar energy strength. This gives a value of  $x \approx 0.1$  for the transition region. Then, it is possible that the increase of  $\nu$  with  $x$  in Figure 5.14 is associated with the transition from a single ion dominated

---

\* With exception of the susceptibility measurements reported in Reference [24] where they report that  $\chi''$  becomes frequency independent at high frequencies and below  $T_g$ , but this result has not been reproduced by any other group.

† As mentioned in the footnote on Page 55, in the diluted limit the average distance between Ho ions will scale as  $x^{-1/3}$ . It would also be expected that, in average, the distance of the muon to the Ho would scale in the same way (inverse of the Ho density). Then the characteristic potential energy at the Ho ion produced by the muon presence would go as  $x^{1/3}$ . Then, from Fermi golden rule, the characteristic perturbation would go as  $x^{2/3}$

scenario to an interaction dominated one. After all, the hyperfine interactions have been shown to protect the system against fluctuations between the Ising levels of the system [47]; so it could be possible that the hyperfine term produces a reduction in the fluctuation rate of the moments in the diluted regime when it becomes bigger than the interactions.

The persistent low temperature fluctuations in  $\text{LiHo}_x\text{Y}_{1-x}\text{F}_4$  recall the magnetic behavior of the cooperative paramagnet  $\text{Tb}_2\text{Ti}_2\text{O}_7$  [100] [101]. This system is also an insulator with the magnetic moments having an Ising character, but here the main ingredient of the cooperative paramagnetism is the frustration of the antiferromagnetic interactions introduced by the lattice structure. In diluted  $\text{LiHo}_x\text{Y}_{1-x}\text{F}_4$  we expect to observe frustration as well (introduced by the dipolar interactions) but also there is a substantial inherent random component. It is for this reason that, in analogy to the Sherrington-Kirkpatrick model (see Section 1.3), it would be expected that  $\text{LiHo}_x\text{Y}_{1-x}\text{F}_4$  had a spin glass ground state instead of a cooperative paramagnetic-like one. In this sense, the observation of temperature-independent fluctuations in diluted  $\text{LiHo}_x\text{Y}_{1-x}\text{F}_4$  is as surprising as the observation of spin glass features in frustrated magnets without apparent source or randomness (*e.g.*  $\text{Tb}_2\text{Mo}_2\text{O}_7$  [102] [103] and  $\text{Y}_2\text{Mo}_2\text{O}_7$  [104] [103]).

It is useful to compare  $\text{LiHo}_x\text{Y}_{1-x}\text{F}_4$  with other systems which exhibit temperature independent dynamic behavior. One of these materials is the frustrated system  $\text{SrCr}_{9x}\text{Ga}_{12-9x}\text{O}_{19}$ . This material has Heisenberg spins ( $S=3/2$ ) in a Kagome lattice, and the interaction between nearest neighbor spins is antiferromagnetic. In analogy with  $\text{LiHo}_x\text{Y}_{1-x}\text{F}_4$ , randomly diluted specimens of

this system display temperature independent fluctuations inside the  $\mu$ SR time window [105] [106] (with a fluctuation rate which seems to be proportional to  $x^3$  [107]). But, in contrast to what we observe in our system, SCGO show spin glass features in the  $\mu$ SR signals [105] [107] above a certain dilution level, which is close to the percolation point of the Kagome lattice.

Whether the random Ising model with dipolar interactions has a spin glass ground state or if it remains paramagnetic, is still a theoretical debate [50] [38] [53] [61]. Our measurements though seem to support the second option. Nevertheless, and regardless of the outcome of this very interesting debate, we believe that any Ising model which will attempt to describe quantitatively the observed dynamical behavior of  $\text{LiHo}_x\text{Y}_{1-x}\text{F}_4$ , will have to include the hyperfine interaction as a main part of the Hamiltonian (as our interpretation of Figure 5.14 suggest, as well as the theoretical calculations in Reference [47]).

## 6.4 Conclusions

In this section we present an overview of our most important results.

We have developed an F- $\mu$ -F fitting function which takes into account the symmetry of the bonds inside this non-cubic material. This function produced systematically better fits than those produced using the standard “cubic” one.

In the  $x=1$  and 0.45 systems we observed a static ferromagnetic ground state. Our measurements show that the internal field distribution at the muon site is quite broad possibly due to magnetic domain formation. It is likely that the Ho ions also feel a broad internal field distribution even for  $x=1$ . As we

mentioned in Section 6.2, adding this internal random field distribution to the Hamiltonian could possibly solve the long standing question about the steep increase of the  $H$ - $T$  phase diagram at very low fields [13].

Upon the increase of dilution we observed that the ferromagnetic order is destroyed. In particular, the  $x=0.25$  system was observed to have a disordered ground state down to 20mK. This system has not been studied before and was expected to lie in the boundary of the ferromagnetic phase on the  $x$ - $T$  phase diagram. The disordered samples ( $x=0.25, 0.12, 0.08, 0.045$  and  $0.018$ ) show qualitatively the same magnetic behavior and, therefore, we do not see any difference between the “spin glass” part of the  $x$ - $T$  phase diagram and that of the “anti-glass”. The behavior of the  $\mu$ SR signals do not show any of the standard features of spin glass behavior. Instead, they show fluctuating moments which slow down with temperature down to a temperature  $T^*$ ; and below this temperature the fluctuation rate is constant. Then, the ground state behavior of the non-ferromagnetic samples resembles more that of a cooperative paramagnet instead of that of a spin glass. These observations at high dilution allow us to propose a new  $x$ - $T$  phase diagram which is shown in Figure 6.2

The low temperature fluctuation rates have a dependence on  $x$  which might arise due to the hyperfine term becoming stronger than the characteristic strength of the dipolar interaction at these doping (see Figure 5.14). We also find evidence for an increase of the fluctuation rate with transverse magnetic field above 0.1T in the  $x=0.08$  system.

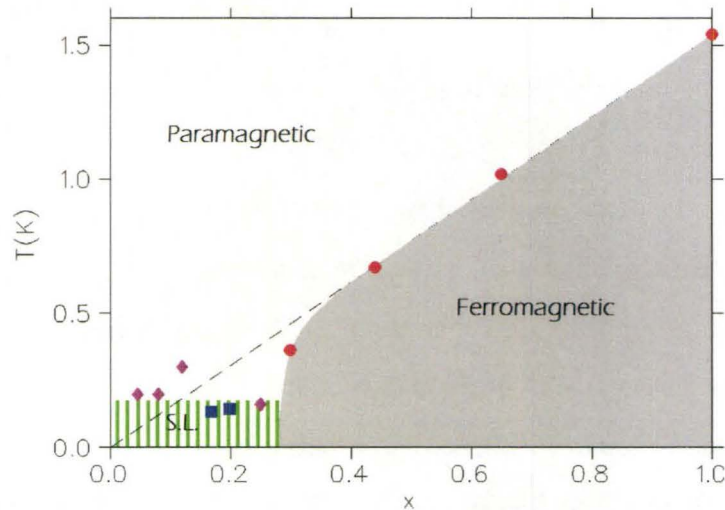


Figure 6.2:  $x$ - $T$  phase diagram. Red circles were measured by magnetization and neutron scattering data [20]; and blue squares from  $\chi_{AC}$  data [22]. The purple diamonds signal the temperature where we observed the onset of a temperature independent  $\mu$ SR signal (Figures 5.4, 5.5, 5.9 and 5.10).

## 6.5 Further work

In this last section we would like to propose further experimental measurements and numerical calculations which would round the main results presented in this thesis, and which would clarify further unknowns.

The next step for improving the F- $\mu$ -F fitting function is to include (most probably through numerical tables) a background distribution of magnetic fields with fluctuations treated within the strong collision model. The smaller fluorine-fluorine interaction could be easily included in this function. The inclusion of a background field distribution has been shown to account for a small frequency shift as the relaxation produced by the background increase [41], which suggest that the new fitting function could correct for the small deviation of  $f_{F\mu F}$  that we observed at low temperatures (see Figure 4.6).

As mentioned before, a muon-induced distortion of the Ho crystal field levels seems unlikely. Nevertheless this point needs still to be proved. Temperature scans in Transverse Field (TF) should be taken in the  $x=0.45$  sample just above  $T_c$  with the field along and perpendicular to the Ising axis. The observed Knight shifts should then be compared to magnetization measurements along the same directions (and in the same transverse field) in order to look for discrepancies in the temperature behavior of the susceptibility (as it was done in Reference [92]). The choice of the  $x=0.45$  sample is suggested so most muons have at least one Ho neighbor, and also because the lower  $T_c$  gives a bigger temperature window for the paramagnetic state at temperatures where the higher crystal field level (at approximately 10K above the ground state doublet) is completely depopulated. Aside from these measurements, a numerical calculation of the perturbation of the crystal field levels should be carried out. Notice that the point charge model might not be useful to calculate the perturbation of the crystal field levels exactly, but nevertheless it can give an order of magnitude for it [92]. Also this calculation would have to include the hyperfine interaction of the Ho ions and, possibly, nuclear quadrupolar interactions of the Ho nucleus with the gradient of the muon electric field.

The origin of the background term can be investigated by making TF scans in the  $x=1$  system above and below  $T_c$ . This would point out if the muons which lie in the silver sample holder of the dilution refrigerator are affected by the ferromagnetism of the sample.

Temperature scans in ZF with the initial muon spin along the [001] direction on the ferromagnetic systems would provide more information about the

shape and size of internal field distribution in the ferromagnetic regime. With the initial muon polarization along the [310] direction (as all the measurements presented in this work), it would be also interesting to perform temperature scans in the  $x=1$  and  $x=0.45$  systems; both at high LF (probably 2T). These measurements would allow us to see how the fluctuations of the paramagnetic moments evolve with temperature as well as observe if the random fields have any effect in the paramagnetic behavior. Another temperature scan in the  $x=0.45$  system, but this time in an LF of 0.5T, would be very interesting to perform since it would allow us to make a clear map of the dynamics at a field where other research works have observed another transition into a ferroglass ground state [27]. It would be interesting to make a couple of runs at the same temperature and field but entering the ferroglass state through different paths on the  $H$ - $T$  phase diagram (one from the top and another from the bottom) to check if the effect of quantum annealing [27] can be observed at the microscopic level.

It would be interesting to perform TF measurements in the ferromagnetic state of the  $x=1$  system with the external field along the Ising direction. This experimental setup would probably allow us to increase the size of the parallel domains to the expense of the anti parallel ones and, in this way, study the effect of the magnetic domain structure in the  $\mu$ SR signal. In this experiment it would be expected that as the field is increased, more muons land in big parallel domains which probably would show progressively narrower internal field distributions. During these measurements it should be kept in mind that below  $\approx 0.2$ T avoided-level-crossing resonances would be crossed [16]. These resonances, which produce a decrease in the relaxation rate [41], should not be

confused with the effect of the magnetic domain structure. Also, further optical mapping of the magnetic domain structure [85] together with numerical calculations at the microscopic level could help determine if the magnetic domain formation is the source of the broad field distribution which we observed. At the same time, these calculations can estimate if the mesoscopic domain formation could affect the Ho ferromagnetism at the microscopic level.

As we mention before, we did not find any evidence for a qualitative change on the physical properties of the system with dilution once ferromagnetism is destroyed. This is, we did not find evidence for the existence of a low  $x$  “anti-glass” phase. Further more, our  $x=0.045$  sample have a  $\chi_{AC}$  behavior which is consistent with that of a glass [36], in contraposition to the “anti-glass” behavior observed by other research group [20] (Section 2.2.3). In order to rule out any sample dependence on this matter, it would be interesting to perform  $\mu$ SR measurements in a sample where “anti-glass” behavior has already been observed.

Finally, it should be interesting to perform TF measurements (with the magnetic field perpendicular to the Ising direction) in samples with very low dilution (like the one used in Reference [41]) in order to observe the magnetic moment renormalization induced by the hyperfine interaction in low transverse field [45], although spectroscopic measurements might be more suitable for this task.

## Appendix A

### Field width vs. doping

In this appendix we derive the dependence of the parameter  $a$  on the dilution level of the magnetic system. The derived expression is valid only in the high dilution limit  $x \ll 1$ , where  $x$  is the probability of a magnetic site being occupied.

The parameter  $a$  in Equation 3.13 is a measure of how broad the field distribution felt by the muon ensemble is. To estimate this range of fields felt by the muon ensemble it has to be noticed that in the high dilution limit, the biggest contribution to the broadening of the signal is the presence (or absence) of a magnetic moment nearby, and not so much the direction in which these moments can point. Muons in regions with high magnetic moment density will see, on average, high fields; while those in regions of low density will see smaller ones. Let's call  $V_\mu$  a volume of influence around the muon such that magnetic moments within this volume are those who have the biggest effect on it. If there are  $N$  possible sites for the magnetic ion to sit inside this environment, then the number of magnetic moments within this volume follow a binomial distribution with success probability equal to  $x$ . Using this, one can define the magnetic moment density at the magnetically concentrated sites as:

$$\rho_+ = \frac{Nx + \sigma}{N} \quad (6.1)$$

while that at the low concentrated sites as:

$$\rho_- = \frac{Nx - \sigma}{N} \quad (6.2)$$

where  $\sigma$  is the standard deviation of the binomial distribution and is given by:

$$\sigma = \sqrt{Nx(1-x)} \quad (6.3)$$

Now, for a given density of moments around a muon site the characteristic field strength is given by the strength of the closest magnetic ion. This ion is, in average, at a distance  $r$  from the muon, such that  $r^3 = 1/\rho$ , where  $\rho$  is the local magnetic density. Then the strength of the magnetic field at this muon site will be:

$$B \propto \frac{1}{r^3} = \rho \quad (6.4)$$

Using this equation and 6.1 and 6.2, one can define the following range of fields felt by the muon ensemble as:

$$a \propto (B_+ - B_-) \propto (\rho_+ - \rho_-) \propto \sqrt{x(1-x)} \quad (6.5)$$

Then, since  $x$  is small:

$$a \propto \sqrt{x} \quad (6.6)$$

A square root behavior can be observed at low  $x$  in numerical calculations in Reference [71]. In these calculations the second moment of the field distribution is obtained as a function of  $x$  for the case where a muon sits at the octahedral interstitial site of a diluted FCC lattice of Heisenberg spins.

## Bibliography

- [1] Encyclopædia Britannica. Electromagnetism. *Encyclopædia Britannica Online*, January 2008.
- [2] B.K. Chackrabarti, A. Dutta, and P. Sen. *Quantum Ising Phases and transitions in transverse Ising models*. Springer, 1996.
- [3] R.J. Birgeneau, W.B. Yelon, E. Cohen, and J. Makovsky. *Phys. Rev. B*, 5:2607, 1972.
- [4] J. W. Stout and R. C. Chisolm. *J. Chem. Phys.*, 36:979, 1962.
- [5] S. Blundell. *Magnetism in condensed matter*. Oxford University Press, 1996.
- [6] A. Dutta, B.K. Chackrabarti, and R.B. Stinchcombe. *J. Phys. A: Math. Gen.*, 29:5285, 1996.
- [7] J. E. Greedan. *J. Mater. Chem.*, 11:37, 2001.
- [8] J. A. Mydosh. *Spin glasses: an experimental introduction*. Taylor & Francis, 1993.
- [9] J. Magariño, J. Tuchendler, J. P. D'Haenens, and A. Linz. *Phys. Rev. B*, 13:2805, 1976.
- [10] Y. Kalisky, J. Kagan, D. Sagie, A. Brenier, C. Pedrini, and G. Boulon. *J. Appl. Phys.*, 70:4095, 1991.

- [11] G. Mennenga, L. J. de Johgh, and W. J. Huiskamp. *J. Magn. Magn. Mat.*, 44:59, 1984.
- [12] L. M. Holmes, T. Johansson, and H. J. Guggenheim. *Solid State Commun.*, 12:993, 1973.
- [13] S. M. A. Tabei, M. J. P. Gingras, Y. J. Kao, and T. Yavors'kii. *Phys. Rev. B*, 78:184408, 2008.
- [14] K. Kjaer, J Als-Nielsen, I. Laursen, and F Krebs Larsen. *J. Phys.: Condens. Matter*, 1:5743, 1989.
- [15] P. B. Chakraborty, P. Henelius, H. Kjønsgberg, A. W. Sandvik, and S. M. Girvin. *Phys. Rev. B*, 70:144411, 2004.
- [16] R. Giraud, W. Wernsdorfer, A. M. Tkachuk, D. Mailly, and B. Barbara. *Phys. Rev. Lett.*, 87:057203–1, 2001.
- [17] H. M. Rønnow, J. Jensen, R. Parthasarathy, G. Aeppli, T. F. Rosenbaum D. F. McMorrow, and C. Kraemer. *Phys. Rev. B*, 75:054426, 2007.
- [18] H. M. Rønnow, R. Parthasarathy, J. Jensen, G. Aeppli, and T. F. Rosenbaum D. F. McMorrow. *Science*, 308:389, 2005.
- [19] P. Beauvillain, J.-P. Renard, I. Laursen, and P. J. Walker. *Phys. Rev. B*, 18:3360, 1978.
- [20] D. H. Reich, B. Ellman, J. Yang, T. F. Rosenbaum, G. Aeppli, and D. P. Belanger. *Phys. Rev. B*, 42:4631, 1990.

- [21] D. S. Pytalev, S. A. Kilmin, and M. N. Popova. *Phys. Lett. A*, 372:2332, 2008.
- [22] C. Ancona-Torres, D. M. Silevitch, G. Aeppli, and T. F. Rosenbaum. *Phys. Rev. Lett.*, 101:057201, 2008.
- [23] J. Nikkel and B. Ellman. *Phys. Rev. B*, 64:214420, 2001.
- [24] D. Bitko, T. F. Rosenbaum, and G. Aeppli. *Phys. Rev. Lett.*, 77:940, 1996.
- [25] D. M. Silevitch, D. Bitko, J. Brooke, S. Ghosh, G. Aeppli, and T. F. Rosenbaum. *Nature*, 448:567, 2007.
- [26] J. Brooke, T. F. Rosenbaum, and G. Aeppli. *Nature*, 413:610, 2001.
- [27] J. Brooke, D. Bitko, T. F. Rosenbaum, and G. Aeppli. *Science*, 284:779, 1999.
- [28] Ying-Jer Kao, G. S. Grest, K. Levin, J. Brooke, T. F. Rosenbaum, and G. Aeppli. *Phys. Rev. B*, 64:060402, 2001.
- [29] Wenhao Wu, B. Ellman, T. F. Rosenbaum, G. Aeppli, and D. H. Reich. *Phys. Rev. Lett.*, 67:2076, 1991.
- [30] Wenhao Wu, D. Bitko, T. F. Rosenbaum, and G. Aeppli. *Phys. Rev. Lett.*, 71:1919, 1993.
- [31] D. Bitko, N. Menon, S. R. Nagel, T. F. Rosenbaum, and G. Aeppli. *Europhys. Lett.*, 33:489, 1996.

- [32] P. E. Jönsson, R. Mathieu, W. Wernsdorfer, A. M. Tkachuk, and B. Barbara. *Phys. Rev. Lett.*, 98:256403, 2007.
- [33] P. E. Jönsson, R. Mathieu, W. Wernsdorfer, A. M. Tkachuk, and B. Barbara. arXiv:0803.1357v3, 2008.
- [34] D. H. Reich, T. F. Rosenbaum, and G. Aeppli. *Phys. Rev. Lett.*, 17:1969, 1987.
- [35] S. Ghosh, R. Parthasarathy, T. F. Rosenbaum, and G. Aeppli. *Science*, 296:2195, 2002.
- [36] J. A. Quilliam, S. Meng, C. G. A. Mugford, and J. B. Kycia. *Phys. Rev. Lett.*, 101:187204, 2008.
- [37] J. A. Quilliam, C. G. A. Mugford, A. Gomez, S. W. Kycia, and J. B. Kycia. *Phys. Rev. Lett.*, 98:037203, 2007.
- [38] J. Snider and C. C. Yu. *Phys. Rev. B*, 72:214203, 2005.
- [39] S. Ghosh, T. F. Rosenbaum, and G. Aeppli S. N. Coppersmith. *Nature*, 425:48, 2003.
- [40] M. J. Graf, A. Lascialfari, F. Borsa, A. M. Tkachuk, and B. Barbara. *Phys. Rev. B*, 73:024403, 2006.
- [41] M. J. Graf, J. Lago, A. Lascialfari, A. Amato, C. Baines, S. R. Giblin, J. S. Lord, A. M. Tkachuk, and B. Barbara. *Phys. Rev. Lett.*, 99:267203, 2007.

- [42] R. Giraud, A. M. Tkachuk, and B. Barbara. *Phys. Rev. Lett.*, 91:257204, 2003.
- [43] B. Barbara, R. Giraud, W. Wernsdorfer, i D. Mailly, P. Lejay, A. M. Tkachuk, and H. Suzuki. *J. Magn. Magn. Matter*, 272-276:1024, 2004.
- [44] M. J. P. Gingras in a private discussion with J. Rodriguez.
- [45] M. Schechter and P. C. E. Stamp. *Phys. Rev. Lett.*, 95:267208, 2005.
- [46] M. Schechter and N. Laflorencie. *Phys. Rev. Lett.*, 97:137204, 2006.
- [47] M. Schechter and P. C. E. Stamp. *Phys. Rev. B*, 78:054438, 2008.
- [48] S. M. A. Tabei, F. Vernay, and M. J. P. Gingras. *Phys. Rev. B*, 77:014432, 2008.
- [49] A. Biltmo and P. Henelius. arXiv:0903.1603v1, 2009.
- [50] M. J. Stephen and A. Aharony. *J. Phys. C: Solid State Phys.*, 14:1665, 1981.
- [51] R. Griffiths. *Phys. Rev.*, 176:655, 1968.
- [52] A. Biltmo and P. Henelius. *Phys. Rev. B*, 76:054423, 2007.
- [53] A. Biltmo and P. Henelius. *Phys. Rev. B*, 78:054437, 2008.
- [54] S. M. A. Tabei, M. J. P. Gingras, Y. J. Kao, P. Stasiak, and J. Y. Fortin. *Phys. Rev. Lett.*, 97:237203, 2006.
- [55] M. Schechter. *Phys. Rev. B*, 77:020401, 2008.

- [56] J. Brooke. PhD thesis, University of Chicago, 2000.
- [57] T. K. Kopeć. *Phys. Rev. Lett.*, 79:4266, 1997.
- [58] M. J. Rozenberg and D. R. Grempel. *Phys. Rev. Lett.*, 81:2550, 1998.
- [59] M. J. P. Gingras in a private communication to M. Schechter.
- [60] A. P. Young and H. G. Katzgraber. *Phys. Rev. Lett.*, 93:207203, 2004.
- [61] K. M. Tam and M. J. P. Gingras. arXiv:0810.0854v2, 2009. Accepted for publication in *Phys. Rev. Lett.*
- [62] S. L. Lee, S. H. Kilcoyne, and R. Cywinski, editors.  *$\mu$ SR relaxation functions in magnetic materials*. Institute of Physics Publishing, 1999.
- [63] A. Schenck. *Muon spin rotation spectroscopy: principles and applications in solid state physics*. Bristol; Boston: A. Hilger, 1985.
- [64] P. D. deR otier and A. Yaouanc. *J. Phys.: Condens. Matter*, 9:9113, 1997.
- [65] G. H. Eaton and S. H. Kilcoyne. Muon production: past, present and future. In S. L. Lee, S. H. Kilcoyne, and R. Cywinski, editors, *Muons in Physics, Chemistry and Materials*, page 97. Institute of Physics Publishing, 1999.
- [66] S. F. J. Cox. Muonium states and dynamics. In S. L. Lee, S. H. Kilcoyne, and R. Cywinski, editors, *Muons in Physics, Chemistry and Materials*, page 97. Institute of Physics Publishing, 1999.
- [67] B. D. Patterson. *Rev. Mod. Phys.*, 60:69, 1988.

- [68] Msrfit program. <http://www.musr.org/msrfit/>, August 2008.
- [69] Minuit minimization routine. <http://wwwasdoc.web.cern.ch/wwwasdoc/minuit/minmain.html>, August 2008.
- [70] Y. J. Uemura.  $\mu$ sr relaxation functions in magnetic materials. In S. L. Lee, S. H. Kilcoyne, and R. Cywinski, editors, *Muons in Physics, Chemistry and Materials*, page 97. Institute of Physics Publishing, 1999.
- [71] D. R. Noakes. *Phys. Rev. B*, 44:5064, 1991.
- [72] W. H. Press, W. T. Vetterling, S. A. Teukolsky, and B. P. Flannery. *Numerical recipes in Fortran77*. Cambridge University Press, 1992.
- [73] Y. J. Uemura, T. Yamazaki, D. R. Harshman, M. Senba, and E. J. Ansaldo. *Phys. Rev. B*, 31:546, 1985.
- [74] R. E. Walstedt and L. R. Walker. *Phys. Rev. B*, 9:4857, 1974.
- [75] R. S. Hayano, Y. J. Uemura, N. Nishida, T. Yamazaki, and R. Kubo. *Phys. Rev. B*, 20:850, 1979.
- [76] R. Kadono, H. Okajima, A. Yamashita, K. Ishii, T. Yokoo, J. Akimitsu, N. Kobayashi, Z. Hiroi, M. Takano, and K. Nagamine. *Phys. Rev. B*, 54:r9628, 1996.
- [77] G. Solt. *Hyp. Int.*, 96:167, 1995.
- [78] J. H. Brewer, S. R. Kreitzman, D. R. Noakes, E. J. Ansaldo, D. R. Harshman, and R. Keitel. *Phys. Rev. B*, 33:7813, 1986.

- [79] D. R. Noakes, E. J. Ansaldo, S. R. Kreitzman, and G. M. Luke. *J. Phys. Chem. Solids*, 54:785, 1993.
- [80] J. H. Brewer, D. R. Harshman, R. Keitel S. R. Kreitzman, G. M. Luke D. R. Noakes, and R. E. Turner. *Hyperfine Interact.*, 32:677, 1986.
- [81] R. C. Newman, S. F. J. Cox, R. A. Catlow, E. A. Davis, A. M. Stoneham, and M. Symons. *Philos. Trans. R. Soc. London, Ser. A*, 350:171, 1995.
- [82] K. Nishiyama, S. W. Nishiyama, and W. Higemoto. *Physica B*, 326:41, 2003.
- [83] Orientexpress package. <http://www.ccp14.ac.uk/ccp/web-mirrors/lmgp-laugier-bochu/>, July 2008.
- [84] D. R. Noakes, E. J. Ansaldo, and G. M. Luke. *J. Appl. Phys.*, 73:5666, 1993.
- [85] J. E. Battison, A. Kasten, M. J. M. Leask, J. B. Lowry, and B. M. Wanklyn. *J. Phys. C: Solid State Phys.*, 8:4089, 1975.
- [86] J. A. Griffin, M. Huster, and R. J. Folweiler. *Phys. Rev. B*, 22:4370, 1980.
- [87] V. Banerjee and S. Dattagupta. *Phys. Rev. B*, 64:024427, 2001.
- [88] T. M. Riseman and J. H. Brewer. *Hyperfine Interact.*, 65:1107, 1990.
- [89] I. A. Campbell. Dynamics of spin glasses. In S. L. Lee, S. H. Kilcoyne, and R. Cywinski, editors, *Muons in Physics, Chemistry and Materials*, page 137. Institute of Physics Publishing, 1999.

- [90] Lapack numerical library. <http://www.netlib.org/lapack>, November 2008.
- [91] E. Garcia and R. R. Ryan. *Acta Crystallogr., Sect. C: Cryst. Struct. Commun.*, 49:2053, 1993.
- [92] R. Feyerherm, A. Amato, F. N. Gygax, A. Schenck, and U. Zimmermann. *Hyperfine Interact.*, 85:329, 1994.
- [93] R. Feyerherm, A. Amato, A. Grayevsky, F. N. Gygax, N. Kaplan, and A. Schenck. *J. Alloy Compd.*, 231:164, 1995.
- [94] R. Feyerherm, A. Amato, A. Grayevsky, F. N. Gygax, N. Kaplan, and A. Schenck. *Z. Phys. B - Cond. Mat.*, 99:3, 1995.
- [95] T. Tashma, A. Amato, A. Grayevsky, F. N. Gygax, M. Pinkpank, A. Schenck, and N. Kaplan. *Phys. Rev. B*, 56:9397, 1997.
- [96] A. Schenck, N. K. Sato, G. Solt, D. Andreica, F. N. Gygax, M. Pinkpank, and A. Amato. *Eur. Phys. J. B*, 13:245, 2000.
- [97] F. N. Gygax, A. Schenck, G. Solt, and P. C. Canfield. *Physica B*, 326:359, 2003.
- [98] I. A. Campbell. *J. Phys. Lett. - Paris*, 45:L-27, 1984.
- [99] J. Rodriguez, S. R. Dunsiger, J. B. Kycia, G. J. MacDougall, J. A. Quilliam, P. R. Russo, A. T. Savici, Y. J. Uemura, C. R. Wiebe, and G. M. Luke. *Physica B*, 374-375:13, 2006.

- [100] J. S. Gardner, S. R. Dunsiger, B. D. Gaulin, M. J. P. Gingras, J. E. Greedan, R. F. Kiefl, M. D. Lumsden, W. A. MacFarlane, N. P. Raju, J. E. Sonier, I. Swainson, and Z. Tun. *Phys. Rev. Lett.*, 82:1012, 1999.
- [101] S. R. Dunsiger, R. F. Kiefl, J. A. Chakhalian, K. H. Chow, S. Gardner, J. E. Greedan, W. A. MacFarlane, R. I. Miller, G. D. Morris, A. N. Price, N. P. Raju, and J. E. Sonier. *Physica B*, 326:475, 2003.
- [102] B.D. Gaulin, J.N. Reimers, T.E. Mason, J.E. Greedan, and Z. Tun. *Phys. Rev. Lett.*, 69:3244, 1992.
- [103] S.R. Dunsiger and R.F. Kiefl, K.H. Chow, B.D. Gaulin, M.J.P. Gingras, J.E. Greedan, A. Keren, K. Kojima, G.M. Luke, W.A. MacFarlane, N.P. Raju, J.E. Sonier, Y.J. Uemura, and W.D. Wu. *Phys. Rev. B*, 54:9019, 1996.
- [104] M. J. P. Gingras, C. V. Stager, N. P. Raju, B. D. Gaulin, and J. E. Greedan. *Phys. Rev. Lett.*, 78:947, 1997.
- [105] Y. J. Uemura, A. Keren, K. Kojima, L. P. Le, G. M. Luke, W. D. Wu, Y. Ajiro, T. Asano, Y. Kuriyama, M. Mekata, H. Kikuchi, and K. Kakurai. *Phys. Rev. Lett.*, 73:3306, 1994.
- [106] D. Bono, P. Mendels, G. Collin, N. Blanchard, F. Bert, A. Amato, C. Baines, and A. D. Hillier. *Physica B*, 374-375:138, 2006.
- [107] A. Keren, Y. J. Uemura, G. M. Luke, P. Mendels, M. Mekata, and T. Asano and. *Phys. Rev. Lett.*, 84:3450, 2000.